UNIVERSIDADE FEDERAL DE SÃO CARLOS
CENTRO DE CIÊNCIAS EXATAS E DE TECNOLOGIA
PROGRAMA DE PÓS-GRADUAÇÃO EM CIÊNCIA E ENGENHARIA DE MATERIAIS

VITROCERÂMICAS CONDUTORAS DE ÍON LÍTIO COM ESTRUTURA DO TIPO NASICON BASEADAS NO SISTEMA $Li_{1+X}Cr_X(Ge_YTi_{1-Y})_{2-X}(PO_4)_3$

Rafael Bianchini Nuernberg

São Carlos-SP
2018

FEDERAL UNIVERSITY OF SÃO CARLOS
CENTER OF SCIENCE AND TECHNOLOGY
GRADUATE PROGRAM IN MATERIALS SCIENCE AND ENGINEERING
AND
UNIVERSITY OF MONTPELLIER
INSTITUTE CHARLES GERHARDT OF MONTPELLIER
DOCTORAL SCHOOL OF CHEMICAL SCIENCES BALARD

LITHIUM ION CONDUCTING GLASS-CERAMICS WITH NASICON-TYPE STRUCTURE BASED ON THE $Li_{1+X}Cr_X(Ge_YTi_{1-Y})_{2-X}(PO_4)_3$ SYSTEM

Rafael Bianchini Nuernberg

Thesis presented for the Graduate Program in Materials Science and Engineering of the Federal University of São Carlos in joint supervision with the Doctoral School of Chemical Sciences of the University of Montpellier in partial fulfillment of the requirements for the degree of Doctor of Philosophy in Materials Science and Engineering and Chemistry and Physical Chemistry of Materials.

Adivisor (UFSCar): Dr. Ana Candida Martins Rodrigues
Adivisor (UM): Dr. Annie Pradel
Funding: CNPq-GD (140456/2014-7)
CAPES-PDSE (88881.132930/2016-01)

São Carlos-SP
2018

DEDICATION

This thesis is dedicated to my beloved family.

VITAE

Master of Science degree in Materials Science and Engineering - Universidade Federal de São Carlos (2014), Bachelor’s degree Materials Engineering - Universidade do Extremo Sul Catarinense (2011).

UNIVERSIDADE FEDERAL DE SÃO CARLOS

Centro de Ciências Exatas e de Tecnologia
Programa de Pós-Graduação em Ciência e Engenharia de Materiais

Folha de Aprovação

Assinaturas dos membros da comissão examinadora que avaliou e aprovou a Defesa de Tese de Doutorado do candidato Rafael Bianchini Nuernberg, realizada em 22/03/2018:

Profa. Dra. Ana Candida Martins Rodrigues
UFSCar

Prof. Dr. Marcello Rubens Barsi Andreeta
UFSCar

Prof. Dr. Eduardo Bellini Ferreira
USP

Prof. Dr. Jean Claude MPeko
USP

Profa. Dra. Annie Pradel
UM

Prof. Dr. Michel Ribes
UM

Prof. Dr. Jean-Louis Souquet
Grenoble INP

Certifico que a defesa realizou-se com a participação à distância do(s) membro(s) Michel Ribes e, depois das arguições e deliberações realizadas, o(s) participante(s) à distância está(ao) de acordo com o conteúdo do parecer da banca examinadora redigido neste relatório de defesa.

Profa. Dra. Ana Candida Martins Rodrigues

ACKNOWLEDGMENTS

First, I would like to thank the graduate program of the Department of Materials Science and Engineering, at the Federal University of São Carlos (UFSCar) in Brazil, and the Ballard doctorate school of Science and Chemistry from the Institute Charles Gerhardt, at the University of Montpellier (UM) in France, for all administrative, teaching and research assistance. In particular, I would like to acknowledge all members of the Laboratory of Vitreous Materials (LaMaV) of UFSCar and Chalcogenide Glasses (ChV) of UM for providing the experimental support of this work. I am very grateful for my advisors Ana Candida Martins Rodrigues (UFSCar) and Annie Pradel (UM) for all encouragements, understanding, advises and above all, obligingness with my work during the whole path. I also wish to recognize the contribution of the members of my committee. Dr. Jean-Louis Souquet and Dr. Michel Ribes for their valuable guidance in solid state electrochemistry and Dr. Edgar Zanotto for providing the glass science background necessary to execute this work. I cannot fail to thank all professors that have participated somehow in my academic formation. Additionally, I acknowledge the financial funding of two brazilian institutions that made this research possible, namely CNPq (Brazil's National Council for Scientific and Technological Development) and CAPES (Coordination for the Improvement of Higher Education Personnel) for the doctoral scholarships in Brazil and France granted under Projects no. 140456/2014-7 and 88881.132930/2016-01, respectively. I am also very grateful to FAPESP (São Paulo Research Foundation) for its financial incentive in this work, under CEPID Process no. 2013/07793-6. Finally, I would like to acknowledge my parents and relatives for the motivational backing I have received in every family gathering, my friends, Jhonatan, Mathieu, and Jésus Thiago for the encouragement, and my girlfriend Norma Maria for the unconditional support during this journey.

ABSTRACT

The primary goal of this work is to develop a new NASICON-structured glass-ceramic with high Li-ion conductivity. Therefore, this work introduces a new series of NASICON-type compositions based on the $Li_{1+x}Cr_x(Ge_yTi_{1-y})_{2-x}(PO_4)_3$ system. At first, a specific glass-ceramic composition of this system was synthesized by the melt-quenching method, followed by crystallization. The crystallization behavior of the precursor glass was examined by differential scanning calorimetry and infrared spectroscopy. The results indicate that the precursor glass presents homogeneous nucleation, has considerable glass stability and crystallizes a NASICON-like phase, which allows solid electrolytes to be obtained by the glass-ceramic route. As a second step, we examine the effect of substituting Ti by Cr and Ge on the glass stability of the precursor glasses, on the structural parameters of NASICON-like phase and on the electrical properties of the glass-ceramics. Hence, a set of sixteen compositions of this system was synthesized. The results indicate that the glass stability increases when Ti is replaced by Ge and Cr. After crystallization, all the glass-ceramics present NASICON-like phase, and their lattice parameters decrease with Ge and increase with Cr content, making it possible to adjust the unit cell volume of the structure. Furthermore, the ionic conductivity and activation energy for lithium conduction in the glass-ceramics are notably dependent on the unit cell volume of the NASICON-type structure, achieving total ionic conductivities of up to $3x10^{-4}$ $\Omega^{-1}cm^{-1}$. Finally, the electrochemical stability window of the NASICON-structured glass-ceramics of highest ionic conductivity is investigated. Cyclic voltammetry measurements were followed by *in situ* electrochemical impedance spectroscopy, enabling the effect of oxidation and reduction reactions on the electrical properties of the investigated glass-ceramics to be determined. X-ray photoelectron spectroscopy, in turn, was applied to determine which chemical species undergo reduction/oxidation. Our findings reveal that the electrochemical stability of this material is limited by the reduction of Ti^{+4} cations at low potentials and by the oxidation of O^{-2} anions at high potentials. A similar behavior at high potentials was also encountered for other well-known Li-ion conducting NASICON-like phosphate suggesting that the electrochemical behavior in oxidative potentials could be generalized for NASICON-structured phosphates.

Keywords: Li ion-conducting glass-ceramics; Glass stability; NASICON-type structure; Ionic conductivity; Electrochemical stability;

RESUMO

O principal objetivo do presente trabalho é desenvolver uma nova vitrocerâmica de alta condutividade de íons lítio com fase cristalina NASICON. Portanto, este trabalho introduz uma série de composições do tipo NASICON baseadas no sistema $Li_{1+x}Cr_x(Ge_yTi_{1-y})_{2-x}(PO_4)_3$. Primeiramente, uma composição específica desse sistema foi sintetizada pela rota tradicional de fusão de vidros seguida de cristalização. O comportamento de cristalização do vidro precursor é examinado por técnicas de calorimetria diferencial exploratória e espectroscopia de infravermelho. Os principais resultados obtidos nesta etapa indicaram que o vidro precursor apresenta nucleação homogênea, possui estabilidade vítrea apreciável e precipita a fase cristalina NASICON quando submetido a tratamento de cristalização. Estes resultados qualificam a rota vitrocerâmica como uma via de obtenção de eletrólitos sólidos a partir deste sistema composicional. Em uma segunda etapa é examinado o efeito da substituição de Ti por Cr e Ge na estabilidade frente à cristalização do vidro precursor, nos parâmetros estruturais da fase tipo NASICON e nas propriedades elétricas das vitrocerâmicas obtidas. Assim, um conjunto de dezesseis composições foi sintetizado a partir do sistema composicional proposto. Os resultados dessa etapa apontam que a estabilidade do vidro contra à cristalização aumenta com a substituição de Ti por Ge e Cr. Após o tratamento de cristalização todas as vitrocerâmicas apresentaram fase cristalina com estrutura do tipo NASICON e o volume da célula unitária diminui com a concentração de Ge e aumenta com a concentração de Cr, evidenciando a possibilidade de ajuste dos parâmetros estruturais da fase cristalina tipo NASICON. Além disso, a condutividade iônica e a energia de ativação para condução de lítio das vitrocerâmicas são notavelmente dependentes do volume da célula unitária, atingindo condutividades iônicas totais de até $3x10^{-4}$ $\Omega^{-1}cm^{-1}$. Finalmente, a janela de estabilidade eletroquímica das vitrocerâmicas de maior condutividade iônica é investigada. Uma abordagem inovadora utilizando voltametria cíclica acompanhada in situ por espectroscopia de impedância, permitiu o estudo do efeito das reações de oxidação e redução nas propriedades elétricas das vitrocerâmicas em questão. Por sua vez, espectroscopia foto eletrônica de raios-X é aplicada para determinar quais espécies químicas sofreram redução e/ou oxidação após a aplicação de um potencial elétrico. Os resultados revelam que a janela de estabilidade eletroquímica desses eletrólitos é limitada pela redução de cátions Ti^{+4} em baixos potenciais e pela oxidação de aníons O^{-2} em altos potenciais. Um comportamento similar em altos potenciais foi encontrado para outro conhecido fosfato condutor de lítio do tipo NASICON, sugerindo que o comportamento em potenciais oxidantes pode ser generalizado para fosfatos com estrutura NASICON.

Palavras-chaves: Vitrocerâmicas condutoras por lítio; Estabilidade contra à cristalização; Estrutura NASICON; Condutividade iônica; Estabilidade eletroquímica;

RÉSUME

L'objectif principal de ce travail est de développer une nouvelle vitrocéramique contenant une phase cristalline de type NASICON ayant une conductivité Li-ion élevée. Par conséquent, ce travail présente une nouvelle série de compositions de type NASICON sur la base du système Li1+xCrx(GeyTi1-y)2-x(PO4)3. Dans un premier temps, une composition spécifique de ce système a été synthétisée par la méthode de fusion et refroidissement rapide, suivie d'une cristallisation. La cristallisation du verre précurseur a été examinée par calorimétrie différentielle à balayage et spectroscopie infrarouge. Les principaux résultats indiquent que le verre précurseur présente une nucléation homogène et une stabilité vitreuse considérable. Il cristallise avec précipitation d'une phase de type NASICON, ce qui permet d'obtenir des électrolytes solides par voie vitrocéramique. Dans une deuxième étape, on examine l'effet de la substitution de Ti par Cr et Ge sur la stabilité vitreuse du verre précurseur, sur les paramètres structuraux de la phase cristalline NASICON et sur les propriétés électriques des vitrocéramiques. Par conséquent, un ensemble de seize compositions de ce système est synthétisé. Les principaux résultats indiquent que la stabilité vitreuse augmente lorsque Ti est remplacé par Ge et Cr. Après cristallisation, toutes les vitrocéramiques présentent une phase de type NASICON, et leurs paramètres de maille décroissent avec Ge et augmentent avec la teneur en Cr, ce qui permet d'ajuster le volume de la cellule élémentaire de la structure de type NASICON. De plus, la conductivité ionique et l'énergie d'activation de conduction du lithium dans les vitrocéramiques dépendent notamment du volume de la cellule élémentaire de la structure de type NASICON, atteignant des conductivités ioniques totales allant jusqu'à $3x10^{-4}$ $\Omega^{-1}cm^{-1}$. Enfin, la fenêtre de stabilité électrochimique de la vitrocéramique à structure NASICON de conductivité ionique la plus élevée est étudiée. Les mesures de voltampérométrie cyclique sont suivies par spectroscopie d'impédance électrochimique in situ, ce qui permet de déterminer l'effet des réactions d'oxydation et de réduction sur les propriétés électriques des vitrocéramiques en question. La spectroscopie photoélectronique par rayons X, à son tour, est appliquée pour déterminer les espèces chimiques qui subissent une réduction/oxydation. Nos résultats révèlent que la stabilité électrochimique de ce matériau est limitée par la réduction des cations Ti+4 dans les faibles potentiels et par l'oxydation des anions O-2 dans les hauts potentiels. Aux hauts potentiels, un comportement similaire a également été rencontré pour d'autres compositions conductrices par Li-ion de type NASICON bien connues, suggérant que le comportement électrochimique dans les potentiels oxydatifs pourrait être généralisé pour les phosphates à structure NASICON.

Mots-clés: Vitrocéramiques conductrices par lithium; Stabilité vitreuse; Structure NASICON; Conductivité ionique; Stabilité électrochimique.

PUBLICATIONS

- R.B. Nuernberg, A.C.M. Rodrigues, M. Ribes, A. Pradel, Electrochemical properties of NASICON-structured glass-ceramics of the $Li_{1+x}Cr_x(Ge_yTi_{1-y})_{2-x}(PO_4)_3$ system, Electrochimica Acta. (Accepted)
- R.B. Nuernberg, A.C.M. Rodrigues, M. Ribes, A. Pradel, Electrochemical properties of NASICON structured glass-ceramics, Journée Scientifique de l'ICGM, September 2017, Lattes, França. (Oral Presentation)
- A. Pradel, R. Nuernberg, A. C. M. Rodrigues, M. Ribes, Electrical and electrochemical properties of lithium ion-conducting glass-ceramics from the $Li_{1+x}Cr_x(Ge_yTi_{1-y})_{2-x}(PO_4)_3$ system. XI Brazilian symposium on glass and related materials, July 2017, Curitiba-PR, Brasil. (Oral Presentation)
- A. Pradel, R. Nuernberg, A. C. M. Rodrigues, M. Ribes, Lithium ion-conducting glass-ceramic on the $Li_{1+x}Cr_x(Ge_yTi_{1-y})_{2-x}(PO_4)_3$ system, L'école thématique du GDR-Verres: Structural role of elements in glasses, from classical concepts to a reflexion over broad composition range, Mars 2017, Cargèse, France. (Poster Presentation)
- R.B. Nuernberg, A. Pradel, A.C.M. Rodrigues, A systematic study of glass stability, crystal structure and electrical properties of lithium ion-conducting glass-ceramics of the $Li_{1+x}Cr_x(Ge_yTi_{1-y})_{2-x}(PO_4)_3$ system, J. Power Sources. 371 (2017) 167–177. doi:10.1016/j.jpowsour.2017.10.020.
- R.B. Nuernberg, A.C.M. Rodrigues, A new NASICON lithium ion-conducting glass-ceramic of the $Li_{1+x}Cr_x(Ge_yTi_{1-y})_{2-x}(PO_4)_3$ system, Solid State Ionics. 301 (2017) 1–9. doi:10.1016/j.ssi.2017.01.004.
- R. Nuernberg, A. C. M. Rodrigues, A new lithium ion-conducting glass-ceramic with NASICON structure. 60° Congresso Brasileiro de Cerâmica, may of 2016, Águas de Lindóia-SP, Brasil. (Oral Presentation)
- L. E. T. Mathias, R. Nuernberg, A. C. M. Rodrigues, Preparação e caracterização de vitrocerâmicas condutoras por lítio baseadas no sistema $Li_2O.Cr_2O_3.GeO_2.TiO_2.P_2O_5$, new lithium ion-conducting glass-ceramic with nasicon structure. XVII Congresso dos Estudantes de Ciência e Engenharia de Materiais do MERCOSUL, July of 2015, São Carlos-SP, Brasil. (Poster Presentation, Award of Best Poster)

LIST OF CONTENTS

LIST OF TABLES

LIST OF FIGURES

ABBREVIATIONS AND SYMBOLS

AC	alternating current
BE	binding energy
CV	cyclic voltammetry
DC	direct current
DSC	differential scanning calorimetry
EC	equivalent circuits
EDX	energy dispersive X-ray spectroscopy
EIS	electrochemical impedance spectroscopy
emf	electromotive force
FT-IR	Fourier transform infrared spectroscopy
ICP-MS	inductively coupled plasma mass spectrometry
LAGP	$Li_{1+x}Al_xGe_{2-x}(PO_4)_3$ (0<x<1)
LAGTP	$LiGe_2(PO_4)_3$
LATP	$Li_{1+x}Al_xTi_{2-x}(PO_4)_3$ (0<x<1)
LCGTP	$Li_{1+x}Cr_x(Ge_yTi_{1-y})_{2-x}(PO_4)_3$ (0<x<1, 0<y<1)
LGP	$LiGe_2(PO_4)_3$
LiPON	$Li_xPO_yN_z$
LISICON	Li super ionic conductor
LLT	$Li_{3x}La_{(2/3)-x}\square_{(1/3)-2x}TiO_3$ (0<x<1/6)
LLZ	$Li_7La_3Zr_2O_{12}$
LSV	linear sweep voltammetry
LTP	$LiTi_2(PO_4)_3$
MYEGA	Mauro–Yue–Ellison–Gupta–Allan
NASICON	Na super ionic conductor
ocv	open circuit voltage
OD	optical dilatometry
PTFE	polytetrafluoroethylene
RC	parallel combination of an ideal resistor and capacitor
RMS	root mean square
RT	room temperature
SEM	scanning electron microscopy
SHE	standard hydrogen electrode
VTF	Vogel−Tammann−Fulcher
XPS	*X-ray photoelectron spectroscopy*
XRD	X-rays diffraction

a_O	activity of O species	
A_{ox}	pre-exponential term for oxidation rate	$mol.s^{-1}$
a_R	activity of R species	
A_{red}	pre-exponential term for reduction rate	$mol.s^{-1}$
C	capacitance	F
C_g	grains capacitance	F
CPE	constant phase element	F
CPE_a	glass constant phase element	F
CPE_e	electrode constant phase element	F
CPE_{gb}	constant phase element related to grain boundary	F
D	diffusion coefficient	$m^2.s^{-1}$
E	electrode potential	V
$\vec{E}$	electric field	$V.m^{-1}$
E_0	standard electrode potential	V
E_a	activation energy for ionic diffusion	eV
E_a'	activation energy for ionic conductivity Eq. 2.5	eV
E_a''	activation energy for ionic conductivity Eq. 2.6	eV
$E_a'_g$	activation energy related to grain ionic conductivity	eV
$E_a'_{gb}$	activation energy related to grain boundary ionic conductivity	eV
$E_a'_t$	activation energy related to total ionic conductivity	eV
E_{eff}	effective operating potential	V
E_{eq}	equilibrium potential	V
E_{ocv}	open circuit potential	V
E_{th}	standard theoretical potential	V
F	Faraday's constant	F
$\vec{F}$	force	N
f	frequency	Hz
I	current	A
I_a	anodic current	A
I_c	cathodic current	A
I_e	partial electronic current carried by electrons	A
I_{el}	total electronic current	A
I_h	partial electronic current carried by holes	A
j	density current	$A.m^{-2}$
k_0	standard rate constant	$mol.s^{-1}$
k_B	Boltzmann's constant	$J.K^{-1}$
K_H	Hruby parameter	
k_{ox}	reduction rate constant	$mol.s^{-1}$
k_{red}	oxidation rate constant	$mol.s^{-1}$

M'	interstitial site 1 of NASICON-type structure	
M"	interstitial site 2 of NASICON-type structure	
m_a	measured mass	g
m_{th}	theoretical mass	g
n	number of electrons transferred	
n*	charged carrier concentration	m^{-3}
n_0	mobile species concentration	m^{-3}
n_{CPE}	constant phase element exponent	
n_{gb}	constant phase element exponent related to grain boundary	
ocv	open circuit potential	
P	electric power	W
Q	electrical capacity	A.s
Q_{CPE}	constant phase element capacitance	F
Q_{gb}	constant phase element capacitance related to grain boundary	F
r	Pearson's correlation coefficient	
$\bar{R}$	ideal gas constant	$J.mol^{-1}.K^{-1}$
R	apparent resistance	Ω
R_0	cell measurement resistance	Ω
R_a	glass resistance	Ω
R_g	grain resistance	Ω
R_{gb}	grain boundary resistance	Ω
R_i	internal resistance	Ω
T	temperature	K
t_e	transference number of electrons	
T_g	glass transition temperature	K
T_{gr}	reduced glass transition temperature	
t_i	transference number of ions	
T_l	liquidus temperature	K
T_m	melting temperature	K
T_p	crystallization peak temperature	K
T_x	onset crystallization temperature	K
Z'	real part of impedance	Ω
Z"	imaginary part of impedance	Ω
Z*	complex impedance	Ω
Ze	associated charge of the charged carriers	C
Z_s'	real part of specific impedance	Ω.cm
Z_s"	imaginary part of specific impedance	Ω.cm
Z_s*	specific complex impedance	Ω.cm
|Z|	impedance modulus	Ω

α	transfer coefficient	
$\Delta G°$	Gibb's free energy	J
ΔG_m	Gibb's free energy of ion migration	J
ΔG_f	Gibb's free energy of defect formation	J
ΔG_{ox}	Gibb's free energy of activation for oxidation	J
ΔG_{red}	Gibb's free energy of activation for reduction	J
Δt	time interval	s
ΔH_f	enthalpy of defect formation	J
ΔH_m	enthalpy of charge carrier migration	J
ΔS_f	entropy of defect formation	J
ΔS_m	entropy of charge carrier migration	$J.K^{-1}$
ε_r	relative permittivity	
η	polarization potential	V
η_c	concentration polarization	V
η_{ct}	charge-transfer polarization	V
θ	diffraction angle	º
λ	jump distance	m
μ	ion mobility	$cm^2.V^{-1}.s^{-1}$
ν	attempt frequency	Hz
ρ	resistivity	$\Omega.cm$
σ	conductivity	$\Omega^{-1}.cm^{-1}$
σ_0'	pre-exponential term of eq. 2.5	$\Omega^{-1}.cm^{-1}$
$\sigma_0'_g$	pre-exponential related to grain contribution	$\Omega^{-1}.cm^{-1}$
$\sigma_0'_{gb}$	pre-exponential related to grain boundary contribution	$\Omega^{-1}.cm^{-1}$
$\sigma_0'_t$	pre-exponential related to total contribution	$\Omega^{-1}.cm^{-1}$
σ_0''	pre-exponential term of eq. 2.6	$K.\Omega^{-1}.cm^{-1}$
σ_e	electronic conductivity	$\Omega^{-1}.cm^{-1}$
σ_g	grain conductivity	$\Omega^{-1}.cm^{-1}$
σ_{gb}	grain boundary conductivity	$\Omega^{-1}.cm^{-1}$
σ_i	ionic conductivity	$\Omega^{-1}.cm^{-1}$
σ_t	total ionic conductivity	$\Omega^{-1}.cm^{-1}$
ϕ	phase shift angle	º
χ^2	goodness of fit	
ω	angular frequency	rad

1 INTRODUCTION

Electrochemical energy storage systems represent today a feasible alternative for the widely-criticized global fossil fuel-based economy. As one of the most widely employed electrochemical energy storage technologies, Li-ion batteries are the primary choice for applications in portable electronics and power tools due to their unique combination of high energy and power density. Moreover, they currently represent the most promising electrochemical storage system to lead the transition towards renewable energy sources and the replacement of gas-powered vehicles by electric vehicles. However, the exponential growth expected for this technology still faces some challenges, such as the development of electrode materials with higher energy density, faster discharge kinetics, and greater stability; and the development of safer and more reliable electrolytes to replace the liquid solutions of salts and organic solvents currently in use.

Regarding electrolytes, a critical issue is the flammability of organic liquid electrolytes, which cause severe safety problems for Li-ion batteries. Moreover, the limited electrochemical window of these electrolytes restricts the choice of high voltage electrode materials, precluding Li-ion batteries with higher energy density. All-solid-state batteries enabled by solid electrolyte based on Li-ion conducting ceramics are promising alternatives to ensure the intrinsic safety required by the new generation of Li-ion batteries, since they are not flammable. The claimed outstanding stability of ceramic solid electrolyte materials may also allow the production of Li metal anodes and high-voltage cathodes, which may significantly increase the energy density of Li-ion batteries. The most widely studied inorganic lithium ion conductors include sulfide glasses and crystals, oxides with perovskite-type and garnet-type structures, and phosphates with NASICON-type structures.

The main advantage of NASICON-like lithium ion conductors is their structural versatility within a wide range of compositions. The base chemical formula of these compounds can be written as $LiB_2(PO_4)_3$, where B is a tetravalent cation (Ge, Ti, Zr, Sn or Hf). The NASICON-type structure consists of a covalent skeleton containing BO_6 octahedra linked by corners to PO_4

tetrahedra, which form 3D interconnected channels and two types of interstitial positions in which the mobile cations are distributed. Mobile cations move from one site to another through bottlenecks whose size depends on the skeleton framework, which in turn depends on the size of the B atoms in the BO_6 octahedra. Hence, the structural and electrical properties of NASICON-type compounds vary widely according to the composition of the framework. Among the aforementioned tetravalent cations, Ti in the $LiTi_2(PO_4)_3$ (LTP) system leads to the simple NASICON-type compound with the highest lithium conductivity and lowest activation energy. Additionally, the partial substitution of the B^{+4} cation by a trivalent cation, B^{+3} (Al, Ga, In, Sc, Y, La, Cr or Fe), generates a deficiency in positive charge, which is compensated by the addition of Li^+ ions, leading to the $Li_{1+x}B''_xB'_{2-x}(PO_4)_3$ system.

Due to its particular characteristics and ability to form solid solution, NASICON-type compounds have been synthesized with several chemical compositions using different synthesis routes, such as the sol-gel, solid-state reaction and glass-ceramic routes. In this respect, the glass-ceramic route offers clear advantages over any route that requires a further sintering stage to consolidate the electrolyte, since it allows low porosity electrolytes to be synthesized and the microstructure to be appropriately designed through controlled glass crystallization. However, the main drawback of the glass-ceramic route is that it requires the glassy state to be reached first, with crystallization occurring only in a subsequent step. Unfortunately, not all NASICON-like compositions can form a glass at the typical cooling rates used in the laboratory or industrial settings. Moreover, well-controlled glass crystallization requires homogenous nucleation of the glass system.

Based on these concepts, this work introduces a new series of NASICON compositions based on the $Li_{1+x}Cr_x(Ge_yTi_{1-y})_{2-x}(PO_4)_3$ system. The idea behind the proposal of the LCGTP system is based on the rationale that the introduction of germanium oxide (GeO_2) increases the glass forming ability of the precursor glass. On the other hand, since Ge^{+4} (0.0670 nm) has smaller crystal radius than Ti^{+4} (0.0745 nm) in octahedral coordination, the presence of titanium oxide (TiO_2) helps to keep the cell parameters of NASICON-type structure close to those of

LTP system. Chromium oxide (Cr_2O_3) is chosen as the trivalent doping to increase lithium concentration in the NASICON-like phase because the crystal radius of Cr^{+3} in octahedral coordination (0.0755 nm) is very close to the crystal radius of Ti^{+4} (0.0745 nm).

The primary goal of this work is to develop a new NASICON-structured glass-ceramic with high Li-ion conductivity. The specific goals are the investigation of the crystallization behavior, and the glass stability of the precursor glasses, the influence of Ti substitution by Cr and Ge on the electrical properties of the NASICON-structured glass-ceramics and the electrochemical stability window of the synthesized electrolytes. Hence, at first, a particular composition ($Li_{1.4}Cr_{0.4}(Ge_{0.4}Ti_{0.6})_{1.6}(PO_4)_3$) of the proposed LCGTP system is synthesized through the glass-ceramic route and its glass forming ability and crystallization behavior (homogenous or heterogeneous) is investigated. The formation of the NASICON-like phase as well as its electrical properties is also studied. Secondly, the double substitution of Ti by Cr and Ge in the $Li_{1+x}Cr_x(Ge_yTi_{1-y})_{2-x}(PO_4)_3$ (LCGTP) system is systematically investigated. In total, sixteen compositions are tailored by means of a simple combination of x and y varying as 0.2, 0.4, 0.6 and 0.8. Then, the influence of both Cr and Ge content on the glass stability, lattice parameters of the NASICON structure and the influence on ionic conductivity and its activation energy is presented and discussed. Finally, the electrochemical properties of the Li-ion conducting glass-ceramics of highest ionic conductivity is evaluated. The electrochemical stability window of these electrolytes is determined, and the redox reaction and the species that undergoes reduction and/or oxidation are identified.

2 THEORY

In this chapter, the fundamental concepts for the understanding of the core issues of this thesis are presented and the most important electroanalytical techniques to characterize solid electrolytes are introduced.

2.1 Electrochemical Cells

Electrochemical cells are devices that convert chemical into electric energy and/or store electric as chemical energy. Consequently, electrochemical cells are the most fundamental part of piles and rechargeable batteries. A typical electrochemical cell is constituted of two half-cells, each containing an electrode in contact with an electrolyte. The two electrodes are externally connected by an electronic conductor such as a metal wire, to allow electrical current to flow from one half-cell to the other. The definition mentioned above, based on chemical conversion and electric storage, is used to classify electrochemical cells into two types, namely, galvanic and electrolytic. In galvanic cells, chemical reactions occur spontaneously at the electrode-electrolyte interfaces and electrons are transferred from one electrode to another, converting chemical energy into electric current. In electrolytic cells, reactions are forced to occur in opposition to their favorable thermodynamic direction using an external source of power connected to both electrodes [1–4]. Figure 2.1 shows schematic representations of galvanic and electrolytic cells using Copper (Cu) and Zinc (Zn) as electrodes and an aqueous solution of zinc and copper sulfate as the electrolyte. Here, a salt bridge is employed to provide ionic contact between two half-cells with different electrolytes yet preventing the solutions from mixing and causing unwanted side reactions. Note that, the electrode polarization and the directions of charged and chemical species as well as the chemical reactions are inverted when comparing galvanic (Figure 2.1a) with electrolytic (Figure 2.1b) cells.

The electromotive force (emf) for the spontaneous process of chemical conversion is provided by a difference of chemical potential between electroactive species of the two different electrodes in contact with the electrolyte. The *efm* of an electrochemical cell can be experimentally determined by connecting a high impedance voltmeter to the cell and measuring the so-called

open circuit voltage (ocv). In summary, the *efm* is a theoretical parameter while the *ocv* is a experimental parameter. In the example of Figure 2.1, metallic Zn has a higher tendency toward oxidation than Cu providing the difference of chemical potential. Therefore, chemical reactions (redox couple) in which species are oxidized at the anode (Zn) and others are reduced at the cathode (Cu) take place to minimize the free energy of the system (Figure 2.1a). The products of this reactions have an electronic and an ionic component which must be divided into two distinct pathways if it is desired to drain the converted energy. The electrolyte should conduct through the cell the ionic chemical species involved in this redox couple and forces the electronic component to traverse a circuit outside the cell to deliver the converted electrical energy. In contrast, to store electrical as chemical energy, an external opposite power must be applied to overcome the former *emf* of the cell and reverse the direction of those chemical reactions. Thus, electrical energy from the external source is stored as chemical energy in the form of the products of the electrode reactions (Figure 2.1b). Therefore, a rechargeable battery is based on these two types of electrochemical cells, where the discharge process is essentially a galvanic cell, and the charging process is an electrolytic cell [1–3,5,6].

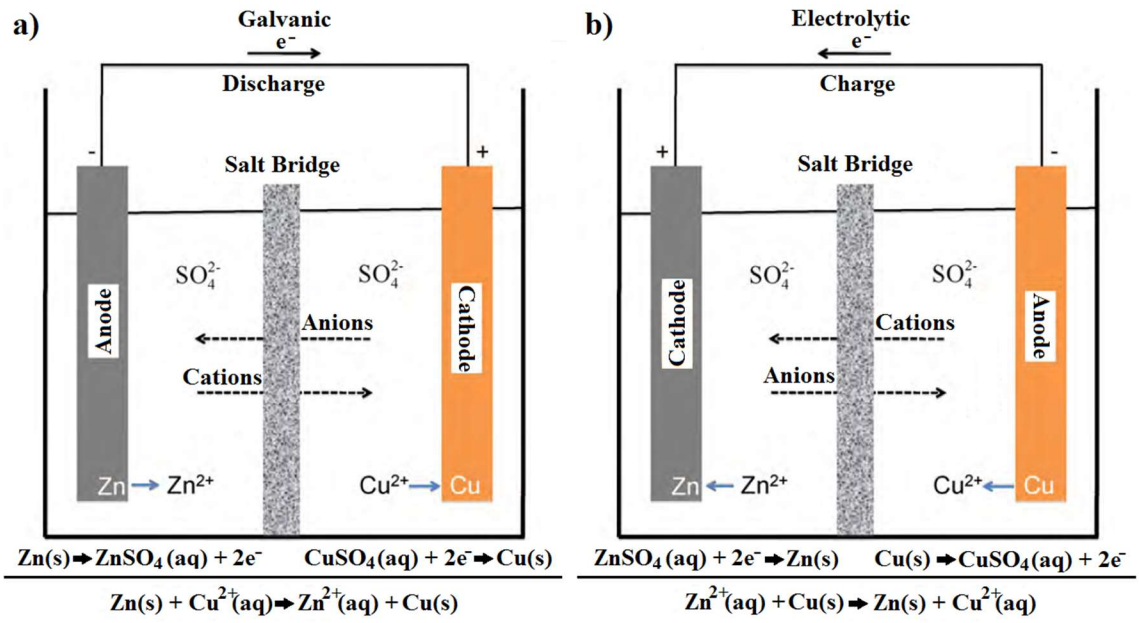

Figure 2.1 – Schematic representation of the two types of electrochemical cells: (a) galvanic cell; (b) electrolytic cell (adapted from [1]).

In order to assure that the chemical and electric processes will follow the conditions listed above, the electrodes must be an electronic conductor (metal) or a mixed ionic-electronic conductor (carbon and intercalation compounds). The electronic conductivity is a crucial property because the electrons released by the redox reaction must flow through the electrodes to reach the external electrical circuit. Still, the electrodes must also deliver and/or incorporate ions coming through the electrolyte from the opposite half-cell. In case of intercalation compounds, the electrode should also present an appreciable ionic conductivity to enable the chemical species involved in the redox reaction to diffuse inside the electrode. On the other hand, the critical roles of the electrolyte are allowing ionic transport between the two half-cells, and at the same time, avoiding internal electronic current between them. A separator is typically employed to prevent mixing of the electrolytes, but in most cases, both half-cells use the same electrolyte, so that the electrochemical cell consists of two electrodes in contact with a single electrolyte [1–3,5].

One of the most relevant properties of electrochemical cells is the electrical potential established between the two half-cells, also called *efm*. The electrical potential (E) is a physical quantity that can be only determined in reference to other condition of the system. As a consequence, the electrical potential of a single half-reaction (e.g., a single electrode immersed in an electrolyte) cannot be measured directly. Thus E is always determined in reference to another half-reaction. Therefore, it was adopted by convention to measure E of a half-cell in relation to the standard hydrogen electrode (SHE) using standard conditions of concentration, temperature, and pressure. In summary, SHE was arbitrarily assigned as the half-cell electric potential equal to zero. The difference of potential between SHE and any half reduction reaction is called the standard electrode potential (E_0). Based on this convention, the following signals are used to define the oxidation or reduction nature of a half-reaction:

- $E_0 > 0$, indicates that the chemical species is a stronger oxidative agent than H^+

- $E_0 < 0$ indicates that the chemical species is a stronger reductive agent than H^+

Table 2.1 lists E_0 values for half-reactions of some elements and substances in aqueous solution. For instance, lithium (Li) is the pure element with strongest reductive potential and Fluorine (F) is the element with strongest oxidative potential. The main advantage of adopting E_0 is because it allows determining cell potentials of any two half-reactions that are expressed in reference to SHE [3,7,8]. As an example, one can determine the theoretical value of E_0 for the galvanic cell depicted in Figure 2.1 by using values of E_0 given in Table 2.1. The standard theoretical potential (E_{Th}) from the overall reaction can be calculated by adding the E_0 from the two half-reactions. However, attention should be paid here because the value of E_0 from the half-reaction of zinc must be inverted since it occurs in the opposite direction in the concerned galvanic cell. As a consequence, E_{Th} of the galvanic cell (Figure 2.1a) will be approximately +1.1 V. In case of the electrolytic cell (Figure 2.1b), the value of E_{Th} for the half-reaction of copper is the one that must be inverted, resulting in an electric potential of -1.1V.

Moreover, E_{Th} provides thermodynamic information about the spontaneity of the chemical reactions involved in the electrochemical process. E_{Th} can be directly related to the so-called Gibbs free energy (ΔG°) using Eq. 2.1.

$$\Delta G = -n.F.E_{Th} \qquad \text{(Eq.2.1)}$$

Here, n is the number of electrons transferred in the reaction (in this case two), and F is a proportionality constant, called the Faraday constant [3,8]. Thus, the Fluorine (F) half-reactions showed in the last row of Table 2.1 will proceed spontaneously in the direction showed while the Lithium (Li) half-reaction showed at the first row of the Table 2.1 will proceed in the opposite direction described. The same rationale can be applied to galvanic and electrolytic cell depicted in Figure 2.1. By employing the previously determined values of E_{Th} in Eq. 2.1 we can promptly see that the overall reaction of the galvanic cell is spontaneous ($\Delta G° < 0$). The opposite is also true for the electrolytic cell where the resulting E_{Th} of -1.1V essentially gives a positive value of ΔG°.

Table 2.1 - Standard electrode potentials in aqueous solutions relative to standard hydrogen electrode (SHE) [28- 30].

Half-reaction	E_o (V)
$Li^+ + e^- \leftrightarrow Li\ (s)$	-3.04
$Na^+ + e^- \leftrightarrow Na(s)$	-2.710
$Zn^{2+} + e^- \leftrightarrow Zn(s)$	-0.760
$Fe^{2+} + 2e^- \leftrightarrow Fe(s)$	-0.440
$Cd^{2+} + 2e^- \leftrightarrow Cd(s)$	-0.400
$Pb^{2+} + 2e^- \leftrightarrow Pb(s)$	-0.126
$2\ H^+ + 2e^- \leftrightarrow H_2(g)$	0.000
$Cu^{2+} + 2e^- \leftrightarrow Cu(s)$	+0.337
$I_2(s) + 2e^- \leftrightarrow 2I^-(s)$	+0.535
$Ag^+ + e^- \leftrightarrow Ag(s)$	+0.779
$O_2(g) + 4H^+ + 4e^- \leftrightarrow 2H_2O(l)$	+1.230
$Cl_2\ (g) + 2e^- \leftrightarrow 2Cl^-$	+1.36
$F_2\ (g) + 2e^- \leftrightarrow 2F^-$	+2.87

Current (I) is also a variable of great interest in electrochemical cells. Combined with the electrical potential it gives the electric power (P) to be provided by the cell under discharge (P = I.E). The unit of power according to the international system of units (SI) is the Joule per second (J/s) or W (Watt). Current is related to the rate of the electrode reactions and is represented in units of A or Coulomb per second (C/s). Electrical potential has often units of Joule per Coulomb (J/C) or Volt (V) and, as mentioned before, is related to the cell electromotive force or the difference in potential between two half-cells. On the other hand, the electrical capacity of the cell (Q) is also an essential quantity since it gives the amount of electrical charge storage. It is given by the product of the current provided by the cell during a interval of time ($Q = i.\Delta t$). The SI units for capacity is A.s, but this quantity usually is presented in mA.h for practical reasons [1–3,5].

In general, the effective operating potential (E_{eff}) of an electrochemical cell is considerably lower than the standard theoretical potential, E_{Th}, due to possible losses caused by several factors. This drop of cell potential is mathematically stated by Eq. 2.2, where $(\eta_{ct})_a$ and $(\eta_{ct})_c$ are the charge-transfer polarizations at the anode and cathode, $(\eta_c)_a$ and $(\eta_c)_c$ are the concentration polarizations at the anode and cathode, i is the cell operating current, R_i is the internal resistance of the cell and R is the apparent cell resistance.

$$E_{eff} = E_{Th} - [(\eta_{ct})_a + (\eta_{ct})_c] - [(\eta_c)_a + (\eta_c)_c] - iR_i = iR \quad \text{(Eq. 2.2)}$$

Activation and concentration polarizations are connected to the kinetics of charge transfer and mass transfer, respectively. On the other hand, the internal resistance (R_i) is affected by the electrical conduction properties of various materials and their interfaces. R_i can be broken down into the cathode, anode, and electrolyte ionic resistances, the electronic resistances of cathode and anode, and the interfacial resistances between all constituent parts of the electrochemical cell. Therefore, the efficiency of an electrochemical cell depends not only on the E_0 of the chosen electrodes but also on the properties and compatibility of all materials that make up the electrochemical cell [1–3,5]. In this survey, the ionic resistance is the central issue, and it is intimately linked with ionic transport in condensed matter.

2.2 Ionic Transport in Solids

In condensed materials, ionic migration, also referred as ionic conduction, hopping or diffusion, is governed by random jumps of ions, leading to position exchange with their neighbors. However, the ionic migration mechanisms in solid-state conductors are significantly different from those in liquid. Ion transport in liquid involves a coupled mechanism between the mobile species and the medium since the medium is also relatively mobile. Thus, the ionic diffusion is frequently described by Stokes−Einstein equation which considers the viscosity of the medium, which in turn can be modeled with Vogel−Tammann−Fulcher (VTF) or Mauro–Yue–Ellison–Gupta–Allan (MYEGA) equations [9]. In contrast, diffusion in solids is usually characterized by a tremendous difference of the species mobilities in the system. Consequently, some species are considered mobile while others are considered as a rigid framework through which mobile species must pass [1,4,10–12]. This section will be mostly devoted to ionic transport in solids since the main subject of this work is the development of solid electrolytes.

In most ionic solids, ions are trapped on their lattice sites. They vibrate continuously at infrared frequencies (~10^{13} Hz) but rarely have enough thermal energy to escape from their lattice sites. If they are able to escape and move into adjacent lattice sites, the requirements for ionic conduction are reached. Ionic

conduction is easier at higher temperatures and especially if crystal defects are involved. In an ideal solid at 0K (defect-free), there are no atom vacancies, and interstitial sites are empty. For ionic conduction to occur, the minimum requirement is that either some sites are vacant and adjacent ions can hop into the vacancies leaving their sites vacant, or ions in their regular position can hop into adjacent interstitial sites. At higher temperatures, ions have greater thermal energy and also defect concentrations are higher [4,11–13].

Ionic migration mechanisms for solids can be primarily classified into two broad categories: vacancy-mediated and interstitial-mediated migration mechanisms. Figure 2.2 shows a schematic representation of these two categories of migration mechanisms. In vacancy-mediated migration, a number of sites that would be occupied in the ideal structure (defect-free) are in fact empty, perhaps due to either a thermally generated (intrinsic defects) Schottky defects (cation and anion vacancies), or the presence of charged impurities (extrinsic defects). An ion adjacent to a vacancy may be able to hop into it, leaving its site vacant (Figure 2.2a). This process is regarded as vacancy migration, although, are the ions and not the vacancies that hop. Interstitial sites are defined as those that would usually be empty in an ideal crystal. Occasionally, in real solids, ions may be displaced from their lattice into interstitial sites generating Frenkel defects (intrinsic defects). Once this happens, the ions in interstitial sites can often hop into adjacent interstitial sites (Figure 2.2b). In either case, these jumps may be one step in a long-range conduction process. [1,4,11–13].

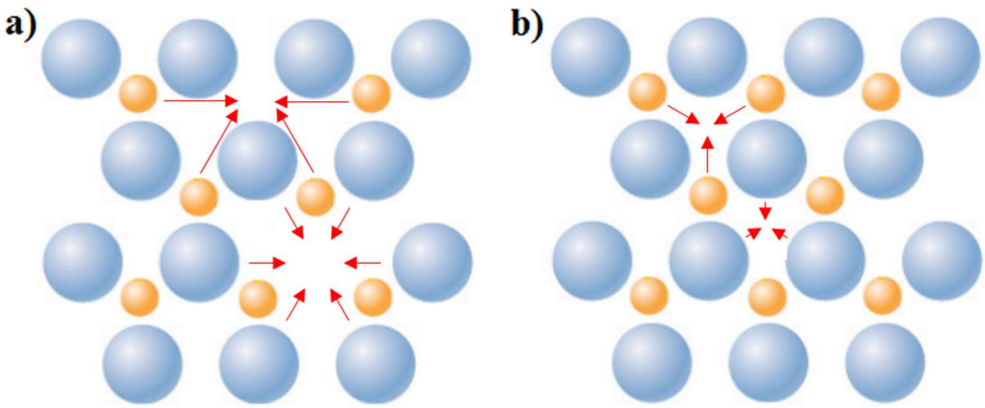

Figure 2.2 - Two-dimensional scheme of (a) vacancy-mediated and (b) interstitial-mediated migration mechanisms.

The ionic conductivity can be defined according to Eq. 2.3, as the product of concentration (n*), mobility (μ) and associated charge (*Ze*) of the charged carriers. The concentration of charge carriers is usually expressed under volumetric units (cm^{-3}) and is a thermoactivated process once the creation of defects usually requires energy. The charge associated with the charge carrier is essentially the product of the electron charge (1.602 x 10^{-19} C) and the valence of the charged carrier. On the other hand, the mobility is described as the drift velocity under an applied electric field ($cm^2.V^{-1}.s^{-1}$). This equation is considerably general and defines conductivity for all types of ionic conductors [4,11–13].

$$\sigma = n^* Ze\mu \qquad \text{(Eq. 2.3)}$$

The formation of charge carriers is directly linked with the Gibbs free energy necessary for formation of defects (ΔG_f) and the total concentration of the mobile specie in the material (n_0) which can be easily accessed if the chemical composition and density of the material are known. This relationship is usually expressed using Eq. 2.4, where T is the temperature, k_B is the Boltzmann's constant, ΔH_f and ΔS_f are the formation enthalpy and entropy associated with the formation of Schottky or Frenkel defects. In general, vacancy defects require larger amount of formation energies than interstitial defects.

$$n^* = n_0 e^{\left(\frac{\Delta S_f}{2k_B}\right)} e^{\left(-\frac{\Delta H_f}{2k_B T}\right)} \qquad \text{(Eq. 2.4)}$$

Regarding the mobility, an approach based on "*the theory of random walks*" is widely used to understand the nature of ionic transport. Even though it neglects conceivable complex mechanisms of ionic motion such as ionic cooperative motion, it is well-known for describing very well the dependence of ionic conductivity with the temperature. The ionic transport is approached as energetic barriers that separate two local minima along the mobile species pathway. This energy barrier, which is often referred to as the Gibbs free energy for ion migration (ΔG_m), dramatically influences ionic mobility, where low migration energies lead to high ionic mobility and conductivity. Just as ΔG_f, ΔG_m is also constituted by one entropic (ΔS_m) and one enthalpic (ΔH_m) term. The physical nature of the entropic term is not fully understood but can be rationalized as a configurational change in the structure in the surroundings of the sites involved

in the hop. On the other hand, the enthalpic term enthalpy is assigned as the enthalpy of charge carrier migration [1,4,11–13]. Figure 2.3 shows a one-dimensional schematic diagram of the enthalpic barrier that an ion need to overcome to move to the neighbor site (Figure 2.3a) and the force that the presence of an applied electric field ($\vec{E}$) causes over a carrier positively charged (Figure 2.3b).

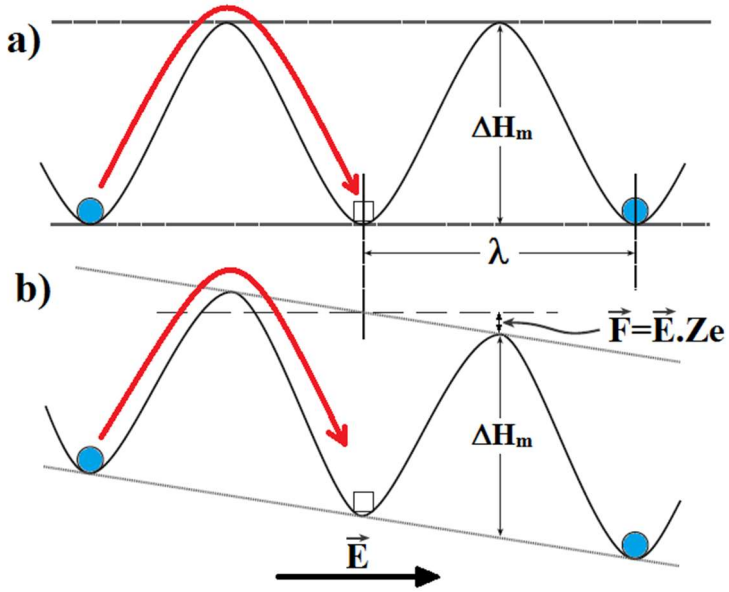

Figure 2.3 - One-dimensional schematic diagram of the enthalpic barrier that an ion need to overcome to move to the neighbor site: (a) in the absence of an applied field; (b) with an applied field ($\vec{E}$). $\vec{F}$ is the force that the applied electric field causes in a carrier positively charged, ΔH_m is the enthalpic barrier for ion motion and λ is the jump distance between sites.

For an ion to move through the lattice under the driving force of an electric field, it must have sufficient thermal energy to pass over the intermediate position between sites. In the one-dimension case, the mobility of the ion will be a function of its characteristic attempt frequency (v), the jump distance (λ), and the probability of a successful jump of the thermally activated mechanism. Therefore, the expression for ionic mobility (μ) can be described using Eq. 2.5.

$$\mu = \frac{Ze.\nu.\lambda^2}{k_B T} e^{\left(\frac{\Delta S_m}{k_B}\right)} e^{\left(-\frac{\Delta H_m}{k_B T}\right)} \qquad \text{(Eq. 2.5)}$$

Hence, it is possible to describe the dependence of ionic conductivity on temperature by combining Eq. 2.3 and Eq. 2.4 and Eq. 2.5, which gives rise to the Eq. 2.6.

$$\sigma = \frac{n_0 Ze^2.\nu.\lambda^2}{k_B T} e^{\left(\frac{\Delta S_m + \Delta S_f/2}{k_B}\right)} e^{\left(-\frac{\Delta H_m + \Delta H_f/2}{k_B T}\right)} \quad \text{(Eq. 2.6)}$$

A simplified form of Eq. 2.6 can be rewritten as an Arrhenius-like equation (Eq. 2.7). Here, σ_0' is called pre-exponential term and contain several physical parameters ($n_0.Ze^2.\nu.\lambda^2/k_B$) including entropy contributions ($e^{[(\Delta Sm+\Delta Sf/2)/kB]}$). Therefore, E_a' is known as the activation energy for ionic conductivity and has the contribution of the defect formation and migration enthalpy ($E_a' = \Delta H_f/2 + \Delta H_m$). The whole entropic term is generally close to the unity since the ΔS_f and ΔS_m are usually small compared to their dividend, k_B. Besides, in the special cases where the enthalpy of defect formation (ΔH_f) is neglectable the activation energy for ionic conductivity (E_a') is reduced to the enthalpy of migration (ΔH_m) [1,4,6,10–14].

$$\sigma T = \sigma_0' \; e^{\left(\frac{-E_a'}{k_B T}\right)} \quad \text{(Eq. 2.7)}$$

The foremost importance of Eq. 2.7 lies in the fact that measuring ionic conductivity as a function of temperature allows the estimation of E_a', which can be calculated from the slope of log(σT) vs. 1/T plot based on the linearized form of Eq. 2.5 ($\log[\sigma T] = \log[\sigma_0'] - \log[e].\, E_a'/[k_B.T]$). Moreover, Eq. 2.7 can be directly related to diffusivity equation ($D = D_0.\exp[-E_a/[k_B.T]]$) by means of the Nernst-Einstein equation and the Haven ratio [6,10,12,13]. A true Arrhenius-type equation (Eq. 2.8) is also widely used because it is simpler to use, once the linearized form of this equation ($\log[\sigma] = \log[\sigma_0''] - \log[e].\, E_a''/[k_B.T]$) implies data being plotted as log(σ) vs. 1/T to determine E_a". Therefore, the ionic conductivity can be promptly read in logarithmic scale in the plot while using Eq. 2.7 demands to isolate the temperature term to have access to ionic conductivity from plotted data [6,12]. Even though Eq. 2.8 has no theoretical bases, under general conditions the relative difference between E_a values obtained from this equation comparatively to Eq. 2.7 is around 10%.

$$\sigma = \sigma_0'' \; e^{\left(\frac{-E_a''}{k_B T}\right)} \quad \text{(Eq. 2.8)}$$

2.3 Electroanalytical Methods

In this section, the most important electroanalytical techniques usually employed to characterize solid electrolytes are introduced.

2.3.1 Direct current techniques

Electrical charge can be transported within solids by the motion of either electronic or ionic species. For materials with interest to be used as solid electrolytes, it is essential that the charge transport be predominantly related to ionic motion. Therefore, the determination of the real contribution of ionic and electronic conductivity to the total electrical conductivity of an electrolyte material is crucial. These quantities are defined as transference numbers of ions (t_i) and electrons and/or holes (t_{el}), and are described according to Eq. 2.9 and Eq. 2.10:

$$t_i = \frac{\sigma_i}{\sigma_i + \sigma_{el}} \quad \text{(Eq. 2.9)}$$

$$t_{el} = 1 - t_i \quad \text{(Eq. 2.10)}$$

where σ_i and σ_{el} are the ionic and electronic contribution to the total electrical conductivity, respectively. Several methods, most of them using direct current techniques, have been proposed to determine ionic and electronic transference number in varied materials. However, these methods have various boundary conditions, and they are valid under strict experimental conditions or limited to some types of electrical conductors. Perhaps, the greatest challenge in solid-state electrochemical currently is to develop a theory and/or a method that allows the determination of transference number for all kind of conductor materials. Still, some methods have already been used in particular conductor materials and had its efficacy evidenced. Among the most used methods, it can be cited, the *efm* method, Tubandt's method and Wagner's method [6,15,16].

The simplest method is to measure the *ocv* of a system under a potential chemical gradient. Thus, a galvanic cell with an assemblage M|MX|X is used, where M and X are usually pure elements and MX is a compound. Under open circuit conditions, neither chemical species nor electronic current can be transported externally from one electrode to the other because a voltmeter with virtually infinite resistance is usually employed. Then, the cell should behave in a

thermodynamically reversible way and produce its maximum potential. If ΔG^o of the predicted cell reaction is known and electronic conductivity is absent, E_{ocv} is equal to the E_{Th}, which can, in turn, be calculated based on Eq. 2.1 presented in section 2.1. On the other hand, if there is electronic leakage through the electrolyte, the measured voltage is given by Eq. 2.11. In summary, t_i is the ratio between the E_{ocv} and E_{Th}. This method requires that well-defined and known thermodynamic conditions are maintained at each of the two electrodes, which can sometimes be difficult to achieve [6,15–18].

$$E_{ocv} = E_{Th} t_i = -t_i \frac{\Delta G^o}{nF} \quad \text{(Eq. 2.11)}$$

Tubandt's method is also conceptually straightforward, being merely a coulometric determination in a solid-state system. An electrolytic cell is used, usually assembled from disks comprising identical cathode and anode and three electrolyte regions, each of which can be separated. The cathode and anode are not blocking to either ions or electrons and must be reversible. The imposition of a direct current (DC) of known interval of time and magnitude causes changes in the weights of the two electrodes where the gain of mass of the cathode should be consistent with the loss of the anode. The two electrodes are weighted, and the average mass (m_a) can be calculated by using the lost and the gain of the mass of electrodes. The current that passes through the cell is integrated with respect to time, and the mass theoretically transferred if the current were purely ionic (m_{th}) can be calculated if the atomic weight of the transporting ionic species is known. The ratio between the measured and the theoretical mass gives the value of the ionic transfer number (Eq. 2.12) and, thus, also that of the electronic transference number. In practice, the disks tend to stick together. Nevertheless, the method is widely used and is quite robust regarding the type of material [6,15,16].

$$t_i = \frac{m_a}{m_{th}} \quad \text{(Eq. 2.12)}$$

Wagner’s method is probably the most used DC technique and is especially useful for the evaluation of low levels of electronic conductivity in materials that are primarily ionic conductors. The general idea behind this method involves the independent measurement of the current carried by minority electronic species

under conditions such that ionic transport is prevented. This approach involves the use of one electrode that is reversible to both ions and electrons and another electrode that blocks the mobile ionic species. These conditions are accomplished by using an electrode that does not contain atoms of the mobile ionic species and polarizing the cell in such a way that they tend to move away from that electrode into the electrolyte. Since the electrode cannot supply those ions, the electrolyte becomes locally starved, and ionic transport is prevented. The polarity must be correct in such a way that, if the mobile ionic defects are positively charged, this electrode must be made positive relative to the other electrode. If the defects carry negative charges, this ionic defect-starving mobile ionic electrode must be on the negative side of the experimental cell. When a potential below the decomposition potential of the electrolyte is applied to the cell, ionic migration will occur until the concentration-induced chemical potential gradient balances the applied field. At the resulting steady state, the cell is polarized, and any residual current flows because of electron and/or hole migration across the electrolyte and the interfaces. When the electrolytic species is a cation, the steady-state electronic current will be described by Eq. 2.13, and if the electrolytic species is an anion by Eq. 2.14:

$$\mathrm{I_{el}} = \mathrm{I_e} + \mathrm{I_h} = \frac{\bar{\mathrm{R}}\mathrm{TA}}{\mathrm{LF}}\left\{\sigma_\mathrm{e}\left[1 - \mathrm{e}^{\left(\frac{-\mathrm{EF}}{\bar{\mathrm{R}}\mathrm{T}}\right)}\right] + \sigma_\mathrm{h}\left[\mathrm{e}^{\left(\frac{\mathrm{EF}}{\bar{\mathrm{R}}\mathrm{T}}\right)} - 1\right]\right\} \qquad \text{(Eq. 2.13)}$$

$$\mathrm{I_{el}} = \mathrm{I_e} + \mathrm{I_h} = \frac{\bar{\mathrm{R}}\mathrm{TA}}{\mathrm{LF}}\left\{\sigma_\mathrm{e}\left[\mathrm{e}^{\left(\frac{\mathrm{EF}}{\bar{\mathrm{R}}\mathrm{T}}\right)} - 1\right] + \sigma_\mathrm{h}\left[1 - \mathrm{e}^{\left(\frac{-\mathrm{EF}}{\bar{\mathrm{R}}\mathrm{T}}\right)}\right]\right\} \qquad \text{(Eq. 2.14)}$$

where I_{el}, I_e, and I_h are the electronic current and its partial contributions because of electrons and hole. σ_e and σ_h are the partial contributions to conductivity due to electrons and holes, respectively. A and L are the electrode area and thickness of the sample and $\bar{\mathrm{R}}$ is the gas constant. Accordingly, if the electronic current (I_{el}) is measured under steady-state conditions at different potentials, a plot of $[I_{el}(LF/\bar{R}TA)]/[e^{(EF/RT)}-1]$ vs. $e^{(-EF/RT)}$ will give a straight line with σ_e as slope and σ_h as intercept for a mobile cation system and the inverse for a mobile anion system [6,16,18–20].

2.3.2 Alternating current techniques

Conductivity measurements are typically carried out under alternating current (AC) conditions because polarization effects are minimized. In experiments using DC signals, for example, it is fundamentally impractical to separate the effects of electrode polarization from the actual ionic resistance of the sample. In contrast, the use of AC signal in variable frequencies allows separating the effects of polarization of electrodes in most cases, since in general, these effects present quite different frequency-domain response from that one of of the concerned material. Also, the electrodes may be any inert metal (under the measurement conditions), thus eliminating the need for reversible electrodes which would be required to eliminate electrode polarization in measurements using DC signals. The experimental technique which uses AC signal in varied frequency as a method to characterize electrical and electrochemical properties of materials and their interfaces is called electrochemical impedance spectroscopy (EIS). The determination of ionic conductivity using EIS is probably the most widespread application of this technique since it provides information difficult to obtain by other methods [6,21–25].

Many electrochemical parameters including conductivity are a function of the applied frequency. This is because the alternating current is out-of-phase with the applied AC electrical potential, and this affects differently the various processes within the cell (surface, interfacial, and bulk ionic transport, double layer, charge-transfer reactions, among others) depending on the frequency of the AC signal. Since the stimulus and response are time-domain signals, impedance is often presented as complex quantity as a function of the frequency of AC signal [21,22,24,25].

In lay terms, the complex impedance can be defined as a “complex resistance” encountered when current flows through a circuit composed of resistors, capacitors, and inductors. In other words, impedance reflects the ability of a circuit to resist the flow of electrical current, represented by the real part of the impedance (or in-phase part), but it also reflects the ability of a circuit to store electrical energy, represented by the imaginary part of the impedance (or out-of-

phase part). In experimental situations, the electrochemical impedance is usually measured using AC potential signals with small amplitude applied in a broad frequency range, expressed in Hz or s^{-1}. Figure 2.4a shows typical sine signals of applied potential and the resulting current out of phase in time domain by an angle ϕ [3,21–24].

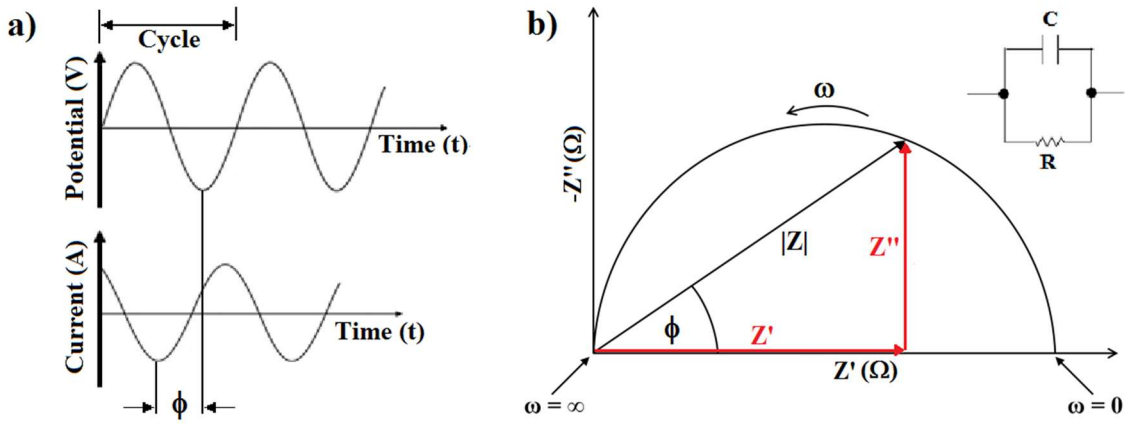

Figure 2.4 – Graphical representation of (a) typical sine signals out of phase by an angle ϕ and (b) complex impedance plot for an ideal RC circuit (resistor in parallel with a capacitor).

Similar to the resistance, impedance is the ratio between the AC applied potential (E), given in units of V, and the measured current (I), given in units of A. An expression analogous to Ohm's Law (Eq. 2.15) allows to calculate the impedance of the system as the ratio of input potential and output measured current as a function of time (t). The impedance is therefore expressed in terms of a magnitude |Z|, and a phase shift angle, ϕ, as a function of the angular frequency (ω) and the time.

$$Z^* = \frac{E(t)}{I(t)} = \frac{E\ \sin(\omega t)}{I\ \sin(\omega t+\phi)} = |Z|.\frac{\sin(\omega t)}{\sin(\omega t+\phi)} \qquad \text{(Eq. 2.15)}$$

Using Euler's relationship, it is possible to express the impedance as a complex function (Eq. 2.16). The impedance is then represented as a complex number that can also be expressed in complex mathematics as a combination of real (Z') and imaginary (Z") parts linked by the phase angle ϕ. Figure 2.4b shows a typical complex impedance plot for an ideal RC circuit (a parallel assemblage of a resistor and a capacitor). The semicircle shape of the impedance response is

characteristic of the RC assemblage. The resistance of this circuit can be promptly read at the low-frequency intercept in the real axis (semicircle diameter) [6,21–24].

$$Z^* = \frac{|E|e^{j\omega t}}{|I|e^{j\omega t - j\phi}} = |Z|e^{j\phi} = |Z|.(\cos\phi + j\sin\phi) = Z' + jZ'' \quad \text{(Eq. 2.16)}$$

In principle, the various forms of impedance spectra provide detailed and separate information about many of the processes within the electrochemical cell. The determination of properties is typically made by comparing the experimental plots with those that would have been generated by model systems called equivalent circuits (EC). These consist of simple circuit elements with well-known impedance behavior like resistances, capacitances and/or inductances in appropriate series and/or parallel combinations. In the case of the EC of Figure 2.4a, a mathematical expression that describes this shape can be easily derived based on the isolated impedance response of a resistor and capacitor, considering a parallel assemblage of these circuit elements, and using fundamentals of the theory of electrical circuits. A parallel combination of a resistor and a capacitor (RC circuit) is used for example to represent the impedance response of a monocrystalline electronic conductor. A monocrystalline ionic conductor, on the other hand, would present an additional capacitive effect due to ion-blocking phenomenon at the metallic electrode responding at low frequencies and could be represented by an $[R_1 \mid C_1] - C_2$ equivalent circuit [3,6,21,22,24,25].

In the case of composite or polycrystalline materials, sometimes it is possible to identify and separate the contribution of each phase, it means grain and grain boundary contributions, because the relaxation frequencies of these contributions are different enough to give distinct impedance response as a function of frequency. Several models for two-phase microstructure have been proposed, but the simplest cases are two phases stacked in layers parallel to the electrodes (series layer model) or two phases stacked in layers perpendicular to the electrode (parallel layer model). In the series layer model, EC is represented by two RC's circuits in series ($R_1 \mid C_1$ - $R_2 \mid C_2$) while in the parallel model by two RC's in parallel ($[R_1 \mid C_1] \mid [R_2 \mid C_2]$). Figure 2.5 shows schematics complex

impedance plots typical of ionic conductors for the series (Figure 2.5a) and parallel (Figure 2.5b) layer models. In the case of the series layer model, the complex impedance plot shows two well-resolved semicircles when the capacitances associated with the two phases are very different from each other (C_2 / C_1 ≥ 10^3). On the other hand, in the model of parallel phases, the contributions of each resistance are theoretically indeterminable. Differences in resistances also turn feasible the differentiation of contributions, but this difference will be better visualized in other immittance formalisms [3,21,22,24,25].

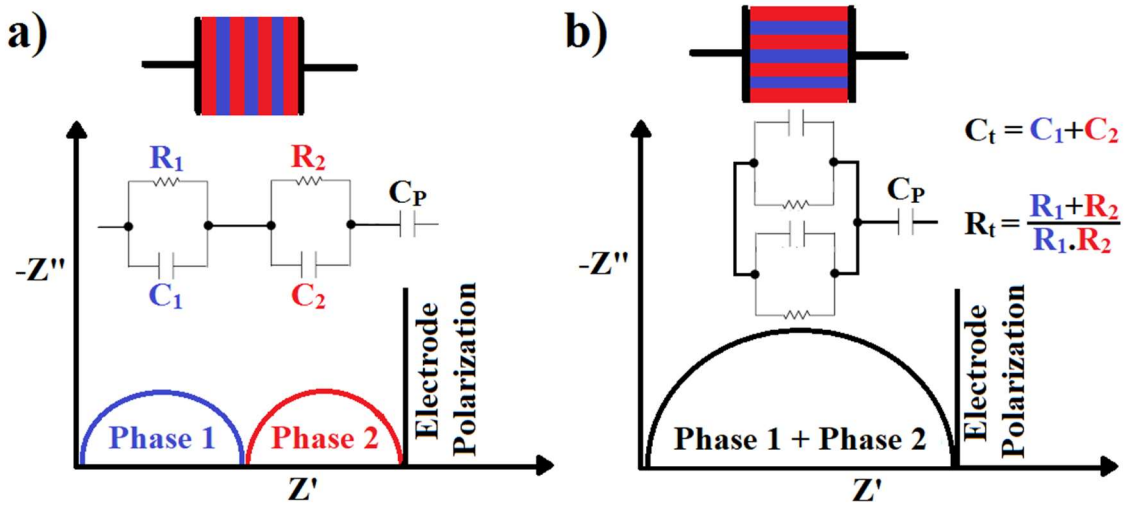

Figure 2.5 – Schematic representation of complex impedance plots typical of ionic conductors in two microstructural models: (a) series layer model; (b) parallel layer model.

In polycrystalline materials, grains and grain boundaries can be represented by using a more realistic model so-called brick layer model. This model consists of a three-dimensional array of blocks (grains) staked together in which the surface of contact between blocks is considered as a different phase (grain boundaries). Since grains have bulk shapes and grain boundaries surface shape, the resulting capacitance of these microstructural components tend to be very different (usually more than two orders of magnitude). Them, if the grain is much more conductive than the grain boundaries, which usually is the case, the conductivity along the grain boundary is negligible, and the serial phase model can be used to represent the polycrystalline material, and the different

contributions can often be resolved (Figure 2.5a). In contrast, if the grain contour is much more conductive than the grain and the current is primarily driven by the contours, the parallel phase model is better suited to represent the microstructure, and only the total conductivity can be determined (Figure 2.5b) [21,24,25].

2.3.3 Voltammetry

Voltammetry is the study of current as a function of applied potential and it is a category of electroanalytical methods used in analytical chemistry and in the energy field of electrolysis and battery technologies. Voltammetric techniques present irreplaceable tools due to their robustness and ability to provide a vast amount of important thermodynamics and kinetics information. Although there are a number of different voltammetric methods used in electroanalytic studies, linear sweep voltammetry (LSV) and cyclic voltammetry (CV) are the most widely used ones. In LSV the potential is scanned from a lower limit to an upper limit using a fixed scan rate. The scan rate is the difference between the upper and the lower potential divided by the sweep time between those potentials and is expressed in units of Volt per second (V/s). The resulting current is measured as an output signal and is plotted as a function of potential rather than time. CV is very similar to LSV but, in this case, the potential is swept between two values until it reaches the upper limit, then, the scan is reversed, and the potential is swept back to the initial potential. Therefore, the only fundamental difference between these methods is that in LSV the potential is scanned in just one direction and in CV the potential is scanned forward and backward. Figure 2.6a shows a typical CV input signal in which a DC potential is linearly increased with time from an initial potential E_1 until the upper limit E_2 when the scan rate is reversed [3,8,26,27].

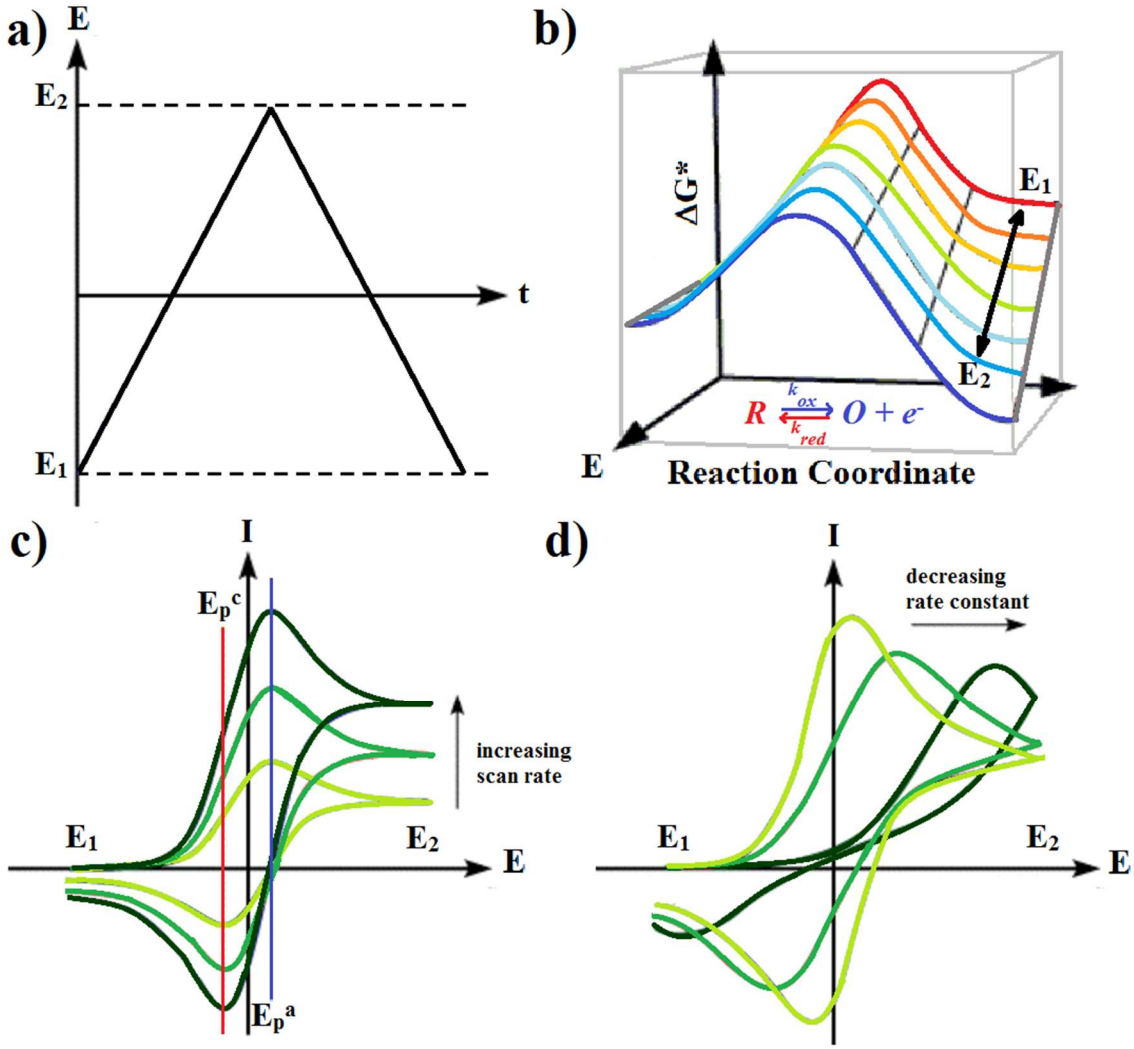

Figure 2.6 – Set of schematic plots presenting: (a) the applied DC potential as function of time under fixed scan rate; (b) the effects of a potential change on the standard free energies of activation for oxidation and reduction; (c) the dependence of the peak current on the experimental scan rate; (d) the dependence of the potential peak current on the rate constant of reactions when the scan rate is significantly faster than it.

Common voltammetry experiments are conducted in the liquid state. The concerned material is typically introduced in aqueous or organic medium, and the resulting solution is called analyte. The electrochemical cell to conduct LSV and CV experiments must have at least two electrodes. However, modern electrochemical cells are constituted of a three-electrode system, namely, work, counter and reference electrodes. The working electrode, which contacts the

analyte, must apply the desired potential in a controlled way and facilitate the transfer of charge to and from the analyte. The counter electrode acts as the other half-cell balancing the charge added or removed by the working electrode. In the two-electrode assemblage, the counter electrode also suits as a comparison potential to gauge the potential of the working electrode. However, it is extremely difficult for an electrode to maintain a constant potential while passing current. Then, a third electrode in which no current flows is added to provide a reference potential for measuring and controlling the working electrode's potential. The reference electrode is essentially a half-cell with a known reduction-oxidation potential [3,7,8,26,27].

Similarly to any chemical system, the rate of electrochemical reaction can be changed by temperature, pressure and the concentration of reactants. However, an additional control parameter for the rate of electrochemical reaction is the electrode potential (E). Its absolute value is not accessible to measurements, so the zero of electrode potential scale is set by the introduction of a SHE or other reference electrode scale. For simplicity, we will consider here a single electron transfer reaction between two species (O) and (R). If no current is passing through the metal/solution interface, the electrode is rested on its equilibrium, reversible, potential (E_{eq}) given by the Nernst equation (Eq. 2.17).

$$E_{eq} = E_0 + \frac{\bar{R}T}{nF} \ln \frac{a_o}{a_R} \qquad \text{(Eq. 2.17)}$$

Where E_0 is the standard electrode potential of the O/R reaction couple ($R \leftrightarrow O + e^-$) and a_o and a_R are the activity of O and R species, which are linked to the concentration of these species in solution. If the current is passing through the electrode, the electrode potential will be different from E_{eq}, so we say that the electrode is polarized. This condition is called overpotential (η) and is simply defined as the difference between the applied electrode potential (E) and the equilibrium potential E_{eq}. As an example, for most of the electrochemical reactions, an increase of the overvoltage of approximately 100 mV increases the rate of electrochemical reaction in one order of magnitude. This additional variable of control is what makes the difference between chemical and electrochemical systems: by controlling electrode potential (or overvoltage) the

rate of the reaction can be finely controlled or increased tremendously [3,7,8,22,24,26,27].

Unlike equilibrium measurements, in voltammetric analysis, there is a flow of current around an electrical circuit. This current can be controlled by a number of factors, but the two most important are the rate of electron transfer between the metal and species in the analyte and the transport of material to and from the electrode interface. Under a fixed overpotential, the current flowing in reductive or oxidative directions at time zero can be predicted using the Eq. 2.18 and Eq. 2.19:

$$I_c = -FAk_{red}[O]_s \quad \text{(Eq. 2.18)}$$

$$I_a = -FAk_{ox}[R]_s \quad \text{(Eq. 2.19)}$$

where I_c and I_a are the cathodic and anodic current, k_{red} and k_{ox} are the rate constant for electron transference for reduction and oxidation and $[R]_s$ and $[O]_s$ are the concentration of R and O species at the surface of the electrode, respectively. The rate constants, k_{red} and $k_{ox,}$ are influenced by the applied potential according to Eq. 2.20 and Eq. 2.21.

$$k_{red} = A_{red}e^{\left[\left(-\frac{\Delta G^*_{red}}{\bar{R}T}\right)\left(\frac{-\alpha F(E-E_{eq})}{\bar{R}T}\right)\right]} \quad \text{(Eq. 2.20)}$$

$$k_{ox} = A_{ox}e^{\left[\left(-\frac{\Delta G^*_{ox}}{\bar{R}T}\right)\left(\frac{(1-\alpha)F(E-E_{eq})}{\bar{R}T}\right)\right]} \quad \text{(Eq. 2.21)}$$

These equations are derived from the transition state theory of chemical kinetics. Here, A_{red} and A_{ox} are pre-exponential factors coming from an Arrhenius-type equation and ΔG^*_{red} ΔG^*_{ox} are the standard free energies of activation for reduction and oxidation, respectively. The term α is known as the transfer coefficient. It arises because only a fraction of the total energy placed into the system (in the form of the applied potential) lowers the activation energy barrier. Its value varies from zero to unity (often ~ 0.5) depending on the shape of the free energy surfaces for the reactants and products [3,7,8,24,26,27].

Figure 2.6b shows a schematic representation of the effect of a potential change in the standard free energies of activation for oxidation and reduction. In summary, Eq. 2.20 and Eq. 2.21 express the dependence of the standard free energies of activation for redox process on the applied potential. Now consider

the special case in which the interface is at equilibrium with a solution in which $[R]_s = [O]_s$. In this situation, $E = E_{eq}$ and $\Delta G^*_{red} = \Delta G^*_{ox}$ (green line, Figure 2.6b), so that $k_{red} = k_{ox}$. Thus, E_{eq} is the potential where the forward and reverse rate constants have the same value. Then, the combination of Eq. 2.18 and Eq. 2.19 with Eq. 2.20 and Eq. 2.21, gives the so-called Butler-Volmer equation (Eq. 2.22):

$$I = FAk_0\left\{[O]_s e^{\left[\left(\frac{-\alpha F(E-E_{eq})}{\bar{R}T}\right)\right]} - [R]_s e^{\left[\left(\frac{(1-\alpha)F(E-E_{eq})}{\bar{R}T}\right)\right]}\right\} \qquad \text{(Eq. 2. 22)}$$

where k_0 is the standard rate constant and merely represents a measure of the kinetic facility of a redox couple. A system with a large k_0 will achieve equilibrium on a short time scale, but a system with small k_0 will be sluggish [3,7,8,22,24,26,27].

The mathematical treatment for transport of material to and from the electrode interface is even more complicated than the electron transfer kinetics. Mass transfer in solution might occur by diffusion, migration, and convection. Diffusion and migration result from a gradient in electrochemical potential. Convection results from an imbalance of forces in the solution. Commonly, the mathematical treatment is conducted by using several boundary conditions suitable for each type of experiment, the geometry of electrodes and for the mechanism of mass transfer that might be controlling the overall process. These mathematical treatments are out of the scope of this work, but they can be found in more details elsewhere [3,8]. However, it is essential to have a notion of the phenomena for the overall understanding of voltammetric analysis. For a fixed overpotential in a diffusion-controlled case, the current will drop as the reactions take place because the reactants are consumed in the surface of the electrode, decreasing in concentration and giving rise to a depletion region, the so-called diffusion layer. The current will drop with time, being proportional to the square root of the diffusion coefficient of the concerned chemical specie in solution ($D^{1/2}$) and inversely proportional to the square root of time ($t^{-1/2}$) [3,7,8,26,27].

Qualitatively, the exact form of the voltammogram can be deduced by considering the potential and mass transport effects. Let us consider that, at the electrode surface, an equilibrium is established, identical to that predicted by the Nernst equation (Eq. 2.15), and all species are in their reduced state. As the

voltage is initially swept from E_1 (reductive) to E_2 (oxidative) the equilibrium at the surface begins to alter, the current starts to flow, and the species are oxidized in a tentative to reestablish the equilibrium. Therefore, once the potential is continuously increased, the current increases because the system is getting far away from the equilibrium as the potential is swept toward more oxidative potentials. Eventually, the anodic peak occurs, since at some point the diffusion layer has grown sufficiently far from the electrode so that the flux of reactant to the electrode is not fast enough to satisfy that required by the Nernst equation. If the potential is swept back, the anodic current will continuously decrease until it begins to flow in the opposite direction and become a cathodic current since the oxidized species begin to be reduced. The anodic peak will occur for the same above-mentioned reason. Figure 2.6c shows a schematic cyclic voltammograms for a single redox couple reaction. In a reversible case, the potentials of the anodic and cathodic current peak are independent of the scan rate, and they are separated by the theoretical potential of 59/n mV, where n is the number of transferred electrons according to the redox reaction. The equilibrium potential of Nernst equation, $E_{eq,}$ is the average potential between the anodic and cathodic current peak. On the other hand, the peak currents are proportional to the square root of the diffusion coefficient and the scan rate. Therefore, when the rate constant is much faster than the scan rate, an increase of scan rate increases the peak current (Figure 2.6c). Although, if the rate constant is slower than the scan rate, the equilibrium predicted by the Nernst equation (Eq. 2.15) is not achieved and the theoretical separation between peaks is not respected. In such cases, the potentials of the anodic and cathodic current peak are dependent on the scan rate (Figure 2.6d) [3,7,8,26,27].

3 LITERATURE REVIEW

3.1 Rechargeable Batteries

The present energy economy based on fossil fuels is at serious risk due to a series of factors, including the continuous increase in the demand for oil, the depletion of non-renewable resources and the dependency on politically unstable oil-producing countries. Notwithstanding the unknown medium-to-long term implications of burning carbonaceous fuels and CO_2 emissions, which have increased at a constant rate with a dramatic jump in the last 30 years, resulted in a rise in global temperature with associated series of dramatic climate changes. Renewable sources offer potential game-changing clean energy, but they are intermittent, whether they come from the sun, wind, or waves. Besides, the gradual replacement of internal combustion engine cars by electric vehicles might also mitigate the CO_2 issue in the following years. All these intermittent systems would benefit from powerful energy storage units to properly balance source variability with the substantial variability in demand for power. Electrochemical energy storage possesses some desirable features, including pollution-free operation, high round-trip efficiency, and flexible power and energy characteristics to meet different functions, long cycle life, and low maintenance. As one of the most widely used technologies for electrochemical energy storage, rechargeable batteries stand out as the most important candidate in many industrial and household applications for the new energy economy from sustainable sources [28–31].

The first galvanic battery was developed by Alessandro Volta in the 1800s, and the first rechargeable battery was invented by Gaston Planté in 1859 when he designed the well-known lead-acid battery. Today, a rechargeable battery is typically composed of several electrochemical cells that are connected in series and/or in parallel to provide the required voltage and capacity, respectively. Each cell consists of a positive and a negative electrode (both sources of chemical reactions) separated by an ion conductive, electronically insulating medium (electrolyte). Once these electrodes are connected externally, electrons are forced to transfer from one electrode to the other through the external circuit. At the same time, the chemical reactions proceed simultaneously at both electrodes

and electroneutrality is ensured by ion transport across the electrolyte. The chemical reactions which generate the consumed energy are reversible, and the initial chemical energy can be restored by passing a reverse current through the battery, thereby recharging it. The energy density, expressed either in gravimetric ($W.h.kg^{-1}$) or volumetric ($W.h.l^{-1}$) units, that a battery is able to deliver is a function of the cell potential (V) and specific capacity ($A.h.kg^{-1}$), both of which are linked directly to the chemistry of the system. Figure 3.1 shows a schematic comparison of the different battery technologies regarding volumetric and gravimetric energy density.

Among the various existing technologies, Li-based batteries currently outperform other systems, accounting for 74% of 2015 worldwide sales values in portable batteries, followed by Ni–MeH (15%) and Ni-Cd (11%). Despite of the superior energy density of Li-metal battery (Fig. 3.1), this first technology has proven to be unsafe due to dendritic grow of lithium metal toward the electrolyte which led to explosion hazards. On the other hand, Li-ion cells solve the dendrite problem and are inherently safer than Li-metal cells, because of the presence of Li in its ionic rather than metallic state. Besides, its unique combination of high energy density and cyclability, made of Li-ion batteries the technology of choice for portable electronics, power tools, and hybrid/full electric vehicles. Therefore, there is high interest from both industry and government funding agencies, and the research in this field has abounded in the recent years [5,28,29,31,32]. Thus, the scope of this study is also centered in the Li-ion battery subject.

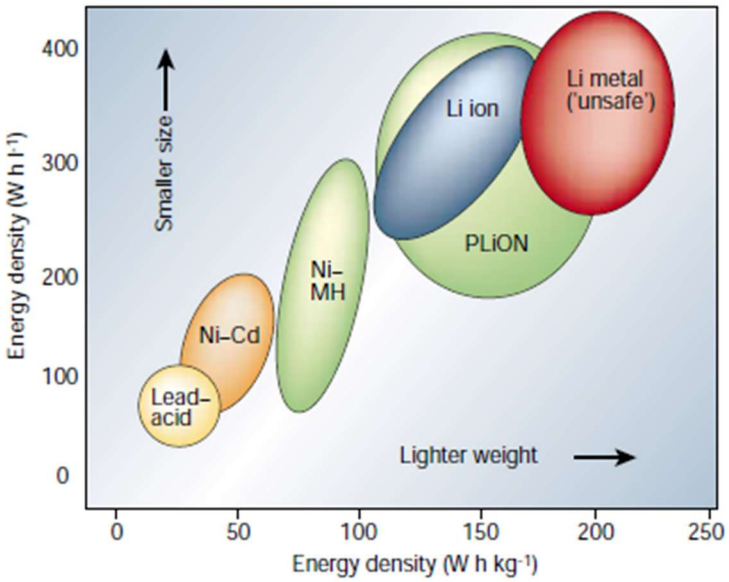

Figure 3.1 - Comparison of the different battery technologies regarding volumetric and gravimetric energy density [32].

3.2 Lithium-ion Batteries

Since the Sony Corporation first successfully marketed a commercial Li-ion battery in 1991, Li-ion battery technology has been applied to both thin, light, and flexible portable electronic devices and, more recently, to batteries for transportation systems including hybrid and electric vehicles. The high energy efficiency of Li-ion batteries may also allow their use in various electric grid applications, including improving the quality of energy harvested from wind, solar, geothermal and other renewable sources, thus contributing to their more widespread use and building an energy-sustainable economy. The rapid expansion of this market and popularization of this research field are meanly due to certain fundamental advantages that Li presents over other chemistries. Firstly, Li has the lowest reduction potential of any element, allowing Li-based batteries to have the highest possible cell potential. Also, Li is the third lightest element and has one of the smallest ionic radii of any single charged ion. These factors allow Li-based batteries to have high gravimetric and volumetric capacity and power density. Finally, Li^{+1} is one of the cations of highest mobility in solids, and since the rate-limiting factor for battery power performance is often the ionic

conductivity of electrolytes and electrodes, this also ends up being a determinant requirement [5,10,28,31,32].

The Li-ion electrochemical cell is typically composed of two electrodes, which have different chemical potentials and connected by an electrolyte. When these electrodes are connected by an external circuit, electrons spontaneously flow from the more negative to the more positive potential. Ions are transported through the electrolyte, maintaining the charge balance, and electrical energy can be tapped by the external loading. The cell converts stored chemical energy into electrical energy via redox reactions at the anode and cathode. Figure 3.2 shows a schematic representation of a typical Li-ion battery. Upon discharging, Li-ions are deintercalated from the graphite layers and intercalated into Li-intercalation compound. The process is reversed on discharge. The electrode materials of the first Li-ion cells were $LiCoO_2$ as cathode and coke as anode, with $LiPF_6$ salt dissolved in a mixture of organic solvents as electrolyte [5,30–33].

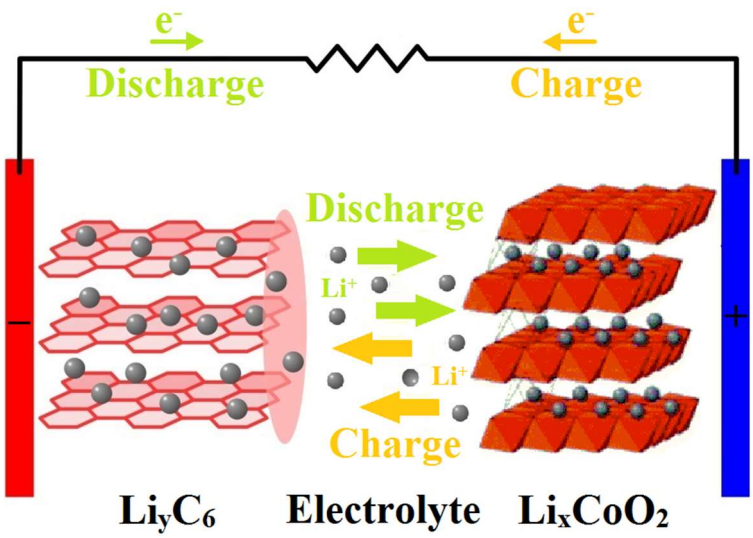

Figure 3.2 - The operation principle of the first commercialized Li-ion batteries. Lithium ions migrate back and forth between the negative and positive electrodes upon discharging/charging via the electrolyte, electrons doing so similarly via the outer electrical circuit.

As it happens for all technologies, the real battery is far from this oversimplified picture, once the electrodes themselves are complex systems

composed of a metallic current collector, the active compound ($LiCoO_2$ or C in this case), and additives that increase the electrical conductivity (typically various types of carbon). Polymeric binders (such as polyvinylidene fluoride) are also used to improve adhesion, mechanical strength and ease of processing. The electrodes are separated by a microporous polyethylene or polypropylene separator film, the whole system being impregnated with the electrolyte. While the voltage, capacity, specific energy and energy density are governed by the properties of bulk electrode materials, the cycle life is mostly dependent on the quality and stability of the several interfaces present. However, battery performance depends critically on the materials used, so the development of new materials is essential for advancing battery technology. The challenges faced by researchers in this field include the development of electrode materials with increased energy density, faster discharge kinetics and better stability. At the same time, there is an urgent need to find alternative non-flammable electrolytes that are stable over more extensive operating voltage windows [5,28,30–32,34]. This latter challenge is the focus of this study.

3.3 Electrolytes

In the case of electrolytes, the principal features are a high Li-ion conductivity ($>10^{-4}$ $S.cm^{-1}$) at operating temperatures (preferably ambient temperature) and negligible electronic conductivity over the operating range of lithium activity and temperatures. Another critical feature is electrochemical stability under the whole electrical potential window generated between anode and cathode, due to differences in chemical activity of Li-ion. In other words, the electrolyte must be inert while facing electrochemical reactions in the electrolyte/anode and electrolyte/cathode interface. Finally, as in all industrial developments, Li-ion electrolytes should be environmentally benign, non-toxic, non-hygroscopic, low-cost materials and their preparation should be easy. As mentioned before, conventional Li-ion battery electrolytes consist of $LiPF_6$ salt, or more recently $Li^+[CF^3SO^2NSO^2CF^3]^-$ salt, dissolved in a mixture of organic solvents, since these solutions offer very high ionic conductivities at operating temperature ($>10^{-3}$ $S.cm^{-1}$) and are compatible with the battery voltage operation

window. Commercial mixtures differ depending on the manufacturer, but generally contain two to four solvents, one of them always being ethylene carbonate. The main drawback concerns to this system are related to leakage demanding more complex cell project, and since these solvents are flammable substances, they cause safety concerns. Also, the demand for large-sized batteries makes the safety even a more serious issue, since increasing battery size, worsens the heat radiation and increases the amount of organic solvent [5,29,30,35,36].

In this respect, the replacement of currently used organic liquid electrolytes for solid electrolytes is expected to be a fundamental solution to the safety issue due to their non-flammability. Besides, they present advantages such as the simplicity of design once eliminates the need for containment of the liquid electrolyte, absence of leakage and pollution. Solid electrolytes used in lithium-ion batteries can be divided into two general classes of materials namely inorganic ceramics and organic polymers. Strictly, non-crystalline organic polymers are also liquids (supercooled liquid) in temperatures above T_g (glass transition temperature). However, the viscosity of polymers is often orders of magnitude higher than that of solvents at room temperature (RT). On the other hand, most of the inorganic solid electrolytes are single ion conductors. In case of Li-ion conductors, this means that only Li-ions are mobile while the rest of the species has very low mobility forming a rigid framework and maintaining the structural integrity of the electrolyte. Figure 3.3 presents a schematic representation of this fundamental difference in solid and liquid electrolyte [10,34,35,37].

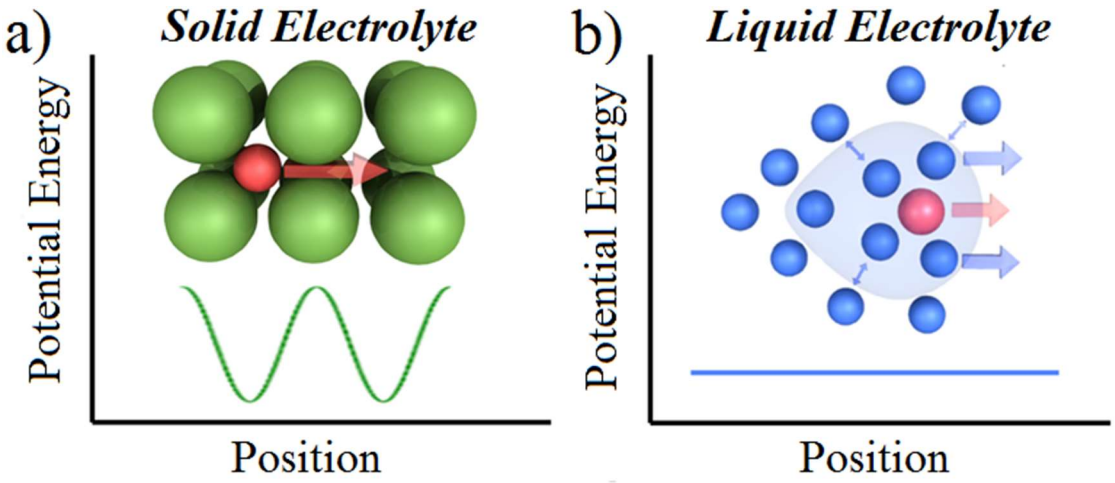

Figure 3.3 - Schematic representation of ion migration potential energy in crystalline solid (a), in which a mobile ion goes from one interstitial site to another, and liquid electrolyte (b), in which a mobile ion is solvated with a shell of electrolyte molecules moving them together as it moves (adapted from [10]).

Other noticeable difference between inorganic ceramics and organic polymers classes is the mechanical properties. The high elastic moduli of ceramics make them more suitable for rigid battery designs as in, for example, thin-film-based devices. Conversely, the low elastic moduli of polymers are useful for flexible battery designs. Also, polymers are usually easier to process than ceramics, which reduces the fabrication costs. On the other hand, ceramics are more suitable for high temperature applications or other aggressive environments. Currently, polymeric lithium ion conductors are market-leading. However, most systems are called “hybrid”, which means coupling a polymer with a plasticizing organic solvent, and may present the usual drawbacks related to the presence of liquid [29,32,34,35].

On the other side, disadvantages pointed out in inorganic solid electrolytes are related to volume changes. As the electrode/electrolyte interface in solid-state batteries is solid/solid, volume changes of the electrode must be considered in the cell design. Regarding the ionic conductivity, even though polymers are fundamentally more suitable for high ionic conductivity once they are structurally closer to the liquid state, much effort has been made to increase the ionic conductivity of inorganic Li-ion conducting electrolytes. Figure 3.4 shows the

dependence of ionic conductivity for several inorganic and polymeric solid electrolytes. As can be seen, the ionic conductivity of inorganic electrolytes (RT) overcomes polymeric system in most of the cases (see the grey line, Figure 3.4). Based on this potential for high ionic conductivity and due to high electrochemical and thermal stability, inorganic solid electrolytes have become a field of intense study [29,34,35,37], and it is also in the core scope of this study.

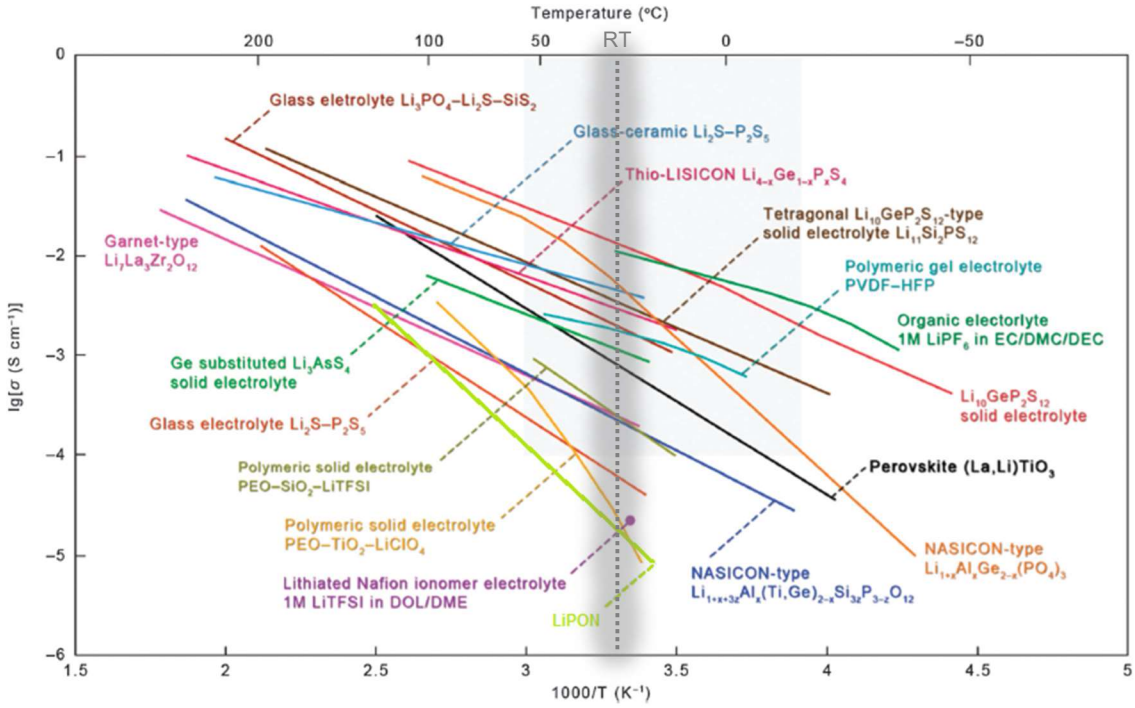

Figure 3.4 - The thermal evolution of ionic conductivity (σ) of inorganic and polymeric solid electrolytes. As a reference, the organic electrolyte adopted in Li-ion batteries is also included (adapted from [29]).

3.4 Inorganic Solid Electrolytes

As discussed before in section 2.2, ionic conduction in inorganic compounds occurs by random jumps of ions or defects, leading to position exchange with their neighbors. The creation and/or movement of these charged species requires energy, so the ionic conductivity of these compounds increases with increasing temperature following an Arrhenius-like relationship (Eq. 2.5). Thus, ceramic solid electrolytes are well suited for high-temperature applications. However, the ionic conduction in some compounds is reasonably high even at RT, so there are

several types of Li-ion conducting inorganic ceramics that have been investigated for possible use in Li-ion batteries. As shown in Figure 3.4, several inorganic ionic conductors from different classes, such as sulfides, nitrides, titanates, zirconates and phosphates among others, present ionic conductivity higher than 10^{-5} $S.cm^{-1}$ at RT [1,29,34–36]. Here, we choose to give an overview of the most known Li-ion conductors with high ionic conductivity, since the ionic conductivity is one of the most critical properties of electrolytes. Therefore, some important classes of electrolytes such as LISICON-type, antiperovskite-type and argyrodite-type compounds are suppressed here due to low ionic conductivity and/or to be still in the initial stage of research. A more detailed description of these systems can be found elsewhere [10].

Studies on ionic conduction in sulfides started in glasses. Due to the high polarizability of sulfide ions, the interaction between the anions and the lithium ions is weakened. Consequently, sulfides inherently tend to show fast ionic conduction as reported for glass systems such as Li_2S-SiS_2 and Li_2S-P_2S_5 (Figure 3.4). The addition of tiny amounts of lithium ortho-oxosalts Li_xMO_y (M = Si, Ge, P) to Li_2S-SiS_2 glasses is often employed to increase the conductivity. The ion conductivity in a glass is usually higher than that in their isochemical crystal due to the opener structure of the glass since glass usually has a larger available volume. Therefore, crystallization of glass typically decreases the total ionic conductivity of the sample. However, glass-ceramics of the Li_2S-P_2S_5 system show higher ionic conductivity than the precursor glass (Figure 3.4), which is attributable to the higher conductivity of the precipitated crystalline phase Thio-LISICON. Crystalline $Li_{4-x}Ge_{1-x}P_xS_4$ and $Li_{10}GeP_2S_{12}$ with Thio-LISICON-type structure (tetragonal, space group $P4_2/nmc$) also have a remarkable high ionic conductivity (Figure 3.4). Besides the high grain ionic conductivity, sulfides frequently show low grain-boundary resistance and often do not have transition metal elements in their composition that might narrow the electrochemical window. However, these electrolytes can quickly react with ambient moisture and generate H_2S gas. Also, the synthesis methods are not so trivial since the raw materials should be heated in a sealed container under controlled atmosphere because of the high vapor pressure of sulfur and to avoid oxidation [10,34–39].

Among the most promising Li-ion conducting oxides are the perovskite-type structured compounds with general formula ABO_3. The ideal perovskite-type structure (cubic, space group $Pm\bar{3}m$) consists of A-site ions (typically alkaline-earth or rare-earth elements) at the corners of a cube, B ions (typically transition metal ions) at the center, and oxygen atoms at the face-center positions. Lithium can be introduced in the perovskite on the A-site through aliovalent doping, creating compositions such as in lithium lanthanum titanate (LLT) with general formula $Li_{3x}La_{(2/3)-x}\square_{(1/3)-2x}TiO_3$ ($0<x<1/6$). Here, □ stands for A-site vacancy and in the extreme case where x is equal to 1/6 ($Li_{1/2}La_{1/2}TiO_3$), La/Li ratio is equal to 1 and no extrinsic vacancy defects are generated, since the electroneutrality is already established by the weighted average of oxidation states of Li and La. Increasing the La/Li ratio above 1 results in the formation of A-site vacancies to maintain charge neutrality until the other extreme where x is equal to 0 and the number of A-site vacancy reaches a maximum value of one for each 2 La atom. Several other systems with different A and B cations have been studied, but the maximum grain ionic conductivity (10^{-3} Scm^{-1} at RT) has been observed for LLT at x = 0.125 and La/Li = 1.4 (Figure 3.4). Despite of the very high grain ionic conductivity, several problems are encountered with LLT, like Li_2O losses observed due to high temperature and longtime sintering process for sample consolidation, and also because the total ionic conductivity of theses ceramics is much lower than that of single crystals due to blocking grain boundaries [10,29,34–37,40].

Some oxides forming a garnet-type structure (cubic, space group $Ia\bar{3}d$) have also good Li-ion conductivity. This new family of Li-ion conductors has general formula $A_3B_2(XO_4)_3$ such as $Ca_3Al_2(SiO_4)_3$ whose structure is constituted of XO_4 tetrahedra and BO_6 octahedra connected via edge sharing. Although this is the general formula, it has been reported an increasing of the number of lithium per formula unit to 5, such as in the $Li_5La_3B'_2O_{12}$ (B' = Bi, Sb, Nb, Ta) system. A further increase in the Li content per formula unit to 7 can be achieved in $Li_7La_3B''_2O_{12}$ (B'' = Zr, Hf, Sn) system. The highest ionic conductivity in garnet-type compounds has been reported for cubic $Li_7La_3Zr_2O_{12}$ (LLZ) in the order of 10^{-4} Scm^{-1} at R.T. (Fig 3.3.2). In the LLZ garnet-type structure, Li positions are

generally referred to as Li(1) if they are tetrahedrally coordinated to oxygen, and as Li(2) if they are octahedrally coordinated. LLZ can exhibit two crystal structures, cubic or tetragonal and the conductivity of the tetragonal phase is about two orders of magnitude lower than that of the cubic phase. LLZ undergoes a phase change from tetragonal to cubic structure as the sintering temperature increases, therefore the challenge has been to stabilize the cubic phase. Nevertheless, these electrolytes have been reported as stable in contact with lithium metal anode although some reports of instabilities against positive electrodes have also been shown [10,35,36,41,42].

Another electrolyte class of common interest is the LiPON-related compounds. In principle, LiPON compounds can be considered a Li-ion defective γ-Li_3PO_4 solid solution (orthorhombic, Pnma space group) with general composition $Li_xPO_yN_z$, (x = 2y+3z-5). Other variations of this system are LiPOS (with sulfur instead of nitrogen), LiSON (with sulfur instead of phosphorus), LiBSO (with sulfur and boron instead of phosphorus and nitrogen) and LiSiPON (with silicon). Usually, these electrolytes have a quite low Li-ion conductivity (~10^{-6} Scm^{-1} at RT) but are stable in contact with metallic lithium (Fig 3.4). Although the ionic conductivity remains moderate, the preparation by sputtering is a significant advantage since thin films can be easily obtained, which reduces the overall resistance of the electrolyte. In this case, the resulting electrolyte is often a glass instead of a crystalline phase, since very high cooling rates are inherent to sputtering methods. Another important advantage of these electrolytes is their excellent cyclability which can reach up to 10,000 cycles. While LiPON-based electrolytes show improvement over other electrolytes classes, mainly due to their compatibility with lithium, their overall ionic conductivities are still a limiting factor [10,35,41,42].

Finally, a prominent family of phosphates has also been extensively studied due to its high ionic conductivity. These phosphates crystallizes in a NASICON-type structure, and its general chemical formula can be described as $LiB_2(PO_4)_3$ where B is a tetravalent element (Ge, Ti, Sn, Zr, Hf, among others). The NASICON-type framework (rhombohedral, $R\bar{3}c$ space group) consists of isolated BO_6 octahedra interconnected via corner sharing with PO_4 tetrahedra in

alternating sequences, which form a very open structure with 3D interconnected channels. The Li sites sit in the interstitials between the BO_6 octahedra and PO_4 tetrahedra in two types of interstitial positions (M′ and M″). In order to add lithium to the chemical formula, attempts to replace tetravalent cation by a trivalent one have resulted in two systems with high ionic conductivity (~10^{-3} Scm^{-1} at RT), namely, $Li_{1.3}Al_{0.3}Ti_{1.7}(PO_4)_3$ (LATP) and $Li_{1.4}Al_{0.4}Ge_{1.6}(PO_4)_3$ (LAGP) (Figure 3.4). Because of the high ionic conductivity presented by this phase, hundreds of compositions have been investigated. In general, the NASICON-like phase is formed with different replacing elements and in a wide range of compositions. Additionally, NASICON-like conductors are typically stable in air and water and are stable at high potentials. The main drawbacks of these materials lies in the grain boundary resistance, which decrease the total ionic conductivity at least one order of magnitude, and the fact that titanium-containing compounds can be reduced at low potentials. [10,29,34–37,39–43]. Nevertheless, in face of the other features of NASICON-type compounds such as high ionic conductivity, structural versatility and chemical stability in water and atmospheric conditions, this present study is also centered in NASICON-like Li-ion conductors.

3.5 NASICON-like Solid Electrolytes

3.5.1 Structure

The term NASICON arises from Sodium (Na) Super (S) Ionic (I) Conductor (CON), and it was first given to the solid solution phase based on the system $Na_{1+x}Zr_2P_{3-x}Si_xO_{12}$, discovery by Hong and Goodenough in the 1970s. With general chemical formula $AB_2(XO_4)_3$, the NASICON-type crystal structure consists of a three-dimensional rigid framework with BO_6 octahedra sharing corners with XO_4 tetrahedra, where A is the guest mobile cation (e. g. Li, Na), B is typically a tetravalent cation (e. g. Ti, Ge, Sn, Hf, Zr), and X is a pentavalent cation (such e. g. P, V, As). The mobile cations are distributed between the BO_6 octahedra and XO_4 tetrahedra in two types of interstitial positions (M′ and M″). The $[B_2(XO_4)_3]$ chains may form a rhombohedral or an orthorhombic framework, although a monoclinic structure has also been reported [10,35–37,40–43]. Figure

3.5 shows representations in different directions of rhombohedral NASICON-type crystal structure as well as the two types of interstitial position.

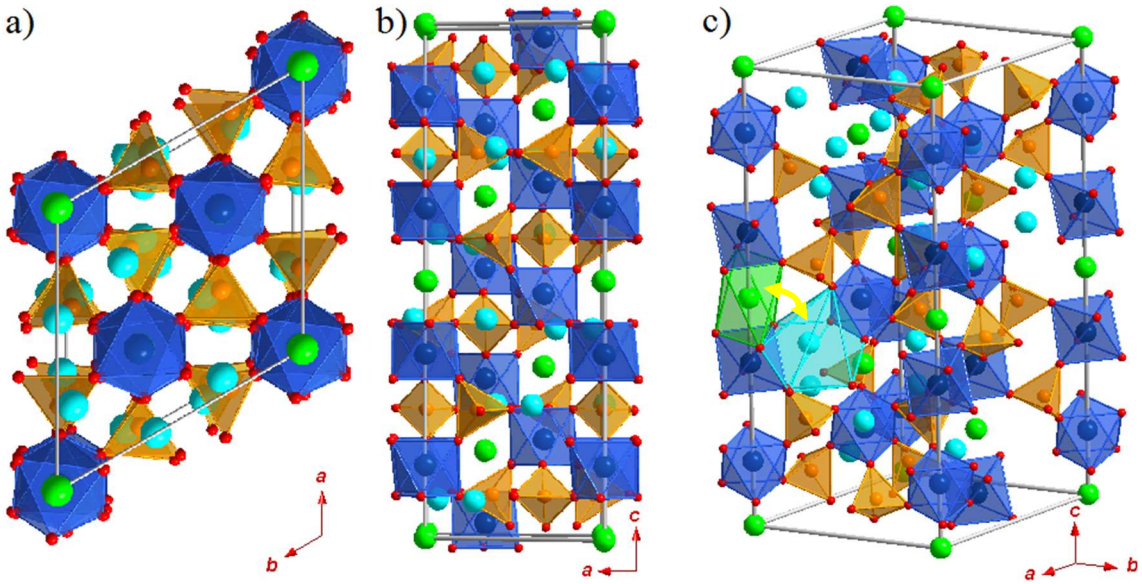

Figure 3.5 - Representation of NASICON-type crystal structure (rhombohedral) along with c direction (a) and b direction (b), and in a three-dimensional view (c). Blue, orange and red spheres represent B, X, and oxygen, respectively. XO_4 tetrahedra are presented in orange and BO_6 octahedra are presented in blue. A+ mobile cations are presented as spheres in light green and blue for M' and M" interstitial positions, respectively. One M' and M" coordination polyhedron is also shown in light green and blue as well as the hoping trajectory between these two sites which is presented as a yellow arrow.

The rhombohedral phase provides better conduction pathways for a guest A^+ cation, but stabilizing the rhombohedral phase is more difficult with a Li^+ guest ion than with a Na^+ guest. Moreover, the interstitial space of the rhombohedral framework contains one M' to three M" sites. The M' sites are coordinated by six oxygen located directly between two BO_6 octahedra. The M" sites are coordinated by eight oxygen and located between two columns of BO_6 octahedra (see light blue and green polyhedra, Figure 3.5c). The mobile cation migration occurs via hopping between these two sites through bottlenecks (see yellow arrow, Figure 3.5c), whose size depends on the nature of the skeleton ions. Partial occupancies of A^+ on those two sites are crucial for fast ion conduction, especially because

vacancies are required at the intersection of the conduction pathways to give access to three-dimensional diffusion within the structure [10,29,35,37]. From a crystallography point of view, the size of the bottleneck is intimately linked with the volume of the unit cell. Several studies have demonstrated a dependence of ionic conductivity with the volume of the unit cell. In case of the rhombohedral lattice (trigonal system), the lattice parameters of NASICON-type structure can also be represented on hexagonal axes and be easily determined by simply knowing the 2 theta position of two diffraction planes. Thus, the lattice parameters and the volume of NASICON unit cell can be estimated based on Eq. 3.1 and Eq. 3.2, respectively [44].

$$\frac{1}{d^2} = \frac{4}{3}\left(\frac{h^2+hk+k^2}{a^2}\right) + \frac{l^2}{c^2} \quad \text{(Eq. 3.1)}$$

$$V = \frac{\sqrt{3}a^2c}{2} \quad \text{(Eq. 3.2)}$$

3.5.2 Chemical composition

Due to the structural features listed above, electrical properties of NASICON-type compounds are strongly dependent on the framework composition. As mentioned before, in case of phosphates Li-ion conductors, the general chemical formula of these compounds can be simplified as $LiB_2(PO_4)_3$. As the lattice parameters *a* and *c* and the unit cell volume are dependent on the ionic radius of the B cation, this will determine, for example, the size of the bottleneck and somehow the activation energy for Li-ion conduction through the crystalline network. Thus, the bottleneck size can be adjusted according to the B cation located in the octahedral site influencing the Li-ion migration [10,35–37]. Several studies available in the literature show that the presence of Ti^{+4} results in lower activation energy and consequently higher ionic conductivity in comparison to Ge^{+4}, Zr^{+4} e Hf^{+4} cations. Whereas the ionic radius of these cations in octahedral coordination in oxides increases in the following order $Ge^{+4} < Ti^{+4} < Sn^{+4} < Hf^{+4} < Zr^{+4}$, there seems to be an optimum size of unit cell volume and bottleneck for lithium as a mobile guest that culminate in lower activation energy

for Li-ion conduction. In case of Na-ion conductors, the B cation which gives lowest activation energy has been confirmed to be Zr^{+4} [36,37,41,43].

Additionally, the oxidation state of the B cation has influence in the stoichiometric amount of lithium in the chemical formula and hence in the Li^{+} charge carrier concentration. Based on this idea, the so-called strategy of aliovalent substitution has been employed. Therein, the substitution of a tetravalent B^{+4} cation for a trivalent B^{+3}, according to the chemical formula Li_{1+x} $B"_x$ B'_{2-x} $(PO_4)_3$, must be followed by lithium addition to maintain the compound electroneutrality. In the unsubstituted general compounds (x=0), sites M' are fully occupied while M" sites are empty and an increase of x increases the occupancy on M" sites [10,40]. This approach has been widely employed on several systems with different B cations (Ge^{+4}, Ti^{+4}, Sn^{+4}, Zr^{+4}) but even more with Ti^{+4}. The most used trivalent cations are Al^{+3}, Cr^{+3}, Ga^{+3}, Fe^{+3}, Sc^{+3}, In^{+3}, Lu^{+3}, Y^{+3} and La^{+3}. The result of this tireless search has resulted in an increment of ionic conductivity of about 1000 times comparatively to simple NASICON-type compounds ($LiB_2(PO_4)_3$). As an example, one can cite the $Li_{1.4}Al_{0.4}Ge_{1.6}(PO_4)_3$ (LAGP) and $Li_{1.3}Al_{0.3}Ti_{1.7}(PO_4)_3$ (LATP) systems and their precursor $LiGe_2(PO_4)_3$ (LGP) and $LiTi_2(PO_4)_3$ (LTP) compounds.

However, in the cases mentioned above, these large increments in ionic conductivity cannot be explained merely by the increase of Li^{+} concentration, since the amount of Li^{+} charge carrier added rarely exceeds the mark of 50%. In the same way, since Al^{+3} (0.0675 nm) has smaller crystal radius than Ti^{+4} (0.0745 nm) and comparable to Ge^{+4} (0.0670 nm), the increase in ionic conductivity cannot be explained solely by cell volume considerations. On the other hand, this effect can be rationalized using the Gibbs free energy of formation of Al_2O_3 (-1582 KJ/mol), TiO_2 (-889 KJ/mol) and GeO_2 (-521 KJ/mol). Accordingly, the substitution of the less stable parent Ti^{+4} or Ge^{+4} by the more stable Al^{+3} is expected to increase the B–O bond strength and to decrease the Li–O bond strength, which increases the lithium ion mobility in LAGP and LATP systems [41,42]. Recently, a study has used ab-initio molecular dynamics simulations to investigate differences between LGP and LAGP systems regarding their structure and Li-ion diffusivity mechanisms. It concludes that the increase in ionic

conductivity in LAGP is not originated just from increased Li concentration, but by newly created diffusion paths with substantially reduced activation energies compared with LGP [45].

3.5.3 Microstructure

Despite the outstanding achievements related to the grain ionic conductivity of NASICON-type compounds, the resulting electrolyte is a polycrystalline material. Therefore, a critical factor which still limits their use as solid electrolytes is the detrimental effects of grain boundaries in the total conductivity. The total conductivity of polycrystalline materials does not depend only on lithium ion transport in the crystalline grains, but also through the grain boundaries. If the serial grain boundary resistance is much higher than the grain resistance, it practically determines the overall resistance of the material in an electrochemical cell. Unfortunately, this is usually the case since grain boundaries act as scattering barriers for ion transport and the grain boundary ionic conductivity is typically one to three orders of magnitude lower than the grain ionic conductivity. Therefore, controlling the microstructure and the ion transport properties of the grain boundaries is a crucial factor for obtaining optimized NASICON-like solid electrolytes with appreciable ionic conductivity at RT [39,46–48].

Another determinant issue to achieve high total ionic conductivity is the relative density of the electrolyte. The deleterious effect of pores is rather evident once a porous can be considered as part of the electrolyte which does not have the desired properties of the concerned ionic conductive material. However, the detrimental presence of pores goes beyond the lack of property matter, since they behave as scattering obstacles for ion motion through the electrolyte. Consequently, besides the total porosity, the porous-size distribution and the distribution of pores along the electrolyte are determinant features [21,24]. Some studies which investigate the effect of aliovalent substitution in the total ionic conductivity have suggested that increment in the total ionic conductivity was also due to the decrease in the porosity and not just due to structural changes and increment of charge carrier concentration [49,50]. Therefore, the chosen

processing route to obtain NASICON-like solid electrolytes is also of great importance.

3.5.4 Synthesis methods

Conventionally, the most employed synthesis route to obtain NASICON-like solid electrolytes is the traditional solid-state reaction followed by solid-state sintering. The simplicity and versatility of this route have allowed the development and study of NASICON-like solid electrolytes of several compositions [49,50]. Other alternative routes including sol-gel [51], Pechini [52] and mechanochemical [53] synthesis have been used to overcome general drawbacks of solid-state reaction route such as elevated temperatures and longtime of synthesis. However, any synthesis route that requires sintering to consolidate the electrolyte has evident limitations related to microstructural control and to the achievement of fully dense electrolytes.

In this respect, the glass-ceramic route offers clear advantages, since it allows one to obtain electrolytes of high relative density and to design its microstructure by controlling glass crystallization. Unlike sintered ceramics, glass-ceramics are inherently free from porosity. However, in some cases, bubbles or pores develop during the latter stages of crystallization. The glass-ceramic route consists in obtaining a liquid by melting oxides, carbonates, or any other components, and cooling it down fast enough to prevent crystallization. In a subsequent process, the resulting glass is heat-treated to crystallize the desired phase. In the cases where the parent glass presents homogenous nucleation, the electrolyte microstructure can be designed by controlling the nucleation and crystal growth phenomena by properly choosing the holding time and temperature of heat treatment [54]. On the other hand, the main drawback of the glass-ceramic route is the fact that not all NASICON-like compositions can form a glass at the typical cooling rates used in the laboratory or industrial scale. In fact, only a few oxides (B_2O_3, SiO_2, P_2O_5, GeO_2) are known to form glasses easily, and they must be present in a molar ratio of about 50% [55]. Therefore, even though limited, the glass-ceramic route has exciting potential and has become one of the most used routes to synthetize NASICON-like electrolytes. In

especial, because these NASICON-like phosphates usually present homogeneous nucleation which allows controlling the final microstructure [56,57]. On the base of these ideas, the glass-ceramic route will be the synthesis route used to develop the electrolytes under study in this work.

4 EXPERIMENTAL PROCEDURE

4.1 Glass Synthesis

In the present work, all synthesized glasses were obtained by means of the conventional melt quenching method. In summary, the method comprises heating up a reactant mixture until it reaches the liquid state at low viscosity. The liquid is held for some time above *liquidus* temperature to homogenize the resulting melt. Finally, the low-viscosity liquid is poured and quenched to avoid premature crystallization.

4.1.1 Glass synthesis of $Li_{1.4}Cr_{0.4}(Ge_{0.4}Ti_{0.6})_{1.6}(PO_4)_3$ composition

The proposal of the $Li_{1+x}Cr_x(Ge_yTi_{1-y})_{2-x}(PO_4)_3$ (LCGTP) system is based on the rationale that the introduction of GeO_2 increases the glass forming ability of the precursor glass, whereas the presence of TiO_2 and Cr_2O_3 might help to keep the NASICON cell parameters close to those of LTP system. Once, to the best of our knowledge, the LCGTP system is proposed for the first time here, one should seek more information about the glass forming ability and crystallization behavior (surface or volume) of this system, as well as if the precipitation of NASICON-like phase from the precursor glass is suitable. Therefore, we firstly synthesized a particular composition (x=y=0.4) of the proposed LCGTP system by the glass-ceramic route to investigate its overall behavior regard to the properties above. The precursor glass was obtained by melting a mixture of reagents with a $17.5Li_2O{\cdot}5Cr_2O_3{\cdot}16GeO_2{\cdot}24TiO_2{\cdot}37.5P_2O_5$ oxide molar ratio, corresponding to the stoichiometric chemical formula $Li_{1.4}Cr_{0.4}(Ge_{0.4}Ti_{0.6})_{1.6}(PO_4)_3$. Suitable amounts of Li_2CO_3 (99.0%, Synth, Brazil), Cr_2O_3 (99.0%, Aldrich, USA), GeO_2 (99.99%, Alfa Aesar, USA), TiO_2 (99.9%, Aldrich, USA) and $NH_4H_2PO_4$ (98%, Aldrich, USA) were used as raw materials. These reactants were homogenized in a roll ball mill for 12 h, using zirconia balls, and the resulting mixture was calcined in a platinum crucible on a hot plate in order to decompose $NH_4H_2PO_4$ and prevent chemical attack of the platinum crucible at higher temperatures. The resulting powder was melted at 1450 °C for 120 min, and the low viscosity liquid was splat-cooled in a brass die to prevent crystallization. The quenched glass was annealed at 550 °C for 2 h to relieve thermal stresses. After cooling, the

resulting glass was bubble-free, transparent, with an intense green color (see Figure 5.5) probably caused by its chromium content.

4.1.2 Glass synthesis of LCGTP compositions

In order to cover the entire LCGTP system, compositions were tailored with x and y ranging from 0.2 to 0.8 with 0.2 steps, which resulted in 16 compositions. LCGTP samples were labeled according to their x and y values. Table 4.1 presents all investigated LCGTP compositions as well as their respective oxide molar ratios. LCGTP precursor glasses were obtained (~15g by batch) following the methodology employed in in the previous section, except that in this case all compositions had 5% increment of $NH_4H_2PO_4$ and the holding time of the melting step was only 30 min. These modifications were made to compensate and avoid P_2O_5 evaporation during the melting procedure, respectively. After cooling, the glasses presented a greenish-dark color, which becomes more intense and darker for higher chromium and titanium content, respectively.

Table 4.1 - Nominal glasses compositions and their respective oxide molar ratios (%) based on systematic substitution of x and y on the $Li_{1+x}Cr_x(Ge_yTi_{1-y})_{2-x}(PO_4)_3$ (LCGTP) system.

Samples	x	y	Li (1+x)	Cr (x)	Ge (2-x)y	Ti (2-x)(1-y)	P 3	Li_2O (%)	Cr_2O_3 (%)	GeO_2 (%)	TiO_2 (%)	P_2O_5 (%)
LCGTP0202	0.2	0.2	1.2	0.2	0.36	1.44	3	15.0	2.5	9.0	36.0	37.5
LCGTP0204	0.2	0.4	1.2	0.2	0.72	1.08	3	15.0	2.5	18.0	27.0	37.5
LCGTP0206	0.2	0.6	1.2	0.2	1.08	0.72	3	15.0	2.5	27.0	18.0	37.5
LCGTP0208	0.2	0.8	1.2	0.2	1.44	0.36	3	15.0	2.5	36.0	9.0	37.5
LCGTP0402	0.4	0.2	1.4	0.4	0.32	1.28	3	17.5	5.0	8.0	32.0	37.5
LCGTP0404	0.4	0.4	1.4	0.4	0.64	0.96	3	17.5	5.0	16.0	24.0	37.5
LCGTP0406	0.4	0.6	1.4	0.4	0.96	0.64	3	17.5	5.0	24.0	16.0	37.5
LCGTP0408	0.4	0.8	1.4	0.4	1.28	0.32	3	17.5	5.0	32.0	8.0	37.5
LCGTP0602	0.6	0.2	1.6	0.6	0.28	1.12	3	20.0	7.5	7.0	28.0	37.5
LCGTP0604	0.6	0.4	1.6	0.6	0.56	0.84	3	20.0	7.5	14.0	21.0	37.5
LCGTP0606	0.6	0.6	1.6	0.6	0.84	0.56	3	20.0	7.5	21.0	14.0	37.5
LCGTP0608	0.6	0.8	1.6	0.6	1.12	0.28	3	20.0	7.5	28.0	7.0	37.5
LCGTP0802	0.8	0.2	1.8	0.8	0.24	0.96	3	22.5	10.0	6.0	24.0	37.5
LCGTP0804	0.8	0.4	1.8	0.8	0.48	0.72	3	22.5	10.0	12.0	18.0	37.5
LCGTP0806	0.8	0.6	1.8	0.8	0.72	0.48	3	22.5	10.0	18.0	12.0	37.5
LCGTP0808	0.8	0.8	1.8	0.8	0.96	0.24	3	22.5	10.0	24.0	6.0	37.5

4.2 Glass-ceramic Synthesis

In the present work, all synthesized glass-ceramics were crystallized using simple heat treatment, which consists of just one dwell temperature and one dwell holding time. Thus, the glass samples were put in a pre-heated furnace at the dwell temperature. After the end of dwell holding time, the glass-ceramics were taken from the furnace and let cooling down at room temperature (RT).

4.2.1 Glass-ceramic synthesis of $Li_{1.4}Cr_{0.4}(Ge_{0.4}Ti_{0.6})_{1.6}(PO_4)_3$ composition

In order to study the influence of the heat treatment temperature on the electrical properties of the LCGTP glass ceramic, we crystallized the $Li_{1.4}Cr_{0.4}(Ge_{0.4}Ti_{0.6})_{1.6}(PO_4)_3$ glass at different temperatures. Glass samples were heat-treated for 12h in the form of bulk samples at the crystallization peak temperature (T_p) obtained from DSC measurements, ~700 °C, and also at higher temperatures of 800 °C, 900 °C and 1000 °C, giving rise to samples named HT700, HT800, HT900, HT1000. To investigate the crystallization behavior of the proposed glass composition, additional heat treatments of 5 min at T_p were also performed in bulk and powder glass samples.

4.2.2 Glass-ceramic synthesis of LCGTP compositions

All LCGTP glasses were heat treated as bulk samples at 900°C for 2 hours to obtain fully crystallized glass-ceramics. The heat treatment temperature was defined based on results obtained from a previous investigation on the influence of the heat treatment temperature on electrical properties. The holding time of 2 hours was determined based on crystallization peak width, which is few degrees wide indicating that the overall crystallization takes place within minutes. Therefore, the time of 2 hours was chosen to ensure that the obtained glass-ceramics are fully crystallized or at least have minimized residual vitreous phase.

4.3 Characterization of $Li_{1.4}Cr_{0.4}(Ge_{0.4}Ti_{0.6})_{1.6}(PO_4)_3$ Glass and Glass-ceramics

In this step, $Li_{1.4}Cr_{0.4}(Ge_{0.4}Ti_{0.6})_{1.6}(PO_4)_3$ glass composition was characterized using differential scanning calorimetry (DSC), optical dilatometry

(OD), X-rays diffraction (XRD), Fourier transform infrared spectroscopy (FT-IR) and electrochemical impedance spectroscopy (EIS). The glass-ceramics deriving from the $Li_{1.4}Cr_{0.4}(Ge_{0.4}Ti_{0.6})_{1.6}(PO_4)_3$ glass were also characterized by XRD, FT-IR and EIS. Moreover, scanning electron microscopy (SEM) and energy dispersive X-ray spectroscopy (EDX) were used in the microstructural characterization of these glass-ceramics.

4.3.1 Differential scanning calorimetry of $Li_{1.4}Cr_{0.4}(Ge_{0.4}Ti_{0.6})_{1.6}(PO_4)_3$ composition

DSC analyses of glass samples were performed in the range of 300 to 1273 K at a heating rate of 10 $K.min^{-1}$, using a Netzsch DSC 404 differential scanning calorimeter equipped with platinum pans and covers. Powder and bulk samples were subjected to the same DSC procedure to evaluate their crystallization behavior (surface or volume crystallization). To obtain powder samples with two different average particle sizes, small pieces of the glass were manually ground in an agate mortar until the powder passed through a 150 or 40 μm mesh sieve; these samples were labelled P150-Glass and P40-Glass, respectively. The characteristic temperatures of the precursor glass, such as glass transition temperature (T_g), crystallization onset temperature (T_x) and crystallization peak temperature (T_p) were determined from the DSC curves.

4.3.2 Optical dilatometry of $Li_{1.4}Cr_{0.4}(Ge_{0.4}Ti_{0.6})_{1.6}(PO_4)_3$ composition

The melting temperature of the glass-ceramics could not be determined by DSC measurements because of a temperature limit of the calorimeter. Then, glass crystallization was monitored by optical dilatometry (OD) using a Misura M3D1600 dilatometer. To perform this experiment, a bulk glass sample was prepared in a parallelepipedal shape. The sample was heated from 300 to 1673 K, also applying a heating rate of 10 $K.min^{-1}$. In this range of temperature, it was also possible to determine the liquidus temperature (T_l) of the resulting glass-ceramic.

4.3.3 X-rays diffraction of $Li_{1.4}Cr_{0.4}(Ge_{0.4}Ti_{0.6})_{1.6}(PO_4)_3$ composition

To confirm the glassy nature of $Li_{1.4}Cr_{0.4}(Ge_{0.4}Ti_{0.6})_{1.6}(PO_4)_3$ precursor glass, X-ray diffraction (XRD) analysis of a bulk glass sample was performed in a Rigaku Ultima IV diffractometer equipped with Cu Kα radiation. It was employed a continuous scan speed of 0.02°/s in the 2 theta range of 5 to 90°. Powder glass samples were also submitted to XRD analyses under the same conditions to provide supplemental information about the crystallization behavior. The same conditions of XRD analysis were employed to characterize the glass-ceramic samples heat-treated for 12 h. Likewise, XRD analyses of glass-ceramic samples heat treated for 5 min, based on the DSC analyses, were also performed in bulk and powder samples to examine the crystalline phases formed during the crystallization step.

4.3.4 Fourier transform infrared spectroscopy of $Li_{1.4}Cr_{0.4}(Ge_{0.4}Ti_{0.6})_{1.6}(PO_4)_3$ composition

A structural analysis of powder and bulk samples of $Li_{1.4}Cr_{0.4}(Ge_{0.4}Ti_{0.6})_{1.6}(PO_4)_3$ glass was performed by Fourier transform infrared spectroscopy (FT-IR). All the infrared spectra were recorded at RT in a Perkin Elmer Spectrum-GX spectrometer operating in reflectance mode, in the wavenumber range of 4000 - 400 cm^{-1}, applying 30 scans and a resolution of 1 cm^{-1}. Moreover, bulk and powder glass-ceramic samples heat-treated for 5 min were also analyzed by FTIR in the same conditions.

4.3.5 Scanning electron microscopy of $Li_{1.4}Cr_{0.4}(Ge_{0.4}Ti_{0.6})_{1.6}(PO_4)_3$ composition

Fracture surfaces of bulk glass-ceramic samples heat-treated for 12 h were prepared for SEM analyses by breaking the samples and sputtering gold on the freshly fractured surfaces. SEM micrographs were recorded with a FEI Inspect S50 scanning electron microscope, and chemical analyses of these samples by energy dispersive X-ray spectroscopy (EDX) were performed in the same device.

4.3.6 Electrochemical impedance spectroscopy of $Li_{1.4}Cr_{0.4}(Ge_{0.4}Ti_{0.6})_{1.6}(PO_4)_3$ composition

The electrical conductivity of $Li_{1.4}Cr_{0.4}(Ge_{0.4}Ti_{0.6})_{1.6}(PO_4)_3$ glass and glass-ceramics heat-treated for 12h in different temperatures was estimated by electrochemical impedance spectroscopy (EIS) using a Novocontrol Alpha impedance analyzer. A rigorous routine comprising calibration, shortcut (closed electrodes) and standard resistor (100Ω) measurements was established before measuring each sample to ensure a near zero impedance contribution from the equipment. EIS measurements were performed in glass and glass-ceramic bulk samples with parallel and polished faces, with gold electrodes sputtered on both sides to ensure electrical contact. Samples were about 0.1 cm thick and had an electrode contact area around 0.1 cm^2. The measurements were performed in the frequency range of 10^7 - 1 Hz, applying a root mean square (RMS) AC voltage of 500 mV in a temperature range of 300 - 400 K. The temperature was controlled using a Novotherm temperature control system, with a maximum temperature variation of ±0.1 K during the EIS measurements. The results were fitted using ZView 3.2b software, using an appropriate equivalent circuit.

4.4 Characterization of LCGTP Glasses and Glass-ceramics

In this step, all different compositions of LCGTP glasses, whose synthesis is presented in section 4.1.2, were characterized. Here, we used inductively coupled plasma mass spectrometry (ICP–MS) for chemical characterization and DSC, OD, XRD. The structural and electrical characterization of glass-ceramics of all LCGTP composition whose synthesis is presented in section 4.2.2, was performed using XRD and EIS techniques, respectively.

4.4.1 Inductively coupled plasma mass spectrometry of LCGTP compositions

The concentration of chemical elements in the glasses was examined by inductively coupled plasma mass spectrometry (ICP–MS), using an Agilent 7900 ICP-MS equipped with an ASX-500 autosampler. Aqueous solutions for ICP–MS analysis were prepared by digesting 10mg of powder glass samples in 5 ml of

40% hydrofluoric acid (HF). After 7 days the resulting solutions were dissolved in one liter of distilled water to reach the optimum limit of detection of the ICP-MS equipment for Li, Cr, Ge, Ti and P.

4.4.2 Differential scanning calorimetry of LCGTP compositions

Bulk glass samples of about 30mg were subjected to differential scanning calorimetry (DSC) analyses in a Netzsch DSC 404 calorimeter equipped with platinum pans and covers, applying a heating rate of 10 $K.min^{-1}$. The characteristic temperatures of the precursor glasses, such as the glass transition temperature (T_g) and crystallization peak temperature (T_p) were taken from DSC curves by using the derivative method.

4.4.3 Optical dilatometry of LCGTP compositions

The melting temperatures of all LCGTP glass-ceramics were obtained by means of optical dilatometry (OD). Parallelepipedal samples of LCGTP glasses with dimensions of approximately 5x5x1mm were prepared to perform this experiment. The glass crystallization and subsequent melting were monitored from 300 to 1673 K applying a heating rate of 10 $K.min^{-1}$ by using a Misura M3D1600 dilatometer.

4.4.4 X-rays diffraction of LCGTP compositions

All the glass-ceramics heat-treated at 900°C for 2 hours were subjected to X-ray diffraction (XRD) analysis as powder samples in a Rigaku Ultima IV diffractometer with Cu Kα radiation. To this end, XRD patterns were recorded in step scan mode, applying a 0.02º step size and 3 seconds per step in the 2 theta range of 10 to 110º.

4.4.5 Electrochemical impedance spectroscopy of LCGTP compositions

The electrical conductivity of all LCGTP glass-ceramics was also determined by means of EIS using a Novocontrol-Alpha impedance analyzer. The experiments and sample preparation were conducted under the same conditions described in section 4.3.6. Samples were about 0.1cm thick and had

a contact area of 0.1 to 0.2 cm^2. The spectra were fitted using an impedance spectroscopy software program (ZView 3.5b) and a suitable equivalent circuit.

4.5 Electrochemical Characterization of LCGTP Glass-ceramics

At this stage, the electrochemical stability window of LCGTP electrolytes is evaluated by voltammetry analyses, electrochemical impedance spectroscopy and X-ray photoelectron spectroscopy. LCGTP0402, LCGTP0602, LCGTP0604 and LCGTP0606 glass-ceramic compositions were chosen specially for their high ionic conductivity at RT (>10^{-4} Ω^{-1} cm^{-1}). For comparison, a LAGP ($Li_{1.5}Al_{0.5}Ge_{1.5}(PO_4)_3$) glass-ceramic synthesized as described in [58] is also investigated.

4.5.1 X-ray photoelectron spectroscopy

The oxidation state of Cr, Ge, Ti, P and O in LCGTP glass-ceramics was investigated by X-ray photoelectron spectroscopy (XPS) before and after the voltammetry analysis. The XPS analyses were carried out on a Thermo Electron ESCALAB 250 spectrometer with an Al Kα monochromatic source operating at 1486.6 eV. Survey and high-resolution spectra were obtained from an analyzed surface of 400µm diameter. The analyzer was operated at a chamber pressure in the range of 10^{-8} mbar and a constant pass energy of 150 eV and 20 eV, respectively, for survey and detailed spectra. The photoelectron spectra were calibrated based on the binding energy (BE) of C 1s core electrons of the C-C component resulting from adventitious carbon. Charge neutralization was also monitored based on the BE of C 1s signal.

4.5.2 Two-electrode setup electrochemical impedance spectroscopy

In most recent reports on investigations into the electrochemical stability of solid electrolytes, the latter is often characterized by cyclic voltammetry using gold, silver, platinum or stainless steel as a working electrode and Li metal as a counter and/or a reference electrode [58–64]. However, this procedure is unreliable if the electrolyte is unstable when in contact with lithium [65]. Therefore, EIS measurements were taken first, using a two-electrode setup with a symmetric

cell (Li/sample/Li) to evaluate the stability of the electrolytes against Li metal. The cell was assembled by pressing lithium foils mechanically against the sample, using stainless steel electrodes supported by a polytetrafluoroethylene (PTFE) structure with attachments that press one electrode against the other. A ModuLab XM ECS chassis equipped with a frequency analyzer slot was employed for the EIS measurements. These measurements were taken over time using AC signals with a RMS amplitude of 100mV in a frequency range of 1 MHz to 100 mHz. Since metallic Li was used, both the cell assembly and the measurements were performed in a glovebox filled with Argon (Ar).

4.5.3 Three-electrode setup cyclic voltammetry

The electrochemical stability of the LCGTP glass-ceramics was studied by cyclic voltammetry (CV) using a three-electrode setup, namely, counter, reference and working electrodes. Figure 4.1 shows a schematic representation of the measurement cell (a), and top (b) and cross-section (c) views of the positions of electrodes on the sample. Gold (Au) was sputtered on both sides of the samples (Figure 4.1b), after which the central part of the electrode was scraped at one side of the sample in order to insert the reference electrode Ag_3SI/Ag (Figure 4.1c). Parts 1 and 2 (Figure 4.1a) were sputtered with Au to ensure good electrical contact with the sample. A mixture of Ag_3SI powder and Ag (Sigma Aldrich, 99.9% of purity), prepared as described in [66], was pressed into the funnel chamber (part 4, Figure 4.1a), which was screwed onto the aluminum cylinder (part 3, Figure 4.1a). The entire system was placed inside a sealed container on Pyrex glass, enabling the atmosphere to be controlled. A ModuLab XM ECS chassis equipped with potentiostat slot was employed for the CV measurements. These measurements were taken in different atmospheres, i.e, air and vacuum ($2x10^{-3}$ mbar), at scan rates of 100, 10 and 1 mV·s−1 between -3 V and 5 V or -1.5 V and 1.5 V vs. Ag_3SI/Ag reference electrode. All the CV measurements were taken at RT (~295K), starting from the open circuit potential with anodic sweep and always with fresh samples since the experimental history of the sample would probably interfere with the results.

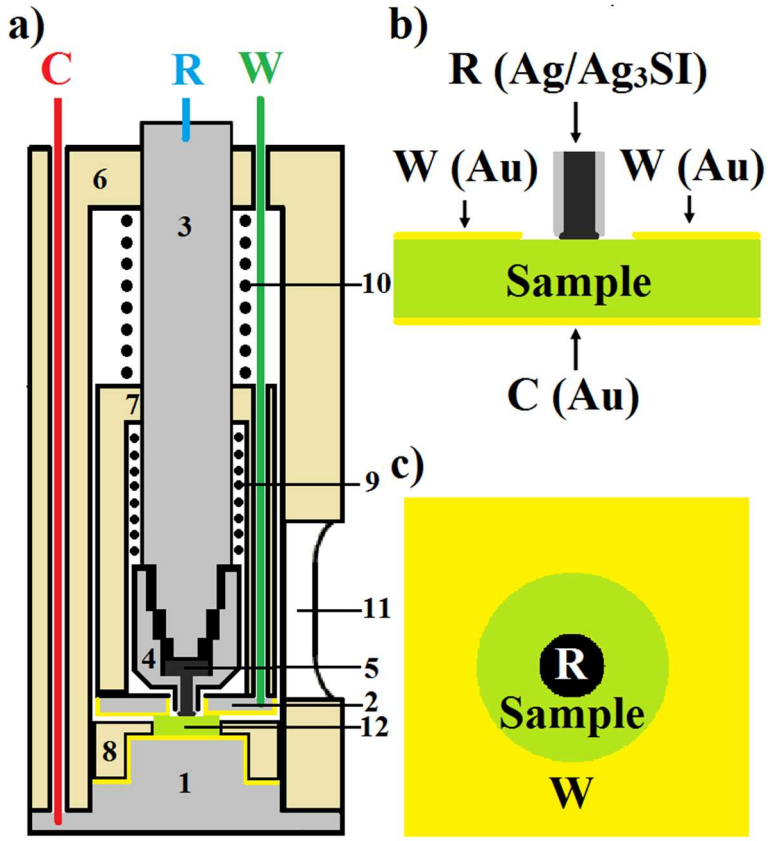

Figure 4.1 - Schematic representation of the measurement cell and electrode position on the samples: (a) three-electrode set-up cell, namely, counter (C), reference (R) and working (W) electrodes; (b) cross-section of the sample; (c) top view of the sample. Parts assigned numbers from 1 to 4 are made of aluminum and correspond to the electrical contact of the counter (1) and the working (2) electrodes, cylinder (3) and container (4) for the reference electrode powder (5). Parts from 6 to 8 are hollow cylinders made in polytetrafluoroethylene (PTFE) that have mechanical functions (6 and 7) or prevent short circuits (8) between the aluminum parts. Springs (9 and 10) serve to press the electrodes against the sample to ensure contact. The sample (12) is introduced at the entrance (11).

4.5.4 Three-electrode setup electrochemical impedance spectroscopy

In situ EIS analyses were performed in the three-electrode setup cell before and after cyclic voltammetry tests, i.e., without removing the sample from the cell. A ModuLab XM ECS chassis equipped with a frequency analyzer slot is employed. EIS measurements were taken using an AC signal with a RMS amplitude of 100mV vs. Ag_3SI/Ag in a frequency range of 1 MHz to 100 mHz.

4.5.5 Linnear sweep voltammetry

Additionally, linear sweep voltammetry (LSV) was used to prepare samples for XPS analyses to separate effects from the anodic and cathodic sweeps. Two samples were prepared using the three-electrode setup cell, in a single sweep using a scan rate of 1 $mV \cdot s^{-1}$ under vacuum. The anodic sweep was performed up to 5 V vs. Ag_3SI/Ag, while the cathodic sweep was scan up to -1.5 V vs. Ag_3SI/Ag. After LSV analyses Au electrode was removed using cotton and acetone and the prepared samples were maintained in a glove box filled with Argon (Ar) to keep the final state achieved through the LSV experiment. XPS analyses of these two samples are conducted using the same conditions as those used in the fresh LCGTP samples.

5 RESULTS AND DISCUSSION

5.1 Glass and Glass-ceramics of $Li_{1.4}Cr_{0.4}(Ge_{0.4}Ti_{0.6})_{1.6}(PO_4)_3$ Composition

5.1.1 Crystallization behavior

To evaluate the general crystallization behavior of glasses from LCGTP system, powder and bulk samples of $Li_{1.4}Cr_{0.4}(Ge_{0.4}Ti_{0.6})_{1.6}(PO_4)_3$ glass composition were subjected to DSC procedure described in section 4.3.1. Figure 5.1 shows DSC analyses of bulk (Bulk-Glass), coarse powder (P150-Glass) and fine powder (P40-Glass) samples of this glass composition. The DSC analysis of bulk glass revealed a very intense and narrow crystallization peak with a sharp crystallization peak (T_p) and a glass transition (T_g) temperature. On the other hand, the DSC curves of the powder samples did not show a clear T_g, while the finest powder (P40-Glass) showed two crystallization peaks at 711 °C and 741 °C (inset, Figure 5.1). Furthermore, the T_p of the glass powder samples unexpectedly shifted to a higher temperature when compared to the T_p of the bulk sample.

In principle, T_p should not change in bulk and powder samples when the glass shows volumetric crystallization. Conversely, if the glass shows surface crystallization, an increase in surface area, like in powder samples, should shift T_p to lower temperatures and the crystallization peak should be even narrower than that of the bulk glass sample. As can be seen in Figure 5.1, the opposite behavior occurred, with T_p shifting to higher temperatures and becoming broader as the glass powder became finer. Therefore, since T_p of the powder samples does not shift to lower temperatures, these results offer a primary evidence that $Li_{1.4}Cr_{0.4}(Ge_{0.4}Ti_{0.6})_{1.6}(PO_4)_3$ glass presents volume crystallization. These results also suggest that in this glass system, a high surface area, in fact, hinders crystallization.

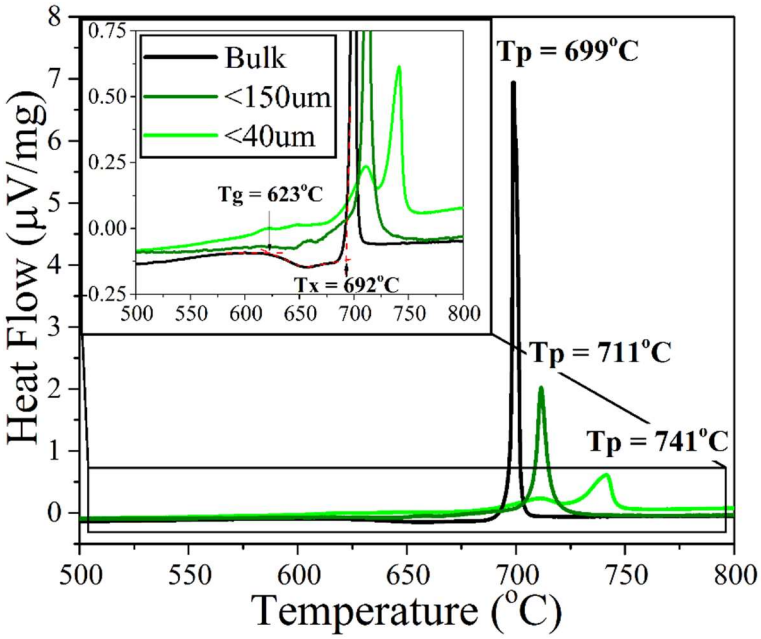

Figure 5.1 - DSC curves at a heating rate of 10 K min^{-1} of $Li_{1.4}Cr_{0.4}(Ge_{0.4}Ti_{0.6})_{1.6}(PO_4)_3$ glass composition in bulk form (Bulk-Glass), coarse (P150-Glass) and fine (P40-Glass) powder. The crystallization peak temperatures, T_p, are indicated for all samples, while T_x and T_g are indicated only for the bulk glass sample.

The melting temperature (T_m) of the crystallized phase was determined from an optical dilatometry (OD) analysis. Figure 5.2 shows the dependence of shrinkage as a function of temperature for the projected area of a parallelepipedal glass sample. Note that two particular events can be observed here. The first event at 695 °C (inflection point) is a slight shrinkage of about 1% (Figure 5.2, insert) in the same temperature range of T_p (699 °C), as determined from the DSC analysis. Theoretically, the DSC temperature peak should match the OD temperature inflection point, since DSC measures heat flow as a response and OD measures shrinkage. Nonetheless, this difference of 4 °C is quite reasonable considering the inherent differences between these methods and devices. Thus, this shrinkage pertains to the crystallization process and indicates that the density of crystallized phase is slightly higher than that of the parent glass. Slighter expansions that occurred before and after the crystallization event were attributed to thermal expansion of the glass and the glass-ceramic, respectively. These kinds of expansion were seen in the entire temperature range and took place in

steps due to the precision limit of the equipment. The second event occurred above 1330 °C when the sample melts. The crystal phase in the resulting $Li_{1.4}Cr_{0.4}(Ge_{0.4}Ti_{0.6})_{1.6}(PO_4)_3$ glass-ceramic is a solid solution, so the crystallized phase begins to melt at about 1330 °C and finishes melting at 1346 °C when the entire sample is liquid (Figure 5.2). The latter temperature is the *liquidus* temperature and is considered here as T_m.

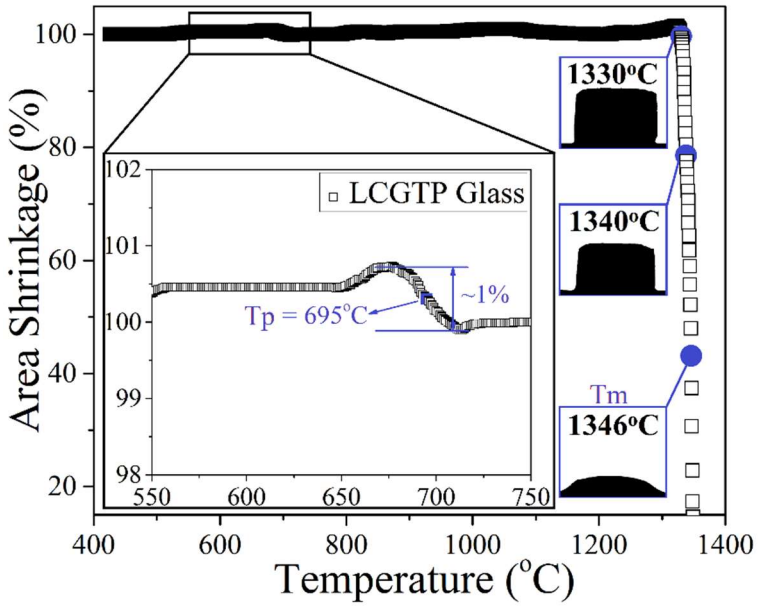

Figure 5.2 - Optical dilatometry data at a heating rate of 10 K min^{-1} for a parallelepiped sample of $Li_{1.4}Cr_{0.4}(Ge_{0.4}Ti_{0.6})_{1.6}(PO_4)_3$ glass. T_p and T_m, as well as some sample's photographs from the OD analysis, are included in the plot.

The reduced glass transition parameter ($T_{gr} = T_g(K)/T_m(K)$) was calculated based on the T_g taken from the DSC curve and the T_m from the OD results. This ratio is important because it indicates whether or not a glass presents homogenous nucleation. A T_{gr} below 0.6 is a compelling indication that the glass presents predominantly homogenous nucleation [67]. In this case, T_{gr} was found to be 0.553, providing evidence that this glass composition present volume crystallization by means of homogeneous nucleation [68]. Another relationship of interest is the Hrubÿ parameter ($K_H = [T_x(K)-T_g(K)]/[T_m(K)-T_x(K)]$) because it gives information about the glass forming ability of a melt. In fact, the K_H parameter is an empirical measure of the stability or resistance of the glass to crystallization

under heating. However, the correlation between glass stability and glass forming ability has already been established, especially in the case of the K_H parameter [69,70]. Thus, the higher the K_H, the more easily the glass is formed. The K_H value of the $Li_{1.4}Cr_{0.4}(Ge_{0.4}Ti_{0.6})_{1.6}(PO_4)_3$ glass (K_H = 0.105) is comparable to that of well-known homogeneous nucleating glass systems such as fresnoite (0.14) [71], lithium germanium phosphate (0.11) [56] and lithium diborate (0.096) [69].

To discover why a larger surface area impairs crystallization, we used IR analyses in reflectance mode, since this mode provides a primarily surface response. Thus, bulk and powder samples of $Li_{1.4}Cr_{0.4}(Ge_{0.4}Ti_{0.6})_{1.6}(PO_4)_3$ glass composition were previously heat-treated for 5 min at temperatures very close to the peak temperatures, i.e., 700 and 710 °C for bulk and coarse powder, respectively. The fine powder was heat-treated at 710 °C and 740 °C because this sample showed two distinguishable crystallization peaks on the DSC curve (Figure 5.1). Figure 5.3 depicts FT-IR analyses of bulk glass and glass powder before and after heat treatment. The bands at 2165 and 1650 cm^{-1} marked on the dotted line appear only in powder samples (Figure 5.3 c, d, e, f and g) and have been assigned to a combination of vibrational modes of the P-OH bond in phosphate glasses [72,73]. These results indicate that the presence of OH groups may be the reason why larger surface areas hinder the crystallization of powder samples. These OH groups are probably bonded to phosphorus atoms from the glass network on the particle surface and may have been introduced in the powder samples through exposure of particle surfaces to the atmospheric moisture during the grinding process. On the other hand, the bands marked by dashed lines, which are more distinguishable in heat-treated samples (Figure 5.3 a, c, e, and f), have been ascribed to PO_4/MO_6 interaction (1280 cm^{-1}), PO_4 (1185 cm^{-1}, 1025 cm^{-1}, 1120 cm^{-1} and 955 cm^{-1}), and MO_6 (640 cm^{-1}) vibrational modes in NASICON-like phosphates [74,75].

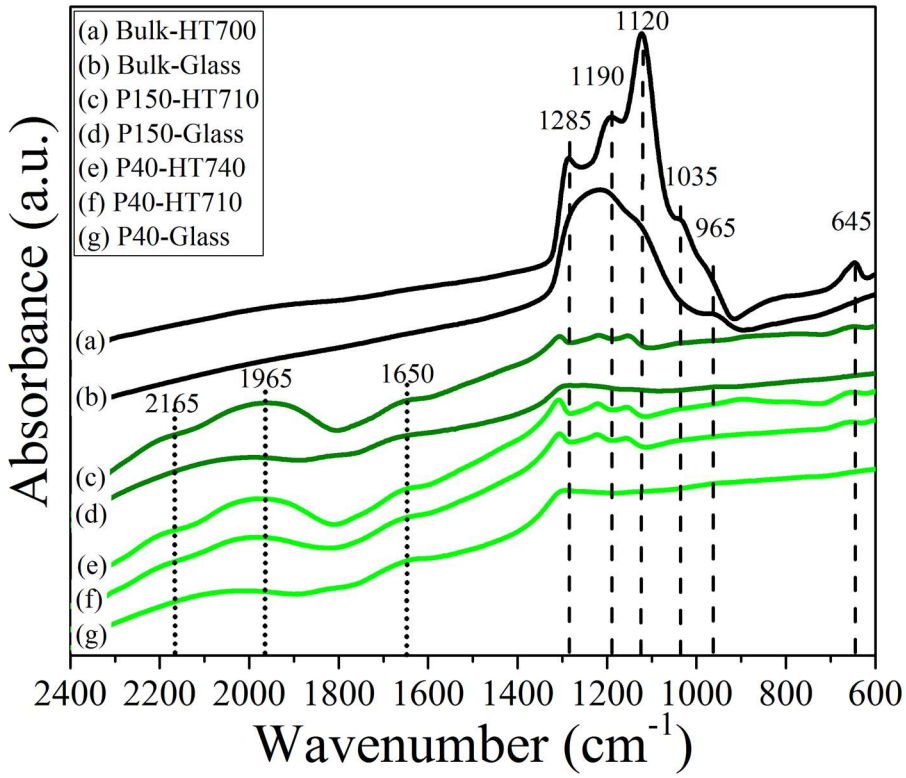

Figure 5.3 - FT-IR analyses of glass bulk and powder samples, before and after a 5 min heat treatment at a temperature close to Tp: (a) bulk glass heat-treated at 700 °C (HT700); (b) precursor glass as quenched (Bulk-Glass); (c) coarse powder heat-treated at 710 °C (P150-HT710); (d) coarse glass powder (P150-Glass); (e) fine glass powder heat-treated at 740 °C (P40-HT740); (f) fine glass powder heat-treated at 710 °C (P40-HT710); (g) fine glass powder (P40-Glass).

To characterize the crystalline phases in the heat-treated bulk, coarse and fine powder, these samples were subjected to XRD analyses, as shown in Figure 5.4. The NASICON $LiTi_2(PO_4)_3$-like phase (COD card 96-722-2156) is formed in every case, whether the sample is crystallized from powder or bulk form, and regardless of the heat treatment temperature employed. A small diffraction peak was attributed to a second minor phase, albeit its determination was unfeasible since only one small peak corresponding to this phase is detectable. Nevertheless, this peak is also visible in all cases and does not explain the differences in the crystallization behavior of bulk and powder samples. These results provide evidence that the two crystallization peaks (Figure 5.1) detected

through the DSC analysis in fine powder probably pertain to different crystallization mechanisms rather than to the formation of distinct phases.

The intensity of the XRD pattern increased as the heat treatment temperature increased. On the other hand, the XRD pattern of the finest powder (P40-HT710) is less intense than that of the coarse powder (P150-HT710) when treated at the same temperature (710 °C), again suggesting that the specific surface area does, in fact, hinder crystallization in the LCGTP glass system. The bulk glass shows less intense peaks, probably because of the lower heat treatment temperature applied.

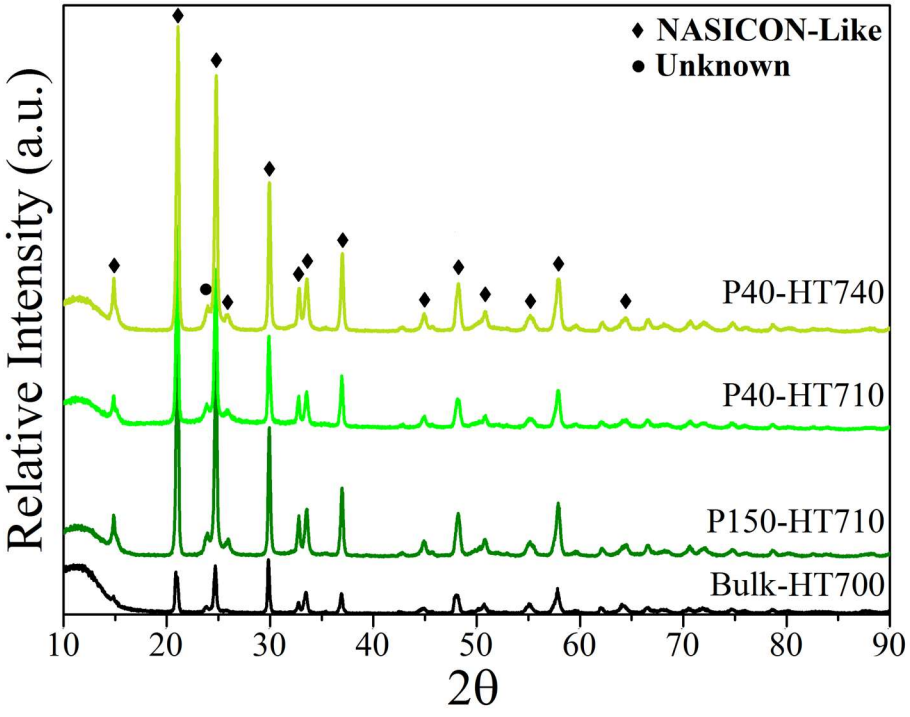

Figure 5.4 - XRD patterns of $Li_{1.4}Cr_{0.4}(Ge_{0.4}Ti_{0.6})_{1.6}(PO_4)_3$ glass heat-treated for 5 min as a bulk sample at 700 °C (Bulk-HT700), as coarse powder at 710 °C (P150-HT710), and as fine powder at 710 °C (P40-HT710) and 740 °C (P40-HT740).

5.1.2 Formation of NASICON-like phase

To produce highly crystalline glass-ceramics, bulk glass samples were crystallized for 12 h at different temperatures. Figure 5.5 illustrates the XRD results of bulk samples heat-treated at 700 °C, 800 °C, 900 °C and 1000 °C for 12 h. Again, diffraction pattern corresponding to NASICON-type structure was

detected in all the glass-ceramics and the intensity of the XRD pattern increases along with the heat treatment temperature (see intensity bars, Figure 5.5). This behavior is well known, and has already been observed in a number of glass-ceramics with NASICON-like phase [57,76,77]. The unknown secondary phase was also detected in the glass-ceramics heat-treated for 12 hours (Figure 5.4).

Moreover, the most intense peaks in the XRD pattern shift toward lower 2 theta angles as a function of heat treatment temperature, which means that the lattice parameters of the NASICON-type structure increase along with increasing heat treatment temperature. As NASICON-type structure has a rhombohedral lattice (space group R-3C, trigonal system), its lattice parameters can also be represented on hexagonal axes [44]. Thus, the lattice parameters and the volume of unit cell were estimated based on the diffraction angle of the most intense peaks (planes [104] and [113]) through Eq. 3.1 and Eq. 3.2, respectively.

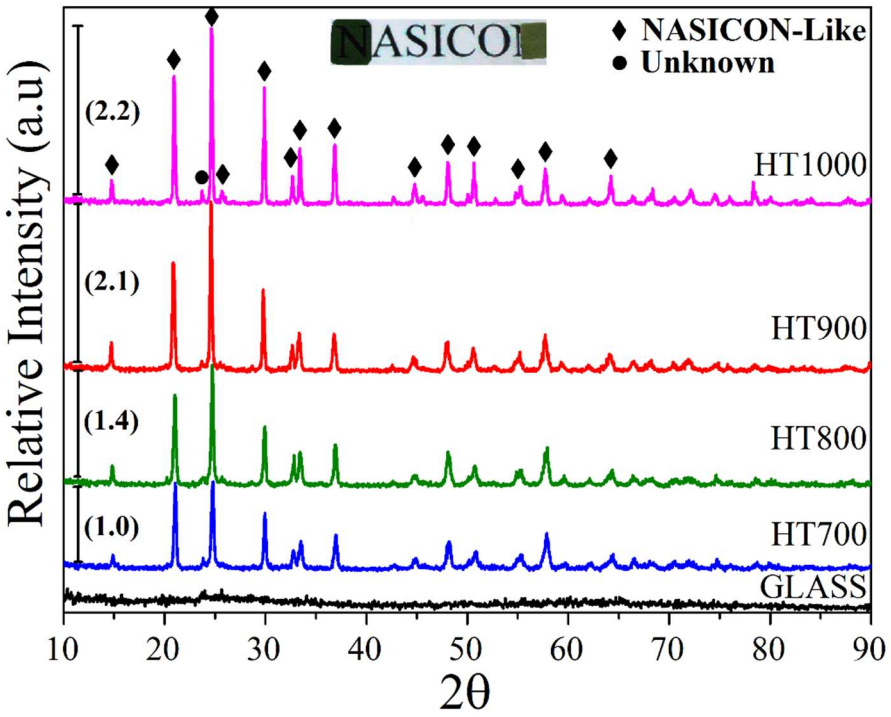

Figure 5.5 - XRD patterns of $Li_{1.4}Cr_{0.4}(Ge_{0.4}Ti_{0.6})_{1.6}(PO_4)_3$ bulk glass and glass-ceramics heat-treated for 12 h at 700 °C (HT700), 800 °C (HT800), 900 °C (HT900) and 1000 °C (HT1000). A cropping of a digital photograph of the glass (left) and glass ceramic (right) is also shown.

Figure 5.6 shows the dependence of the lattice parameters (a and c) and volume of the NASICON-type structure on the heat treatment temperature. As can be clearly seen, the unit cell volume shows practically no variation between the heat treatment at 700 °C and at 800 °C, and increases considerably in response to the heat treatment at 900 °C, but slightly drops again after the heat treatment at 1000°C. Since the proposed composition leads to a solid solution, a possible explanation for this behavior is that some components in the residual glassy phase or segregated at the grain boundary were incorporated into the NASICON-like phase, causing structural changes in the NASICON-type unit cell from 800 °C to 900 °C heat-treatment. In the case of sample heat treatment at 1000 °C (HT1000), the opposite might be occurred, with some oxides being expelled from the NASICON-type structure leading to a shrinkage of NASICON-type unit cell.

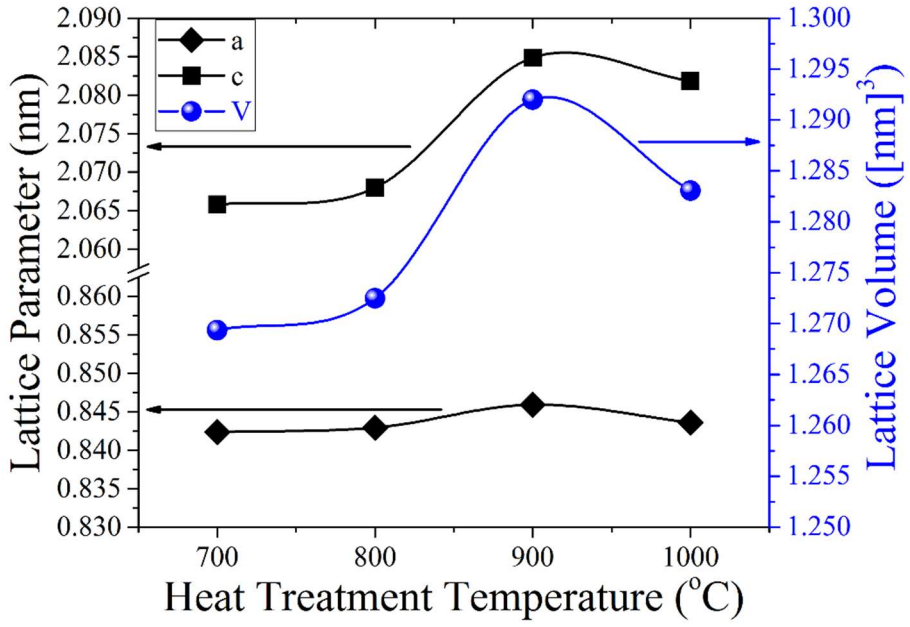

Figure 5.6 - Dependence of the lattice parameters (a and c) and lattice volume of the NASICON-type structure on heat treatment temperatures.

In summary, the estimated lattice parameters for $Li_{1.4}Cr_{0.4}(Ge_{0.4}Ti_{0.6})_{1.6}(PO_4)_3$ glass-ceramics are slightly lower than that of $LiTi_2(PO_4)_3$ (a = 0.851 nm and c = 2.084 nm), COD card 96-722-2156, and higher than the lattice parameters (a = 0.829 nm and c = 2.053 nm) found by Xu [78] in

$Li_{1.4}Cr_{0.4}Ge_{1.6}(PO_4)_3$ glass-ceramics. HT900 sample presented lattice parameters (a = 0.846 nm and c = 2.085 nm) very close to those of $LiTi_2(PO_4)_3$. These results are in perfect agreement with our previous prediction that, the proposed $Li_{1+x}Cr_x(Ge_yTi_{1-y})_{2-x}(PO_4)_3$ system can indeed result in lattice parameters comparable to those of $LiTi_2(PO_4)_3$ through compositional tailoring.

5.1.3 Microstructure

Figure 5.7 shows SEM micrographs of the fractured surfaces of $Li_{1.4}Cr_{0.4}(Ge_{0.4}Ti_{0.6})_{1.6}(PO_4)_3$ glass-ceramics at distinct magnification levels. In overall, it is possible to note the low porosity of the glass-ceramic samples. More specifically, HT700 and HT800 samples show irregular fracture surfaces with underdeveloped grains smaller than 1 μm of undefined shape. On the other hand, HT900 and HT1000 samples show typical NASICON-like phase cubic-shaped grains [48,57,79,80] larger than 1 μm. Moreover, sample HT1000 shows a very regular microstructure typical of intergranular fracture. In summary, these results also confirm the prevalence of internal crystallization in this glass, since surface-crystallized glass-ceramics usually show textured microstructures with elongated grains grown from the surface. The SEM micrograph of sample HT1000 also shows spherical grains indicated by arrows, which are discussed later.

The low porosity of HT900 sample was confirmed by a rough estimation using the apparent and the theoretical density of this sample. Its apparent density (2.98 g/cm^3) was estimated by using the sample's dimensions and mass. On the other hand, the theoretical density (3.14 g/cm^3) was calculated considering six formula units and the nominal molar mass (407.9 g/mol) of the studied composition. The unit cell volume of the sample HT900 was calculated using the lattice parameters determined from XRD analysis. It is true that this estimated value of density does not consider the residual glassy phase or other secondary phases. Even though, this estimation leads to a relative density of 95% for the HT900 sample, which is in good agreement with SEM micrograph shown in Figure 5.7.

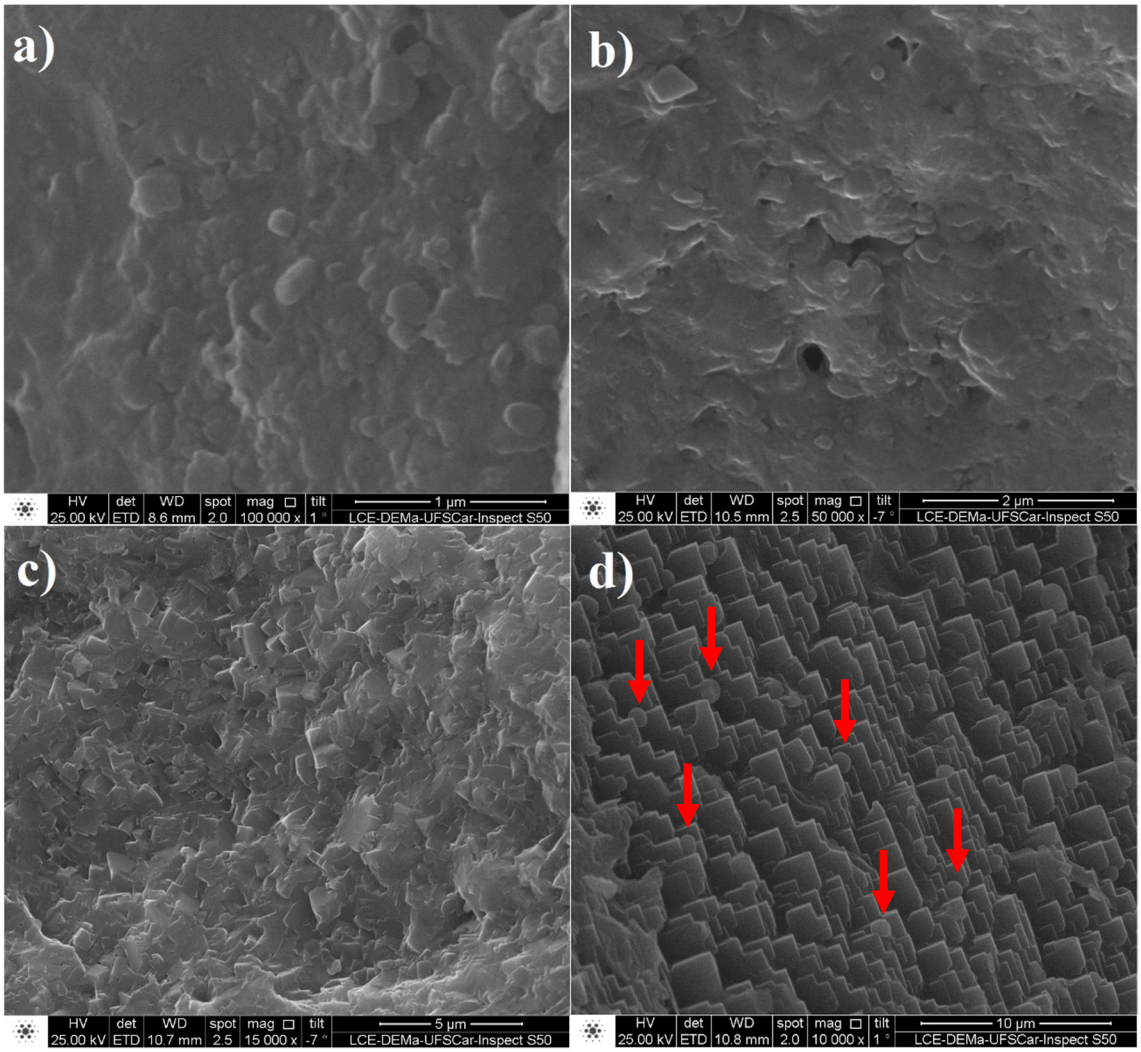

Figure 5.7 - SEM micrographs of surface fractures of $Li_{1.4}Cr_{0.4}(Ge_{0.4}Ti_{0.6})_{1.6}(PO_4)_3$ glass-ceramics heat-treated at different temperatures: (a) HT700, (b) HT800, (c) HT900 and (d) HT1000. Since the samples presents very different grain size, the micrographs are shown under distinct levels of magnification, namely 100,000X for HT700, 50,000X for HT800, 15,000X for HT900 and 10,000X for HT1000 samples. A qualitative measurement of the grains size can be accessed through the scale bars. The arrows indicate a distinct grain morphology.

The chemical composition of all the glass-ceramics was examined by EDX under 1,000X magnification (area of about 0.1 mm^2) in three different regions of the samples. Table 5.1 shows the average results and their respective standard errors. Lithium is not detectable in chemical characterizations by EDX, so our calculations were based on its nominal composition. Given that glass-ceramics

derive from the same glass, they should have the same chemical composition. Deviations between samples were lower than 5% in every case and for all the oxides and lower than 3% between samples and their nominal chemical compositions. The chemical compositions of spherical and cubic grains which were revealed under 100,000X magnification in sample HT1000 were also determined by EDX. The spherical grains were found to contain about 20 mol% of silicon which was not found in any of the other analyses. Therefore, it is reasonable to infer that the silicon impurity is concentrate in these spherical grains and was not detect when the overall sample is analyzed because the total silicon content is probably out of the detection limit of the equipment. This impurity was more likely introduced by the chemical reactants used to synthesize the parent glass since there was no contact with silicon sources in any other step of the synthesis process.

Table 5.1 - EDX chemical analysis of the glass-ceramics examined in this study, and local EDX chemical analysis of different grain shapes in sample HT1000.

Oxides	Nominal (mol%)	HT700 (mol%)	HT800 (mol%)	HT900 (mol%)	HT1000 (mol%)	HT1000 Cubic (mol%)	HT1000 Spherical (mol%)
Cr_2O_3	5.0	4.8 (1)	5.9(2)	5.04(5)	4.53(8)	4.2	2.9
GeO_2	16.0	16.7(2)	17.2(5)	17.1(5)	18.9(5)	16.0	13.5
TiO_2	24.0	23.0(7)	26.3(5)	23.1(4)	23.7(9)	21.2	15.1
P_2O_5	37.5	39.9(4)	35.1(3)	39.3(5)	37.4(3)	42.4	32.4
SiO_2	0.0	-	-	-	-	0.7	20.7

5.1.4 Electrical behavior

The EIS data of the $Li_{1.4}Cr_{0.4}(Ge_{0.4}Ti_{0.6})_{1.6}(PO_4)_3$ glass and glass-ceramics revealed typical ion-conductive behavior. The impedance complex plot shows a spike of points at low frequency resulting from the effect of ionic polarization [48,56,57,78], which indicates that the main charge carrier in these glasses and glass-ceramics are ions. Figure 5.8 shows a representative set of data obtained from the EIS analyses of $Li_{1.4}Cr_{0.4}(Ge_{0.4}Ti_{0.6})_{1.6}(PO_4)_3$ glass-ceramics. Here, the complex impedance (Z^*) plots have been normalized by the shape factor of each sample ($Z^*/[L/A]$, thickness over area) given rise to what we have called specific impedance (Z_S^*). This approach allows one to make direct comparison on

differences in the electrical behavior of samples since the resistivity of samples can be promptly read on the real axis (Z_S'). Figure 5.8a shows frequency-color map of impedance data of HT700 glass-ceramic recorded at room temeprature (RT). An analysis of the complex impedance plot reveals three distinct contributions, namely, in the low-frequency range (10^3 – 1Hz), a spike related to lithium ions being blocked by the sputtered gold electrodes; in the medium frequency range (10^3 – 10^6Hz), a depressed semi-circle related to grain boundary impedance; and in the high frequency range (>10^6Hz), a partial semi-circle related to grain impedance. Figure 5.8b presents impedance data obtained at RT (300K) for the glass-ceramic samples HT700, HT800 and HT900. As can be promptly seen, the heat treatment temperature has an important influence on the total resistivity of the $Li_{1.4}Cr_{0.4}(Ge_{0.4}Ti_{0.6})_{1.6}(PO_4)_3$ glass-ceramic samples.

In order to separate these different contributions, impedance data were fitted based on an equivalent circuit comprising a parallel combination of resistance (R_g) and capacitance (C_g) attributed to the grain contribution ($R_g|C_g$), in series with a parallel combination of a resistance (R_{gb}) and a constant-phase element (CPE_{gb}) attributed to the grain boundary contribution ($R_{gb}|CPE_{gb}$) and in series with a constant-phase element (CPE_e) which accounts for the electrode polarization effects in the low frequency region (Figure 5.8a). Note that the equivalent circuit used here does not comprise an R_0 circuit element related to the resistance and/or inductance of the cell measurement or equipment. Although the use of R_0 is very common in the literature [81–83], this approach can lead to misinterpretation, since this R_0 parameter usually is unknown and is usually a free parameter in fitting procedures. Thus, the impedance of the equipment can be overestimated in detriment to that of the sample, which leads to an overestimation of the sample's conductivity. This is particularly true when samples are highly conductive, and the frequency range used in the measurement is not broad enough to encompass all the electrical behavior of the grain contribution. In this work, we chose to ensure a near zero equipment impedance by means of calibration, which allows us to work with an equivalent circuit without R_0. It is worth to note that this approach can lead to an underestimation of total conductivity but never an overestimation.

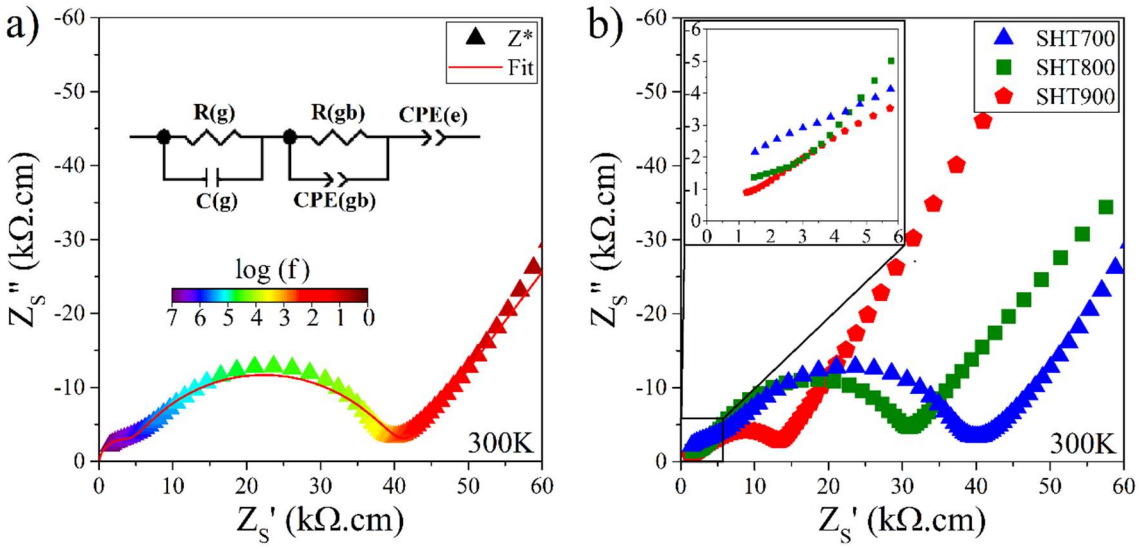

Figure 5.8 - Set of EIS analyses of $Li_{1.4}Cr_{0.4}(Ge_{0.4}Ti_{0.6})_{1.6}(PO_4)_3$ glass-ceramics represented by: (a) a fit of impedance data of the glass-ceramic HT700 recorded at 300K, based on the indicated equivalent circuit; (b) Z_S* plots at 300K of glass-ceramic samples HT700, HT800 and HT900. Data of glass and HT1000 samples are not shown here due to scale compatibility.

Figure 5.8a shows an example of the complex impedance plot, including experimental data and the result of fitting, as well as the equivalent circuit ($[R_g|C_g]$ - $[R_{gb}|CPE_{gb}]$ - CPE_e) used in the fitting procedure. In the case of the glass sample, the equivalent circuit ($[R_a|CPE_a]$ - CPE_e) has only a parallel combination of a resistance (R_a) and a constant-phase element (CPE_a) in series with a constant-phase element (CPE_e) to describe the electrode polarization. The impedance of the constant-phase element (CPE) is given by Eq. 5.1, where ω is the angular frequency and Q_{CPE} and n_{CPE} refer, respectively, to the capacitance and depression angle ($n_{CPE} \leq 1$) [24,47,48,79].

$$Z_{CPE} = \frac{1}{Q_{CPE}(i\omega)^{n_{CPE}}} \qquad \text{(Eq. 5.1)}$$

In all the glass-ceramics and in the entire temperature range, fitting results of the grain capacitance (C_g) showed values varying from $8x10^{-12}$ to $9x10^{-11}$ F, which agrees with the range proposed by Irvine et al. [25]. The effective capacitance (C_{gb}) of the grain boundary was determined based on Eq. 5.2 [24,47,48,79] and ranged from $1x10^{-10}$ to $2x10^{-9}$ F, also in agreement with Irvine et al. [25], while the fitting parameter n_{gb} was found to range from 0.6 to 0.9. The

electrode capacitance of the fitted data in Figure 5.8a was found to be $5.3x10^{-6}F$. A rough estimation, considering a monolayer of Li^{+1} ions with an ionic radius of 76 pm blocked on both sides of the electrode, based on the electrode area of the HT700 sample ($0.167cm^2$) and a reasonable ε_r of 2, results in a capacitance of $1.9x10^{-6}F$. Thus, all the fitting results were reasonable for the polycrystalline ionic conductor class [25], suggesting that the equivalent circuit used here can adequately describe the electrical behavior of the electrolytes investigated in this study.

$$C_{gb} = \frac{(R_{gb}Q_{gb})^{\frac{1}{n_{gb}}}}{R_{gb}} \qquad \text{(Eq. 5.2)}$$

The total ionic conductivity of $Li_{1.4}Cr_{0.4}(Ge_{0.4}Ti_{0.6})_{1.6}(PO_4)_3$ glass and glass-ceramics, were determined by applying the relation $\sigma = 1/\rho$ to the values of R_a and $R_g + R_{gb}$ (obtained by fitting), respectively. As the impedance data have previously been normalized by the sample's shape factor, the values obtained by fitting indicate the resistivities (ρ).

The dependence of total ionic conductivity on the inverse of temperature was plotted following the Arrhenius-like relation expressed in Eq. 2.5 [6], where k_B is Boltzmann's constant, T is the absolute temperature, σ_0' is the pre-exponential factor, and E_a' is the activation energy for ion conduction. Figure 5.9 shows the Arrhenius-like plot of total ionic conductivity for glass-ceramics obtained at different temperatures, together with the ionic conductivity of the $Li_{1.4}Cr_{0.4}(Ge_{0.4}Ti_{0.6})_{1.6}(PO_4)_3$ precursor glass. The ionic conductivity of glass-ceramics is up to 5 orders of magnitude higher than that of the parent glass. This result demonstrates how specific the NASICON-type structure is, since the conductivity of a particular glass is usually higher than that of its isochemical crystal [36]. Also, the glass-ceramics obtained with a single heat treatment at 900°C (HT900) showed the highest total conductivity in the entire temperature range ($6.6 \times 10^{-5}\Omega^{-1}.cm^{-1}$ at 300K).

The activation energy for ion conduction in the glass and glass-ceramics was calculated by linear regression of the experimental points shown in Figure 5.9. Table 5.2 summarizes the total ionic conductivity at RT (300K), as well as the related activation energy (E_a'$_t$) and the logarithm of the pre-exponential term

(log(σ_0'$_t$)). Comparing the results related to total contribution of conductivity. Comparing the results related to total contribution of conductivity (Table 5.2 it becomes clear that the main difference between them lies in the E_a'$_t$ since the values of log(σ_0'$_t$) in glass and glass-ceramics are comparable.

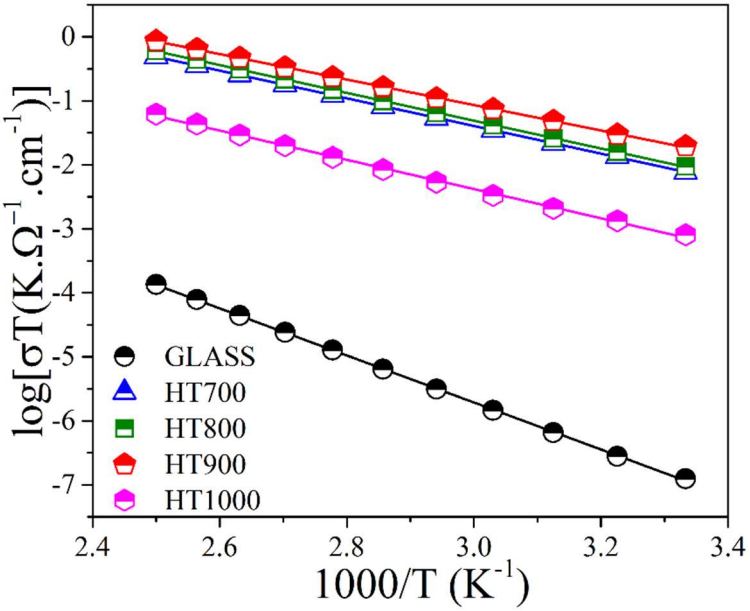

Figure 5.9 - Arrhenius plot of total ionic conductivity of the $Li_{1.4}Cr_{0.4}(Ge_{0.4}Ti_{0.6})_{1.6}(PO_4)_3$ glass-ceramics heat-treated at 700 °C (HT700), 800 °C (HT800), 900 °C (HT900) and 1000°C (HT1000). The ionic conductivity of the precursor glass is also shown.

In the case of glass-ceramics, it was also possible to separate the contributions of the grain and the grain boundary. As a matter of fact, since the geometrical factor (L/A) of grains and grain boundaries is unknown, only their apparent contribution can be estimated based on the geometrical factor of the whole sample. Thus, the apparent contributions of grains and grain boundaries were also calculated using the relation $\sigma = 1/\rho$, but now, using the obtained R_g and R_{gb} data separately [47,48,79]. Figure 5.10 shows an Arrhenius-like plot of the grain and grain boundary apparent contribution of ionic conductivity obtained at different temperatures.

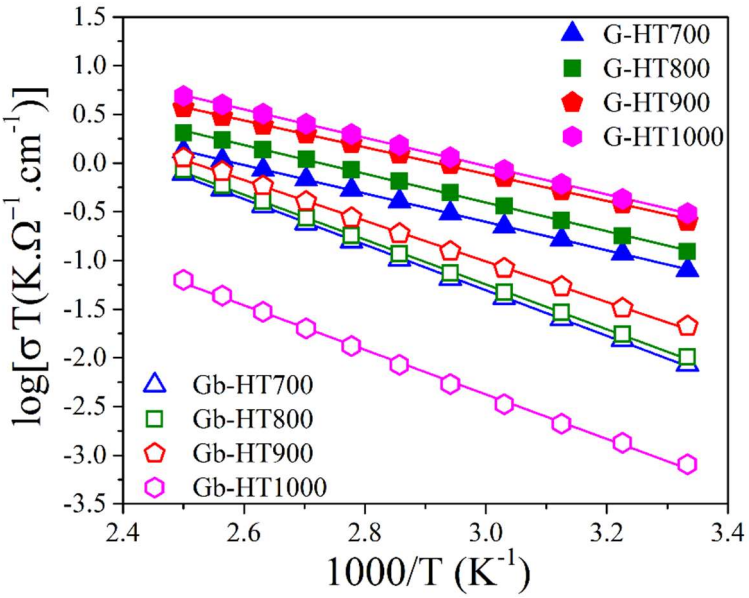

Figure 5.10 - Arrhenius plot of grain (closed symbols) and grain boundary (open symbols) apparent ionic conductivity as a function of inverse temperature in $Li_{1.4}Cr_{0.4}(Ge_{0.4}Ti_{0.6})_{1.6}(PO_4)_3$ glass-ceramics heat-treated at distinct temperatures.

Values of σ, E_a' and log(σ_0') related to the apparent contribution of grains and grain boundaries in the synthesized glass-ceramic are also summarized in Table 5.2. A notably high grain conductivity of $1x10^{-3}\Omega^{-1}.cm^{-1}$ at RT was found for the glass-ceramic HT1000. The activation energy of grain conductivity ($E_a'_g$) decreases as a function of heat treatment temperature, except in sample HT1000. Thus, the glass-ceramic HT900 showed the lowest $E_a'_g$ (0.274(3) eV), which also led to high grain conductivity ($8.5 \times 10^{-4}\Omega^{-1}.cm^{-1}$) at RT. It is also interesting to note that grain boundaries have lower apparent conductivity and higher activation energy than grains. The lower conductivity can be predicted from the impedance plots (Figure 5.8), which show much larger semicircles relate to grain boundary resistivity (middle-frequency) in comparison to those attributed to the grain contribution (high-frequency). This also indicates that the grain boundary limits the total ionic conductivity in these glass-ceramics. Additionally, the grain boundary activation energy tends to decrease with heat treatment temperature, except in the sample heat-treated at 1000 °C, indicating that increased heat treatment temperature also has a beneficial effect on the grain boundary contribution, up to 900 °C.

The results in Table 5.2 indicate that the activation energies related to grain contribution are the same within experimental errors, in samples heat-treated at 700 and 800°C, with a minimum in the sample heat-treated at 900 °C, and then, increases again in the sample heat-treated at 1000°C. This trend may be correlated to the variation of the lattice volume Figure 5.6, which exhibits a maximum in the sample heat-treated at 900 °C. Thus, sample HT900 presented both the maximum volume lattice and the minimum activation energy related to grain ionic conductivity. The relationship between lattice volume and activation energy for ion conduction has been already reported in the literature [37,77,78]. However, we found no reports relating the dependence of $E_a'_g$ to the NASICON volume lattice caused by different heat treatments. Concerning grain boundary contribution, $E_a'_{gb}$ follows roughly the same trend as grain contribution.

Table 5.2 - Total ionic conductivity at room temperature (σ_t), activation energy ($E_a'_t$) and the pre-exponential term ($\log(\sigma_0'_t)$) of $Li_{1.4}Cr_{0.4}(Ge_{0.4}Ti_{0.6})_{1.6}(PO_4)_3$ glass and glass-ceramics. Ionic conductivity, E_a' and $\log(\sigma_0')$ of grains and grain boundaries are also showed. The uncertainties indicated here are mathematical errors taken from the linear regression.

Sample	Total			Grains			Grain Boundaries		
	RT σ_t ($S.cm^{-1}$)	$\log(\sigma_0'_t)$ ($S.cm^{-1}$)	$E_a'_t$ (eV)	σ_{300K} ($S.cm^{-1}$)	RT σ_t ($S.cm^{-1}$)	$\log(\sigma_0'_t)$ ($S.cm^{-1}$)	E_a' (eV)	$\log(\sigma_0')$ ($S.cm^{-1}$)	RT σ_t ($S.cm^{-1}$)
Glass	$4.2x10^{-10}$	5.31(5)	0.730(3)	-	-	-	-	-	-
HT700	$2.6x10^{-5}$	5.09(2)	0.429(1)	$2.7x10^{-4}$	3.78(1)	0.290(1)	$2.8x10^{-5}$	5.72(5)	0.465(4)
HT800	$3.2x10^{-5}$	5.21(1)	0.432(1)	$4.1x10^{-4}$	4.02(4)	0.293(3)	$3.4x10^{-5}$	5.67(4)	0.458(4)
HT900	$6.6x10^{-5}$	4.90(3)	0.395(2)	$8.5x10^{-4}$	4.02(4)	0.274(3)	$7.1x10^{-5}$	5.26(5)	0.414(4)
HT1000	$2.2x10^{-6}$	4.47(4)	0.454(6)	$1.0x10^{-3}$	4.33(2)	0.289(1)	$2.9x10^{-6}$	4.49(1)	0.455(6)

Nonetheless, the main finding regarding the grain boundary contribution was the $\log(\sigma_0'_{gb})$ term for sample HT1000, which dropped by about one order of magnitude compared to the other glass-ceramics. This was probably the main reason why sample HT1000 exhibited the lowest total ionic conductivity at RT (Table 5.2). A reasonable explanation may be a poorer contact between grains or cracks introduced in the heat treatment stage [48]. In fact, while all the glass-ceramics showed considerable mechanical strength (impossible to break manually), sample HT1000 was brittle and broke easily when handled. Also, the

SEM analysis of sample HT1000 indicated a typical intergranular fracture, which may justify its precarious mechanical strength and may also explain the drop of grain boundary conductivity resulting from deficient contact between grains.

5.2 Glass and Glass-ceramics of LCGTP Compositions

5.2.1 Chemical characterization of LCGTP glasses

Several aqueous mixtures of acids and even bases have been tested to digest the glass samples, but only HF proves to be effective. The samples with higher Cr and Ti content (LCGTP0206, LCGTP0208 and LCGTP0408) have not been digested even after weeks. Therefore, LCGTP0202, LCGTP0404, LCGTP0606, and LCGTP0808 glass samples have been chosen to represent the complete set of compositions, given their low Ti or Cr content and the fact that they cover the entire range of x and y values. Table 5.3 describes the nominal and experimental chemical composition of these samples, in weight percent. As the oxygen content cannot be determined by wet chemical analysis, calculations are made based on the nominal oxygen content. However, this assumption is quite reasonable, since the oxidation state used in the calculation of all the elements is the most common one.

Table 5.3 - Nominal and experimental chemical composition, in weight percent (wt.%), of the LCGTP0202, LCGTP0404, LCGTP0606, and LCGTP0808 glass samples.

Sample	Nominal (wt.%)					Experimental (wt.%)				
	Li	Cr	Ge	Ti	P	Li	Cr	Ge	Ti	P
LCGTP0202	2.1	2.6	6.6	17.3	23.3	2.1	2.5	6.0	16.7	24.5
LCGTP0404	2.4	5.1	11.4	11.3	22.8	2.3	5.0	10.5	10.7	24.5
LCGTP0606	2.7	7.5	14.7	6.5	22.4	2.7	7.1	14.1	6.4	23.4
LCGTP0808	3.0	9.9	16.6	2.7	22.1	3.2	8.9	16.1	2.8	23.3

In summary, all the elements show unsystematic discrepancies between nominal and experimental concentrations, but in every case, the relative discrepancy is lower than 10%. These discrepancies, which are expected, are attributed to evaporation during melting and to experimental errors intrinsic to chemical analysis. A systematic discrepancy is also detected in the phosphorus

content, whose relative perceptual in all the analyzed compositions is about 5% higher. This indicates that the 5% addition made in the formulation step is unnecessary, at least when it comes to short synthesis times. The most important point here is that, in every case, the progressive increase/decrease of Li, Cr, Ge and Ti is maintained (Table 5.3). This is a crucial point in discussing the properties of these glasses and glass-ceramics. For the sake of simplicity, from now on, all the compositions are discussed based on their nominal content.

5.2.2 Thermal characterization of LCGTP glasses

The DSC analysis indicates that all the LCGTP glasses have shown a clear glass transition and a narrow and very intense crystallization. Figure 5.11 depicts the DSC curves of four LCGTP glasses (series x=0.2), showing the glass transition temperature, T_g (Figure 5.11a), and the crystallization peak temperature, T_p (Figure 5.11b). Note the considerable shift of T_g to lower temperatures as y increases (proportional to the Ge content), while T_p changes by only a few degrees. All the other LCGTP glass series, x=0.4, x=0.6 and x=0.8, have exhibited essentially the same behavior. Usually, T_g is determined from the inflection point, and T_p is ascribed to the crystallization peak temperature of the DSC curve. However, to determine T_g and T_p more precisely and without the influence of the experimenter, we have adopted a more rigorous method than a simple plot visualization. Therefore, the first derivative of the DSC curve is used to ascertain these specific temperatures. In this case, T_g can be determined when the first derivative in the glass transition region reaches a minimum value, while T_p is the temperature at which the first derivative reaches zero in the domain of the crystallization peak (Figure 5.11c). Also, the melting temperature (T_m) of the crystallized phase has been determined using optical dilatometry (OD). Figure 5.11d shows the shrinkage area of the same four LCGTP glass compositions as a function of temperature. A slight shrinkage of about 1%, attributed to glass crystallization, is visible at around 700°C, as previously discussed. Above this temperature, LCGTP glass-ceramics show only minor dimensional changes until they begin to melt above 1200°C. Since the $Li_{1+x}Cr_x(Ge_yTi_{1-y})_{2-x}(PO_4)_3$ system is a solid solution, the crystallized phase melts within a temperature range of about

30°C, depending on the chemical composition. Thus, T_m is ascribed to the *liquidus* temperature (T_l) when the sample has been entirely melted (see Figure 5.11d, half-filled circles).

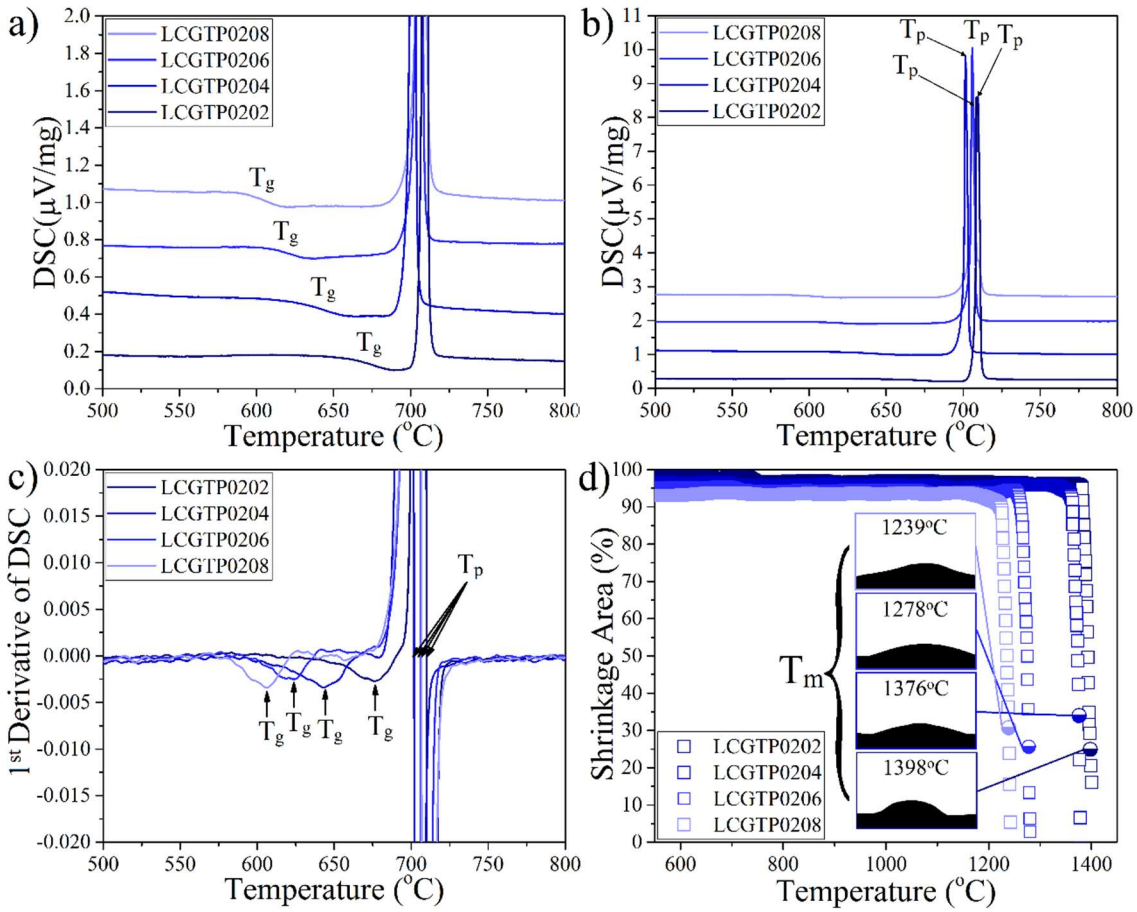

Figure 5.11 - DSC and OD analyses of four LCGTP glasses (x=0.2 series) at a heating rate of 10K.min^{-1}, indicating: (a) T_g, (b) T_p, (c) 1st derivative method, and (d) T_m of the corresponding LCGTP glasses.

Table 5.4 summarizes the thermal parameters (T_g, T_p and T_m) obtained for the sixteen LCGTP glasses. Based on the values of T_g from DSC measurements, and of T_m from the OD analysis, we have calculated the reduced glass transition parameter (T_{gr}). As previously pointed out, this ratio can provide information about the nucleation mechanism in a particular glass [67,68]. As can be seen in Table 5.4, the sixteen LCGTP glasses under study have shown T_{gr}<0.6, indicating that these glass compositions nucleate homogenously, which is desirable to design the final microstructure of a glass-ceramic [54,56,57,67]. The

Hrubÿ parameter ($K_H = T_x-T_g/T_m-T_x$) was also used here to calculate the glass stability of the entire composition range of LCGTP glasses. For the sake of simplicity, we chose to use T_p instead of the onset crystallization temperature (T_x) to calculate K_H. As Nascimento et al. [69] have shown, in the glass stability case, these terms are interchangeable with no loss of accuracy.

Table 5.4 - Thermal parameters (T_g, T_p, and T_m), as well as the Hrubÿ parameter (K_H) and reduced glass transition (T_{gr}) of the 16 investigated LCGTP glasses.

Sample	x	y	T_g (ºC)	T_p (ºC)	T_m(ºC)	K_H	T_{gr}
LCGTP0202	0.2	0.2	676.3	709.9	1398	0.049	0.57
LCGTP0204	0.2	0.4	643.7	701.8	1376	0.086	0.56
LCGTP0206	0.2	0.6	623.8	706.1	1278	0.144	0.58
LCGTP0208	0.2	0.8	606.3	706.7	1239	0.189	0.58
LCGTP0402	0.4	0.2	677.6	709.6	1384	0.048	0.57
LCGTP0404	0.4	0.4	647.7	706.9	1336	0.094	0.57
LCGTP0406	0.4	0.6	631.1	724.0	1278	0.168	0.58
LCGTP0408	0.4	0.8	606.6	723.0	1221	0.234	0.59
LCGTP0602	0.6	0.2	682.5	725.8	1396	0.065	0.57
LCGTP0604	0.6	0.4	657.2	729.8	1356	0.116	0.57
LCGTP0606	0.6	0.6	622.8	715.0	1289	0.161	0.57
LCGTP0608	0.6	0.8	613.4	714.8	1232	0.196	0.59
LCGTP0802	0.8	0.2	680.4	726.5	1405	0.068	0.57
LCGTP0804	0.8	0.4	659.7	726.5	1373	0.103	0.57
LCGTP0806	0.8	0.6	633.3	708.4	1329	0.121	0.57
LCGTP0808	0.8	0.8	614.1	700.7	1241	0.160	0.59

Figure 5.12 illustrates the dependence of the K_H parameter on x (Cr content) and y (proportional to the Ge content). In summary, the K_H values in the entire LCGTP series vary from 0.05 to 0.23, where the upper part of this range is comparable to well-known glass forming systems such as lithium diborate (K_H = 0.096), lithium germanium phosphate (0.11), fresnoite (K_H = 0.14) and anorthite (0.25) [56,69]. As expected, since GeO_2 is a good glass former, the stability of LCGTP glasses increases substantially in response to increasing Ge content, in every x series. Regarding the effect of chromium, the glass stability of the 0.2 y series also seems to increase with Cr content. On the other hand, in the 0.4, 0.6, and 0.8 y series, the glass stability increases with low Cr content but begins to decrease again after reaching a certain point. It should be kept in mind that the increase of Cr content is followed by a decrease in both Ti and Ge content,

according to the chemical formula ($[Ge_yTi_{1-y}]_{2-x}$), making this a more complicated analysis.

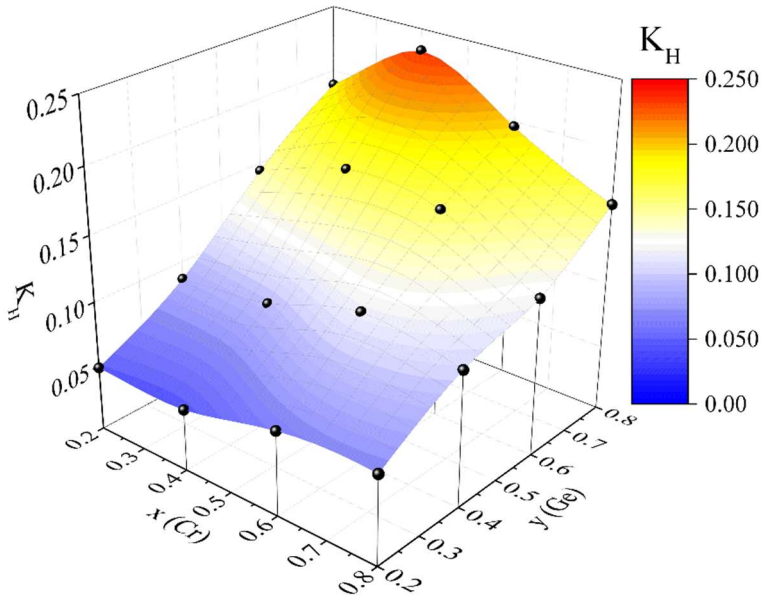

Figure 5.12 - Dependence of the K_H parameter of $Li_{1+x}Cr_x(Ge_yTi_{1-y})_{2-x}(PO_4)_3$(LCGTP) glasses on x (Cr content) and y (proportional to the Ge content).

Because the Ge content is related to y but is also dependent on x (Ge = y[2-x]), we have also plotted the glass stability parameter as a function of the GeO_2 nominal molar content (as shown in Table 4.1) for each x series (Figure 5.13). This enabled us to isolate the effect of GeO_2 from the Cr_2O_3 content. Pearson's correlation coefficient (r) between the K_H parameter and the GeO_2 nominal content of all the LCGTP glasses (r_{all} = 0.921) indicates a significant correlation between those variables (dashed line, Figure 5.13a).

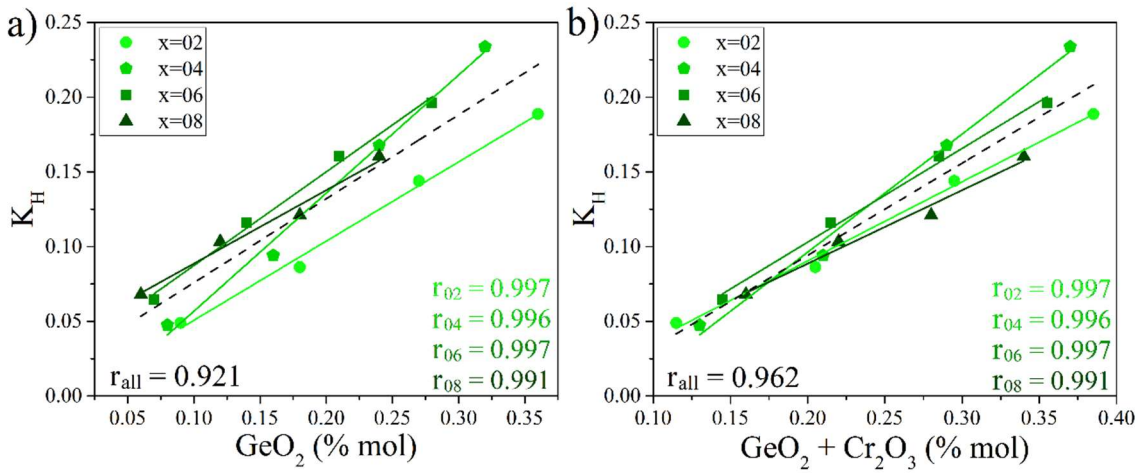

Figure 5.13 - Dependence of the K_H parameter of the four x series on (a) GeO_2 and (b) GeO_2 plus Cr_2O_3 content. The correlation coefficient (r) of each x series (solid line) and of all the LCGTP glasses together (dashed line) is also shown.

Moreover, when the x series are evaluated separately (r_{02}, r_{04}, r_{06} and r_{08}), the correlation between K_H and GeO_2 content is even higher (solid lines, Figure 5.13a). To determine the influence of Cr_2O_3 on the stability of LCGTP glasses, we examined the joint influence of Cr_2O_3 and GeO_2 content on the K_H parameter (Figure 5.13b). As expected, the correlation within a particular x series (solid lines, Figure 5.13b) is the same as the correlation with GeO_2 content. However, an increase in the r coefficient when all LCGTP glasses are considered (r_{all} = 0.962) indicates that Cr_2O_3 also plays a positive role in the glass stability parameter (dashed line, Figure 5.13b). In conclusion, this result suggests that although Cr is not considered a glass former like Ge, it might play an intermediate role like Al_2O_3 in glass melts [55].

5.2.3 Structural characterization of LCGTP glass-ceramics

After crystallization, LCGTP samples become opaque, and their greenish color becomes less intense than that of the precursor glass (see Figure 5.14). Figure 5.14 shows XRD patterns of the sixteen LCGTP glass-ceramics obtained by heat-treating the precursor glass for two hours at 900°C. A typical diffraction pattern of NASICON-type structure, $LiTi_2(PO_4)_3$-like phase (COD card 96-722-2156), was detected in all the LCGTP glass-ceramics. Other diffraction peaks were also indexed as minority phase corresponding to $LiCrP_2O_7$-type compound

(COD card 96-221-2724). Note that the assigned diffraction peaks pertaining to this phase are more intense in series with higher chromium content (Figure 5.14). Moreover, the 2θ angle of diffraction peaks corresponding to NASICON-type structures shifts as germanium content increases, due to changes in interplanar spaces (d). In fact, a progressive shift of the most intense diffraction peak towards higher 2θ is visible in a comparison of all XRD patterns (see guideline, Figure 5.14).

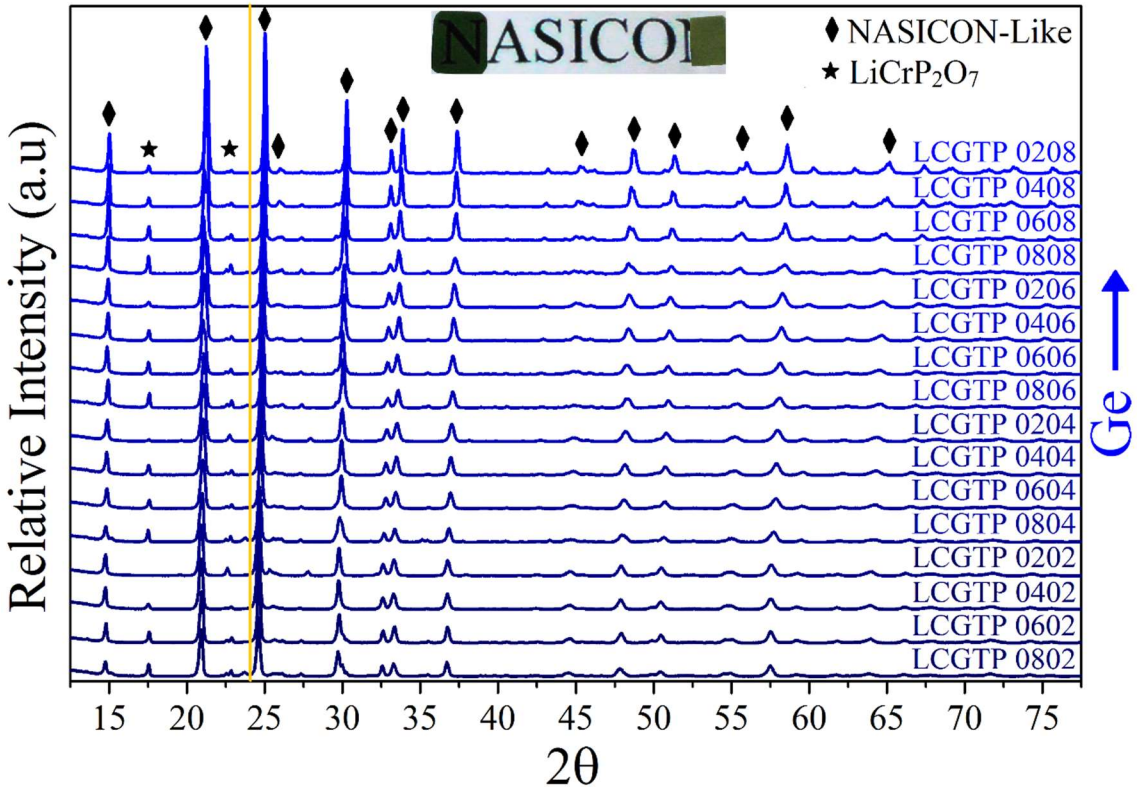

Figure 5.14 - XRD patterns of the sixteen LCGTP glass-ceramics obtained by heat-treating the precursor glass for 2 hours at 900ºC.

Figure 5.15 shows the most intense diffraction peak (2θ ~ 25 °) of twelve LCGTP glass-ceramics. In the 0.2 x series (Figure 5.15a), the increase in y (proportional to Ge content) causes the diffraction peak to shift to higher angles. Based on Bragg's law (n.λ=2.d.sinθ), this shift indicates smaller interplanar distances. These results are in perfect agreement with the previous assumption, which justified the investigation of the LCGTP system. As Ge^{+4} has a smaller crystal radius (0.0670 nm) than Ti^{+4} (0.0745 nm) [84], the substitution of Ti^{+4} by

Ge^{+4} in this series leads to a smaller interplanar spacing. The same applies to the 0.8 x series (Figure 5.15b), albeit with smaller shifts, since the effective Ge content here is lower because x is higher (Ge=[y(2-x)]).

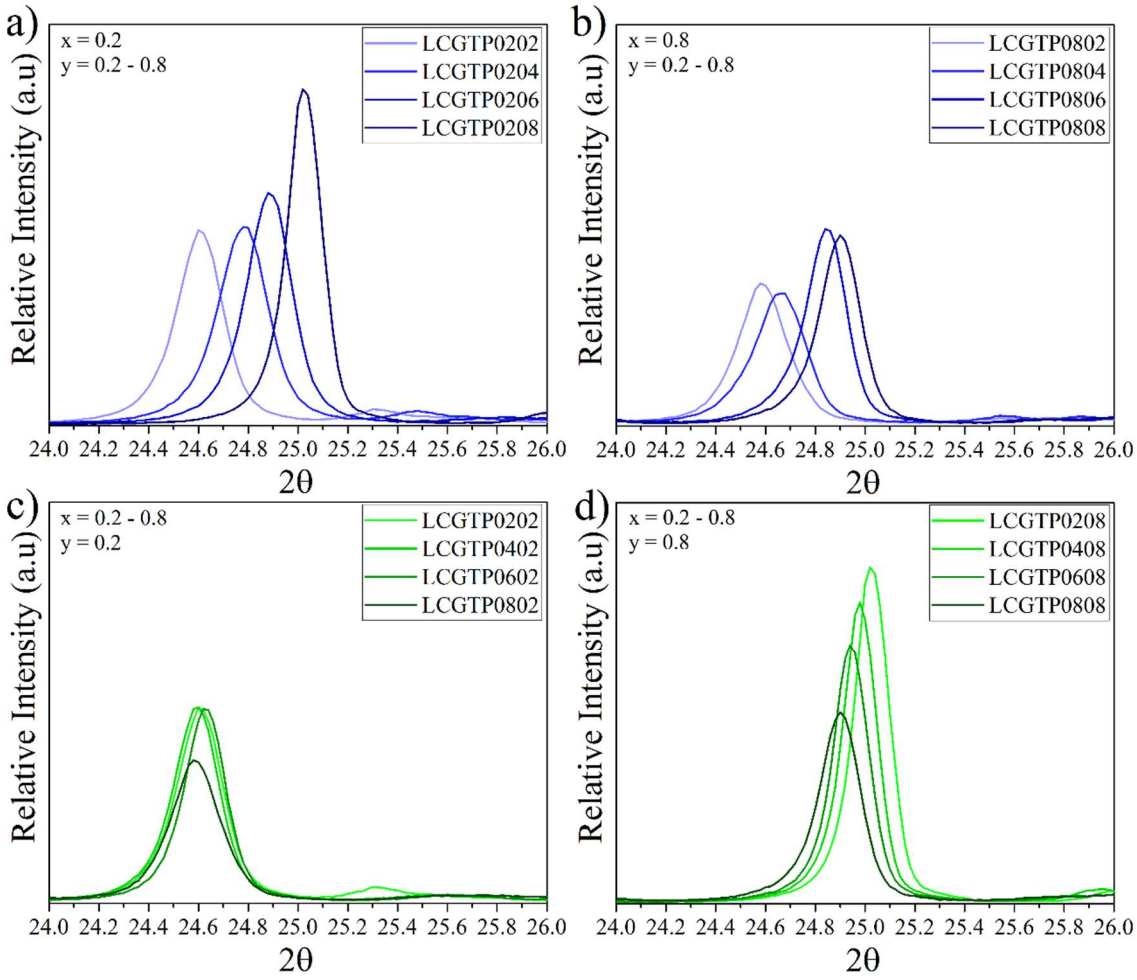

Figure 5.15 - Dependence of the most intense diffraction peak position on x (Cr content) or y (proportional to Ge content) of different LCGTP glass-ceramics series, namely, 0.2 x series (a), 0.8 x series (b), 0.2 y series (c) 0.8 y series (d).

On the other hand, when the 0.2 y series is analyzed as a function of x (Cr content), the shift is almost imperceptible (Figure 5.15c). As the Ge content in this series is low, Cr (0.0755 nm) replaces mostly Ti (0.0745 nm), and no shift is visible because their crystal radius has roughly the same size [84]. Conversely, if the Ge content is high, like in the 0.8 y series (Figure 5.15d), an increase in Cr content shifts the most intense diffraction peak to lower 2θ angles. This increment

in the interplanar spacing can be explained based on the crystal radius of Cr^{+3} (0.0755 nm) which is larger than that of Ge^{+4} (0.0670 nm).

As we have shown before, the lattice parameters and unit cell volume of NASICON-type structures can be estimated based on the diffraction angle of its atomic planes, using Eq. 3.1 and Eq. 3.2, respectively. Indeed, it is possible to determine *a* and *c* parameters by knowing the diffraction angle of only two atomic planes. Even though, here we chose to use a fitting tool called *"profile matching with constant scale factor",* available in Full Prof Suite software. This fitting tool uses all reflections generated from the space group which confers better accuracy to the analysis. In addition to the cell parameters, also zero shift and Caglioti's coefficients were refined. A second phase (space group P 12_11, monoclinic system) corresponding to the $LiCrP_2O_7$ compound has also been added to get a more reliable fitting. For all sixteen glass-ceramics, the agreement between experimental and calculated XRD pattern are reasonably good, with χ^2 lower than 7 and Bragg R-Factor for the NASICON-like phase lower than 0.5. Figure 5.16 shows experimental and calculated XRD pattern of glass-ceramic sample LCGTP0602.

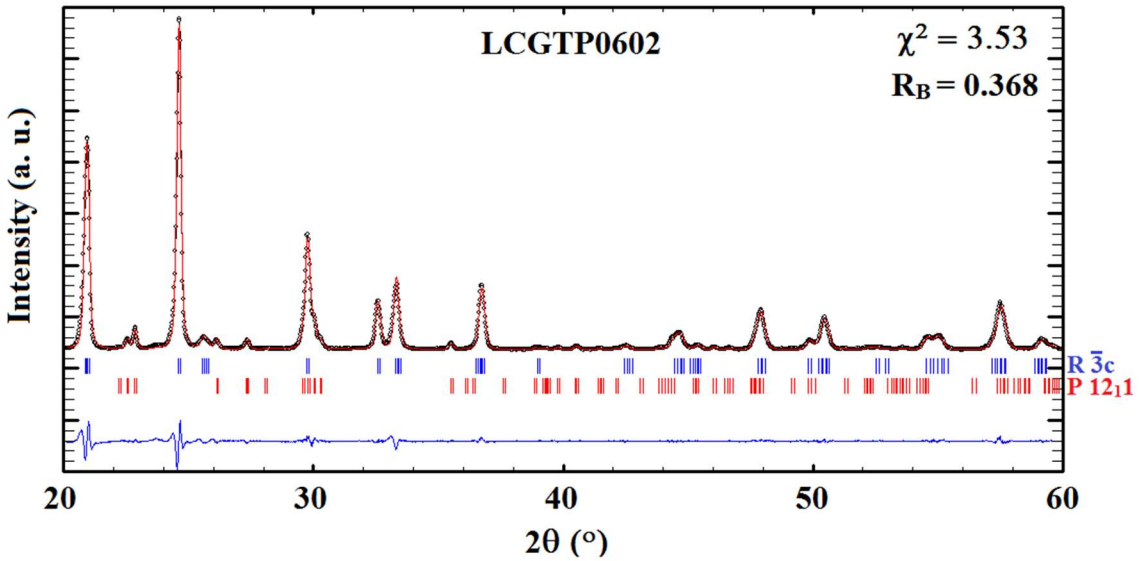

Figure 5.16 - Experimental (black circles) and calculated (red line) XRD patterns of LCGTP0602 glass-ceramics. The difference pattern is shown below (blue line), vertical bars show calculated Bragg reflection positions for the spaces groups R$\bar{3}$c (blue) and P 12_11 (red).

Figure 5.17 illustrates the dependence of the unit cell volume of NASICON-type structure on x and y. An analysis of the unit cell volume in the 3D plot in Figure 5.17a indicates that the unit cell volume decreases when y increases in every x series. As stated earlier, this effect is smaller in the 0.8 x than in the 0.2 x series because the effective Ge content (y[2-x]) is lower in the first. In the case of Cr content, the increase in x causes practically no change in the unit cell volume of the 0.2 y series, but significantly increases the volume in the 0.8 y series. To gain a clear understanding of how the unit cell volume of NASICON-type structure changes with Cr and Ge content, we have also plotted the unit cell volume as a function of the effective Ge content. Moreover, its respective difference is also plotted (Cr plus Ti content) since Cr^{+3} and Ti^{+4} have comparable crystal radii (Figure 5.17b). Note that the sum of Cr, Ge and Ti is always 2 because of the proportion of the octahedral site in the LCGTP system. Pearson's correlation coefficient (r) shows a negative dependence (r_{Ge} = -0.991) of the unit cell volume on the effective Ge content (y[2-x]). Hence, the enhancement of Ge content indeed decreases the unit cell volume. Consequently, the correlation coefficient between the unit cell volume and Cr plus Ti content (x+[1-y][2-x]) is the same, but positive (r_{Ti+Cr} = +0.991).

Moreover, the intercepts where Ge content (1.314±0.002nm^3) and Cr plus Ti content (1.198±0.004nm^3) are zero, match fairly well with the unit cell volume of $LiTi_2(PO_4)_3$ (1.310nm^3) and $LiGe_2(PO_4)_3$ (1.207nm^3) [78], respectively. Therefore, notwithstanding some spurious phases, it is highly likely that Ge, Ti, and Cr share the octahedral sites of NASICON-type structures in all the LCGTP compositions. In summary, these results are consistent with our previous prediction that the lattice parameters and unit cell volume of the proposed $Li_{1+x}Cr_x(Ge_yTi_{1-y})_{2-x}(PO_4)_3$ system could be tailored by means of compositional design. Additionally, the unit cell volume of LCGTP glass-ceramics of the 0.2 y series is only slightly lower (1.290-1.300nm^3) than that of $LiTi_2(PO_4)_3$ (1.310 nm^3).

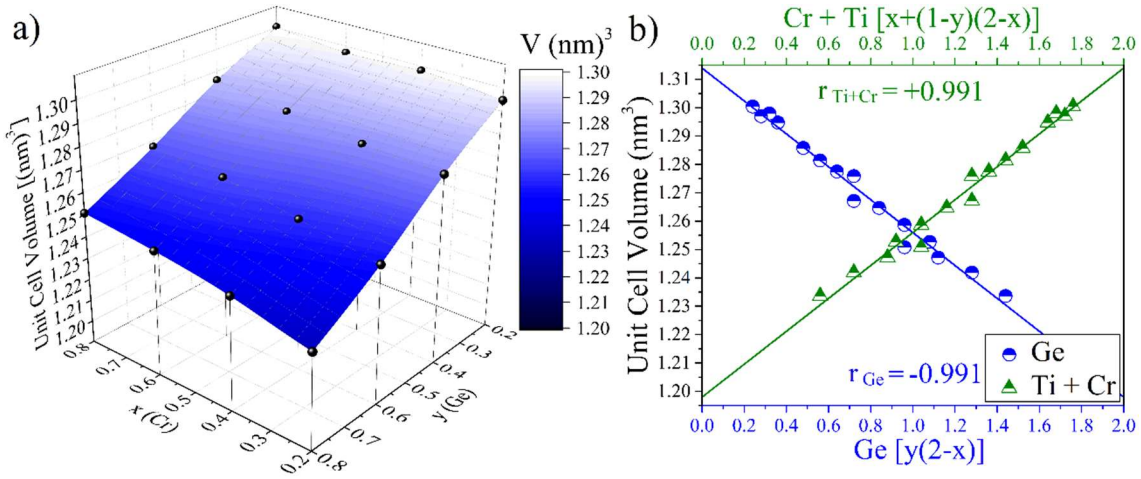

Figure 5.17 - Dependence of the unit cell volume of NASICON-type structure on: (a) x (Cr content) and y (proportional to Ge content); (b) effective Ge content (y[2-x]) or Cr plus Ti (x+[1-y][2-x]) content.

5.2.4 Electrical Characterization of LCGTP glass-ceramics

We have analyzed the sixteen LCGTP glass-ceramics by electrochemical impedance spectroscopy (EIS) at six different temperatures, making a total of 96 measurements. Again, in every case, the EIS analysis reveals the typical behavior of an ionic conductive electrolyte (see Figure 5.18) [48,56,57,78]. Figure 5.18 shows a representative set of data obtained from the EIS analyses of LCGTP glass-ceramics. As we have done previously, the complex impedance (Z*) plots have been normalized by the shape factor of each sample to obtain the specific impedance (Z_S*). In general, the complex impedance of all LCGTP glass-ceramics has exhibited the same electrical behavior with three distinct contributions, namely, grain, grain boundary and electrode polarization. Although the frequency range in which they are observed has varied since the resistivity of LCGTP glass-ceramics also varied considerably with composition.

The strong dependence of the electrical properties of LCGTP glass-ceramics on their composition can be directly observed in the specific complex impedance plots. Figure 5.18b presents Z_S* plots of LCGTP glass-ceramics of the 0.6 x series. As can be seen, while the total resistivity of the LCGTP0608 glass-ceramic (higher Ge content) is higher than 35kΩ.cm (Figure 5.18b), that of the other glass-ceramics of the 0.6 x series is lower than 10kΩ.cm (Figure 5.18b,

10X zoom). Moreover, the grain resistivity of the LCGTP0608 is in the same order of magnitude as the total resistivity of the other glass-ceramics Figure 5.18b, 10X zoom). In contrast, the LCGTP0602 glass-ceramic has presented the lowest resistivity (about 3 kΩ.cm) at RT (300K) among all the LCGTP glass-ceramics studied here. As the temperature of measurement is increased the resistivity of the samples decreases. Figure 5.18c shows Z_S* plots of LCGTP0602 glass-ceramics measured at six different temperatures. As the theory predicts, the decrease in resistivity as a function of temperature is not linear but logarithmic.

To properly separate and quantify grain and grain boundary contributions, the impedance data are fitted with the same equivalent circuit presented in section 5.1.4. Figure 5.18a shows the resulting fit obtained for the impedance data of sample LCGTP0602. The goodness of fit is remarkably high (χ^2=0.0006, in this case) indicating that the chosen equivalent circuit can describe very well the impedance data. We extrapolated the fit to a frequency (10GHz) out of the measured frequency range just to show the grain contribution, which agrees very well with the high-frequency experimental data where the grain contribution is significant. The grain contribution becomes more obvious in the analysis of more resistive samples such is the case of the LCGTP0608 sample (Figure 5.18b, 10X zoom). The results of fitting of grain capacitance (C_g) at 300K of all the LCGTP glass-ceramics range from $2.5x10^{-12}$ to $1.5x10^{-11}$F. As for grain boundary, capacitance (C_{gb}), which has been determined using equation Eq. 5.2 [24,48,79], are found to range from $3.2x10^{-11}$ to $3.0x10^{-10}$ F, while the parameter n_{gb} are fitted between 0.46-0.81. All the results of fitting are reasonable for polycrystalline ionic conductors [25], demonstrating that the equivalent circuit employed here can provide a good description of the electrical behavior of the investigated electrolytes.

The grain and grain boundary contribution to the ionic conductivity, as well as the total ionic conductivity of LCGTP glass-ceramics, were determined by applying the relation $\sigma = 1/\rho$ to the values obtained by fitting, R_g, R_{gb} and $R_g + R_{gb}$, respectively. As the impedance data have previously been normalized by the sample's shape factor, the values obtained by fitting indicate the resistivities (ρ).

However, only their apparent contribution can be estimated based on the shape factor of the entire sample.

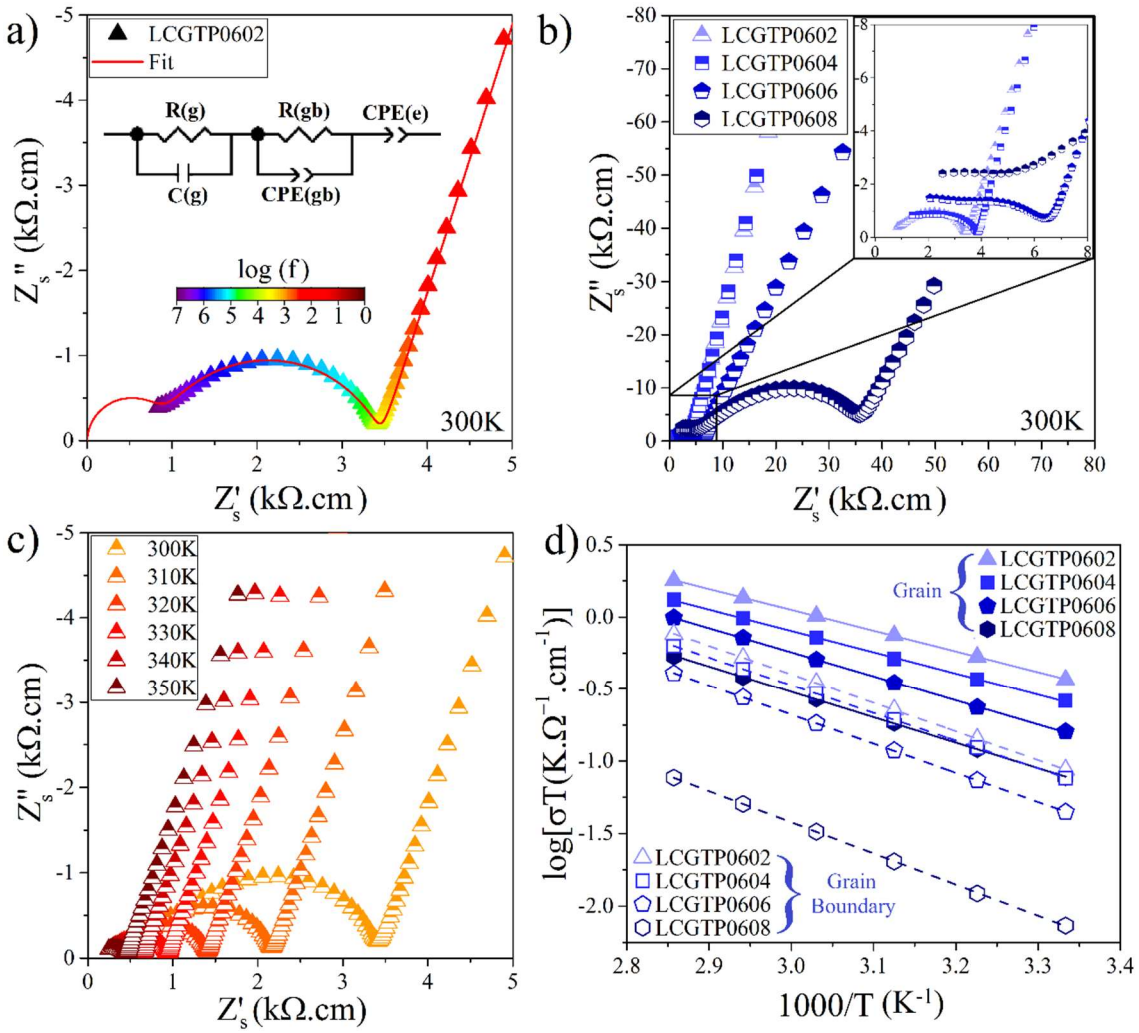

Figure 5.18 - Set of EIS analyses of LCGTP glass-ceramics represented by: (a) A Fit of impedance data of the LCGTP0602 glass-ceramic recorded at 300K, based on the indicated equivalent circuit; (b) Z_S^* plots at 300K of the LCGTP glass-ceramics of the 0.6 x series; (c) Z_S^* plots of LCGTP0602 at different temperatures; (d) Arrhenius plots of apparent conductivity at the grain and grain boundary of LCGTP glass-ceramics of the 0.6 x series.

The dependence of ionic conductivity on the inverse of temperature has been plotted following the Arrhenius-like relation expressed in Eq. 2.5 [6]. Arrhenius-like plots of grain (σ_g) and grain boundary (σ_{gb}) apparent contribution of ionic conductivity for LCGTP glass-ceramics of the 0.6 x series are shown in

Figure 5.18d. Both grain and grain boundary apparent contribution present an Arrhenius behavior. Figure 5.18d clearly shows that the grain apparent conductivity of LCGTP0602 is higher than that of LCGTP0608. The grain boundary apparent conductivity of LCGTP0602 is even higher than the grain apparent conductivity of LCGTP0608 glass-ceramics. Thus, the increase of Ge content seems to impair both grain and grain boundary conductivities. Indeed, this behavior generally has prevailed throughout the entire LCGTP glass-ceramic system.

Figure 5.19 shows the dependence of total ionic conductivity at 300K on x and y, as well as the grain and grain boundary apparent contribution. As can be readily seen in Figure 5.19a, an increase in y (proportional to Ge content) decreases the total ionic conductivity of every x series. On the other hand, looking at the y series, the enhancement of x (Cr content) seems to increase the total ionic conductivity up to a certain limit (x = 0.6). After this point, the enhancement of Cr content decreases the total ionic conductivity of every y series. The highest total ionic at RT conductivity is found to be $2.9x10^{-4}\Omega^{-1}.cm^{-1}$ ($\log[\sigma_t] = -3.53$) for the LCGTP0602 glass-ceramic. Half of all the LCGTP glass-ceramics, namely, LCGTP0402, LCGTP0404, LCGTP0602, LCGTP0604, LCGTP0606, LCGTP0802, LCGTP0804 and LCGTP0806, have presented a total conductivity higher than $10^{-4}\Omega^{-1}.cm^{-1}$ at 300K.

One can also see that the tendency and magnitude of total ionic conductivity is mostly limited by the grain boundary apparent contribution (Figure 5.19c). However, special attention should focus on the apparent grain contribution, which is higher than $10^{-3}\Omega^{-1}.cm^{-1}$ in the LCGTP glass-ceramics of the 0.2 y series (Figure 5.19b). The apparent grain conductivity decreases in response to increasing y in every x series. On the other hand, increasing x does not change the apparent grain conductivity of the 0.2 and 0.4 y series substantially, but increases it sharply in the 0.6 and 0.8 y series.

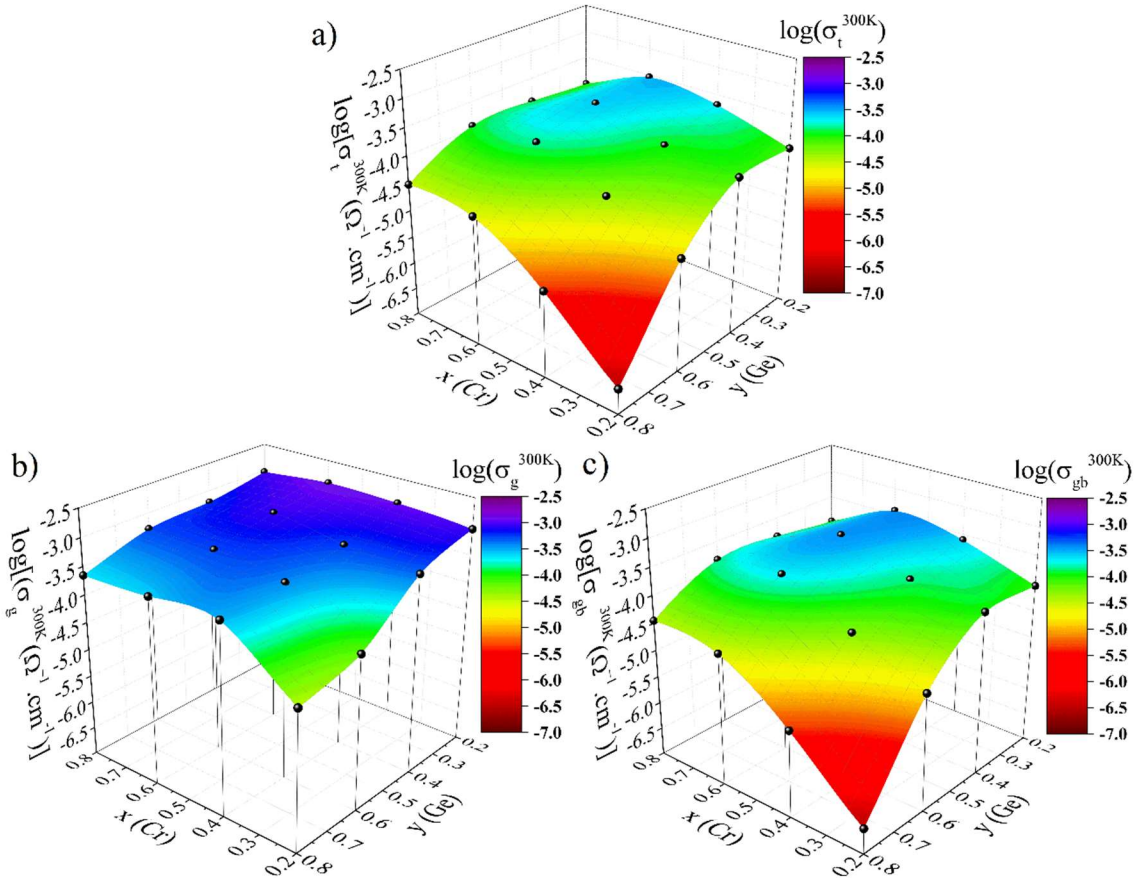

Figure 5.19 - Dependence of room temperature ionic conductivity (300K) on x (Cr content) and y (proportional to Ge content), for glass-ceramics of the $Li_{1+x}Cr_x(Ge_yTi_{1-y})_{2-x}(PO_4)_3$ system in the following contributions: (a) total; (b) grain; (c) grain boundary.

The activation energy for ionic conductivity of grain and grain boundary apparent contributions has been calculated for all the LCGTP glass-ceramics using Eq. 2.5. Figure 5.20 shows the dependence of activation energy related to grain contribution ($E_a'_g$) as a function of x and y, as well as the effective Ge content ([y(2-x]). The increment of y causes an increase in $E_a'_g$ in every x series, while the increment of x does not show a regular tendency, exhibiting a different trend for each y series (Figure 5.20a). Nonetheless, the 0.2 y series, which presents apparent grain conductivity higher than 10^{-3}, shows the lowest $E_a'_g$ (<0.27 eV). Additionally, 10 of the 16 LCGTP glass-ceramics present $E_a'_g$ lower than 0.30 eV.

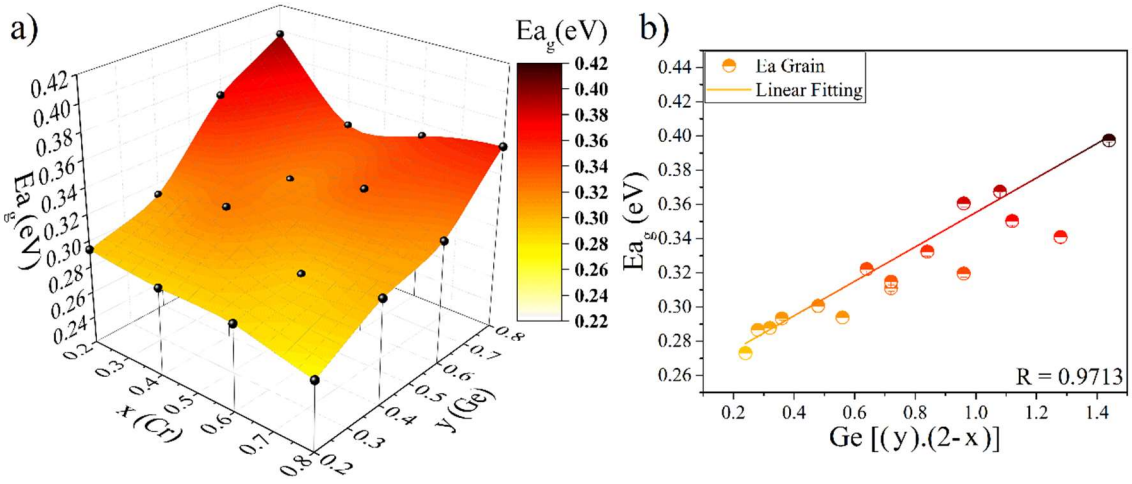

Figure 5.20 - Dependence of grain contribution-related activation energy ($E_a'_g$) on: (a) x (Cr content) and y (proportional to Ge content); (b) effective Ge content ([y(2-x]).

As we have previously done with the unit cell volume in section 5.2.3, the correlation between effective Ge content and $E_a'_g$ for all the LCGTP glass-ceramics has also been evaluated based on Pearson's coefficient (r) (Figure 5.20b). Here, we find a positive and significant correlation (0.9713), indicating that the Ge content causes structural changes that hamper the movement of lithium ions in NASICON-type structure. Considering the negative correlation (-0.991) between Ge content and unit cell volume shown in the previous section, we can safely infer that there is also a correlation between the unit cell volume and $E_a'_g$, in which an increase in the unit cell volume tends to cause a decrease in $E_a'_g$.

The relationship between unit cell volume and activation energy for ion conduction has already been reported for other systems. However, this reported correlation contemplates a broad range of cell volumes with only tetravalent cations (Ge, Ti, and Hf) and suggests an optimum volume to a lower $E_a'_g$ [37]. In this study, we extended this investigation also considering a trivalent cation (Cr^{+3}), but we use a narrower range of cell volumes. However, notwithstanding the correlation we found, another structural issue other than just the cell volume may play a role in the $E_a'_g$ since there is a considerable dispersion in $E_a'_g$ data. As for the pre-exponential term, the values pertaining to grain contribution

($\log(\sigma_0'_g)$) ranges from 4.0 to 4.9. These values are in accordance with the one ($\log(\sigma_0'_g) = 4.3$) estimated using the expression $\sigma_0'_g = n_0.Ze^2.v.\lambda^2/k_B$, where the entropic term ($e^{[(\Delta Sm+\Delta Sf/2)/kB]}$) is neglected, n_0 is the concentration of the mobile species (~10^{22}ions/cm^3), Ze is the charge associated to the mobile species ($1.6x10^{-19}$C), λ is the jump distance (λ~$1x10^{-8}$cm) and v is the attempt frequency (v=10^{13}Hz) [1,6,10,13].

Values of activation energy ($E_a'_{gb}$) and log pre-exponential term ($\log(\sigma_0'_{gb})$) related to grain boundary contribution are identified, ranging from 0.36 to 0.49 eV and from 3.8 to 6.5, respectively. In the case of $E_a'_{gb}$, no significative correlation relating to Ge content ($r < 0.05$) has been found. In the case of the LCGTP0602 glass-ceramic, which exhibited the highest grain boundary conductivity, $E_a'_{gb}$ is found to be 0.42 eV and $\log(\sigma_0'_{gb})$ is at the upper limit ($\log(\sigma_0'_{gb}) = 6.5$). Although it is tempting to attribute the high grain boundary conductivity of the LCGTP0602 sample to its high $\log(\sigma_0'_{gb})$ value, it should be kept in mind that the grain boundary conductivity calculated here is based on the shape factor of the whole sample. Therefore, the grain boundary conductivity calculated here is merely the apparent grain boundary conductivity, thus precluding an in-depth discussion of the differences found in the $\log(\sigma_0'_{gb})$ term [48]. The real shape factor of the grain boundary depends on the microstructure of the glass-ceramics. In this regard, the reason why some glass-ceramics of this system present higher grain boundary conductivities than others is still unknown, but the microstructure and spurious phase should play a significant role. However, since this issue falls outside the scope of this study, we consider it an open question for further investigation.

5.3 Electrochemical Stability Window of LCGTP Glass-ceramics

5.3.1 Two-electrode setup electrochemical impedance spectroscopy

The stability of the Li/electrolyte interface was ascertained from EIS analyses using a symmetric Li/Sample/Li assembly. Figure 5.21 shows the evolution of the impedance response of LCGTP0606 (a) and LAGP (b) glass-ceramics over time. Two distinct contributions are clearly visible in both cases, namely, a high-frequency semicircle related to the sample's impedance and a low-frequency semicircle associated with Li transfer at the Li/electrolyte interface,

in contrast to ionic polarization at the electrode when the Au/sample/Au assembly was used in sections 5.1.4 and 5.2.4. Note that the interface impedance increases continuously over time, indicating that both glass-ceramics are unstable against lithium. This contradicts the widespread idea that LAGP electrolytes are stable against lithium because Ge and Al have relatively stable oxidation states [36,58,62].

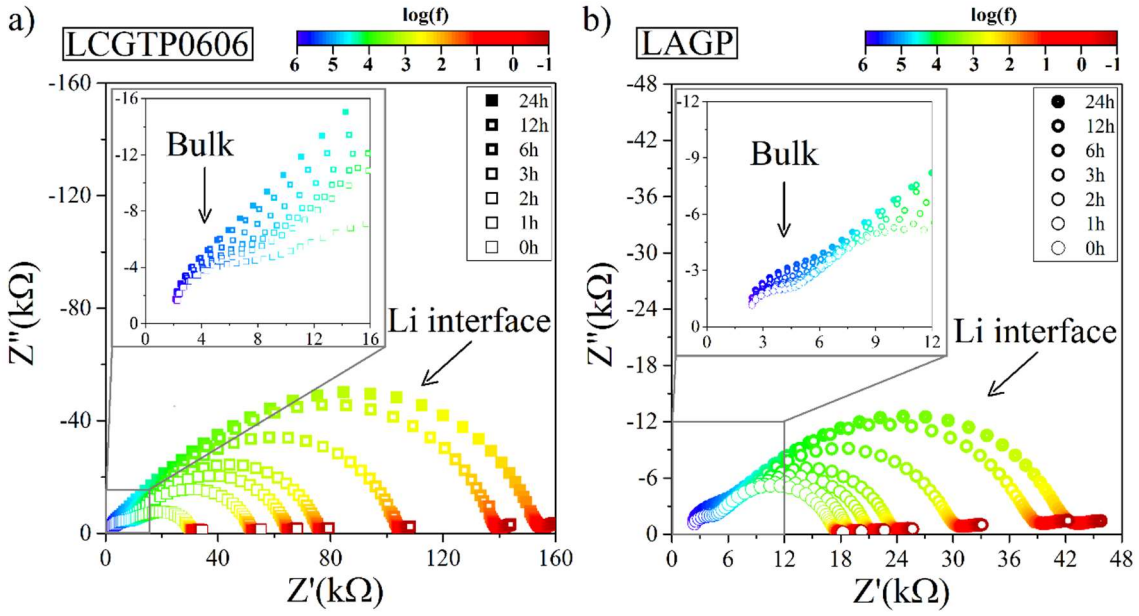

Figure 5.21 - Complex impedance data of LCGTP0606 (a) and LAGP (b) glass-ceramic samples recorded over time using a symmetric cell assembly (Li/Sample/Li). Measurements were taken in an Ar-filled glovebox, in a frequency range of 1MHz to 100mHz, using a RMS amplitude of 100mV.

Recently, a bright investigation based on EIS measurements and XPS analyses of Li-coated NASICON compounds also yielded similar results, demonstrating the instability of LAGP when in contact with Li metal [85]. In quantitative terms, the LAGP (Figure 5.21b) glass-ceramic appeared to be more stable than the LCGTP0606 (Figure 5.21a) since the increase in total impedance after 24 h is about twice for the LAGP glass-ceramic and four times for the LCGTP0606 glass-ceramic. Others LCGTP glass-ceramics have also been tested and present a similar behavior, with 3 to 5 times higher impedance after 24 h compared to the initial impedance. Therefore, the investigation of the

electrochemical stability of these electrolytes using Li metal as a reference and/or counter electrode is probably unfeasible.

5.3.2 Three-electrode setup cyclic voltammetry

Since the electrolytes were demonstrably unstable against lithium, an Ag3SI/Ag mixture was used as a reference electrode and Au as counter and working electrodes. The use of this assembly has proved to be satisfactory for several types of lithium electrolytes despite the junction potential that appears when Ag_3SI (Ag+ conducting) and lithium electrolytes (Li+ conducting) are placed in contact [65,86]. This junction potential is a result of ionic exchange (Li^+-Ag^+) between Ag_3SI and the lithium ion-conducting electrolyte, and it is an irreversible and time dependent process. Nevertheless, the interfacial layer composition changes very sluggishly with time, and this junction potential can be considered stable. Strictly speaking, since it is not a true equilibrium potential, the Ag/Ag_3SI electrode is qualified as a comparison rather than a reference electrode. However, if the time dependence of the junction potential is imperceptible in the CV experiment time-scale, the voltammetry curves will be reproducible and with a fixed potential shift [86]. In this context, an open circuit potential of around 0.4 V was found between the working and reference outputs when the samples were placed in the cell in contact with Ag_3SI/Ag electrode. Therefore, although Ag_3SI/Ag is not a true reference electrode, it will hereinafter be referred to as such for simplicity.

The first CV measurements were taken under different atmospheric conditions while the other experimental parameters were maintained. Figure 5.22 shows cyclic voltammograms of the LCGTP0402 glass-ceramic sample carried out in air (Figure 5.22a) and vacuum (Figure 5.22b). A comparison of the curves shows a markedly different behavior, but with a few characteristics in common. Starting from the open circuit potential at around 0.4 V vs. Ag_3SI/Ag (identified by a cross) and sweeping to anodic potentials, the current density increases by around 2.5 V vs. Ag_3SI/Ag in the first cycle in both atmospheres, although these increases in current density have noticeably quantitative dissimilarities. In the cathodic sweep, reduction peaks at about -1 V vs. Ag_3SI/Ag and -3V vs. Ag_3SI/Ag

also seem to be in the same position in both cases. Two others oxidation current peaks are visible in the anodic sweep when the first cycle is complete, although they are located at different potentials under vacuum and air conditions.

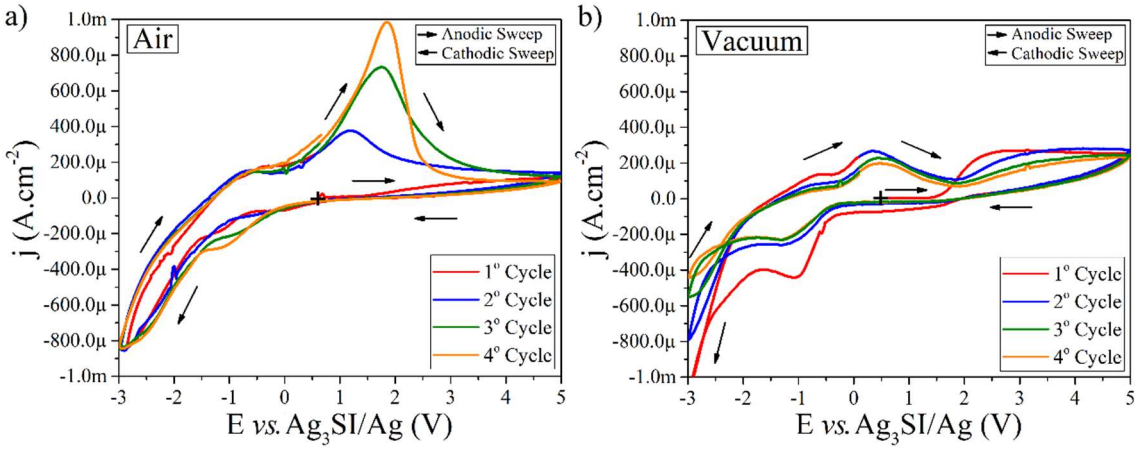

Figure 5.22 - Cyclic voltammograms of the LCGTP0402 glass-ceramic sample in air (a) and vacuum (b) atmospheres. The electrochemical window and scan rate were set at -3 V to 5 V vs. Ag_3SI/Ag and 100 $mV \cdot s^{-1}$, respectively.

The additional subsequent cycles are practically the same in the vacuum condition, albeit with a decline in the magnitude of the peak current density. However, in the air condition, the current peak at 0.5 V vs. Ag_3SI/Ag keeps increasing and shifting to higher potentials as the number of cycle increases. This behavior has also been reported by Kone et al. [86], who took CV measurements of lithium silicate glasses and attributed this peak current to the reoxidation of lithium by traces of water. Due to the magnitude of current density and broadening of this peak, it probably masks other characteristic peaks we intend to study here. Therefore, the CV analyses described from now on are performed under vacuum.

The scan rate of a CV measurement is a critical experimental parameter that must be defined to evaluate the electrochemical stability window of LCGTP glass-ceramics. High scan rates tend to overestimate the stability window of an electrolyte [86]. Figure 5.23 shows how the scan rate affects the peak potential and current density. Increasing the scan rate here causes the current density to rise, as well as the reduction peaks to shift to more reductive potentials (Figure

5.23 tag 2) and the oxidation peaks to more oxidative ones (Figure 5.23 tag 1). In liquids, those behaviors are expected, and the underlying mechanisms are well-known. In a reversible one-electron charge transfer reaction, the peak current must be proportional to the square root of the scan rate and the peak potential independent of the scan rate employed. On the other hand, in irreversible cases where the electron-transfer kinetics is limited, the peak potential is a function of the scan rate. In such cases, it is advisable to use the lowest possible scan rate, even if it causes a decrease in the magnitude of the current density.

However, as mentioned previously, there are some fundamental differences between solids and liquids regarding cyclic voltammetry analyses. For instance, in the liquid all electroactive species are relatively mobile, and an electrolyte of negligible electronic conductivity is usually chosen [3,8]. Usually in solid electrolytes, only one electroactive specie is highly mobile while the other species form a rigid framework and have very low mobility [1,10]. Consequently, if the electronic conductivity is comparable or higher than the partial ionic conductivity of the concerning specie, an electronic current is likely to flows through the solid electrolyte. Therefore, the shape of current peak curve would be governed by the electronic conductivity rather than the diffusion of the electroactive species toward the working electrode. In the present case, the electronic conductivity would proceed by a polaronic mechanism between Ti^{+4} and Ti^{+3} cations [13]. Hence, it is inadvisable to analyze the curves i = f(E) strictly on the basis of the equations commonly used for CV analyses in liquids. Nevertheless, it was chosen to use the lowest possible scan rate in order to avoid overestimation of the electrochemical window. Still, at scan rates in the order of 0.1 mV s^{-1}, it would take an entire week to scan an electrochemical window of 8V for a few cycles. Therefore, the scan rate used hereinafter to characterize the LCGTP glass-ceramic was the lowest scan rate tested (1 mV s^{-1}).

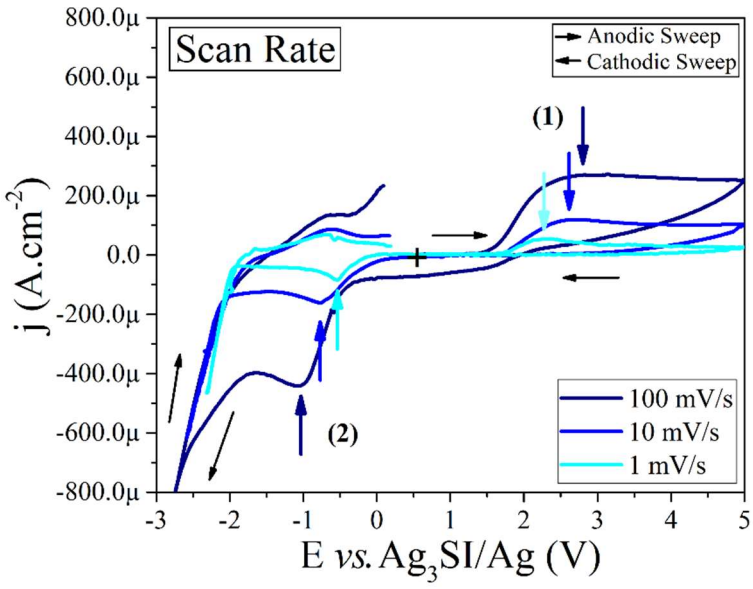

Figure 5.23 - Cyclic voltammograms of the LCGTP0402 glass-ceramic sample subjected to different scan rates (1, 10 and 100 mV s^{-1}). Measurements were taken under vacuum, and the electrochemical window was set at -3 V to 5 V vs. Ag_3SI/Ag.

The next step consisted in determining which species are reduced and oxidized when LCGTP glass-ceramics are subjected to cyclic voltammetry. Figure 5.24 shows cyclic voltammograms of LCGTP0402 glass-ceramic, and voltammograms of LAGP glass-ceramic are also presented for comparison. In Figure 5.24a, three pairs of peaks are tagged based on the rationale that redox couples should be located around the same potential. However, the chemical species oxidized at around 2 V vs. Ag_3SI/Ag (Figure 5.24a, tag 1) shows no reduction peak, indicating that this reaction is entirely irreversible. The most reasonable explanation would be oxidation of the oxygen anion (O^{-2}) from the crystal lattice, leading to gaseous O_2 (Eq. 5.3, in Kröger–Vink notations). Thus, during the anodic sweep, O_2 would be exhausted by the vacuum pump, and consequently, when the potential is swept back, the reduction of this couple is prevented or undetectable.

$$O_O^x \rightarrow \frac{1}{2}O_2(g) + V_O^{\bullet\bullet} + 2e' \qquad \text{(Eq. 5.3)}$$

As mentioned earlier, the Ag_3SI/Ag electrode in contact with LCGTP glass-ceramics presents an open circuit potential of about 0.4 V, which can be seen in

the cross marked starting potential (Figure 5.22, Figure 5.23 and Figure 5.24). Hence, the Ag_3SI/Ag potential is about 2.6 V vs. Li^+/Li electrode (+3.0 V - 0.4 V), since the Li^+/Li couple yields a potential of about -3.04 vs. SHE. This conversion places the oxidation peak at 2 V vs. Ag_3SI/Ag at a potential of 4.6 vs. Li^+/Li (2 V + 2.6 V). However, this result is inconsistent, for instance, with previously reported CV measurements of LAGP electrolytes, in which no oxidation reaction was detected up to 7 V vs. Li^+/Li [58,62]. On the other hand, it is in good agreement with computational simulations of 4.3 vs. Li^+/Li with O_2 as an equilibrium phase in the potential decomposition [87].

Using some reasonable assumptions, we can roughly estimate the thickness of the oxidized layer at the end of the first anodic sweep (Figure 5.24a, tag 1). By integrating the current density as a function of time we have found a charge density of about 100 $mC.cm^{-2}$. Then, according to the Eq.5.3 each O^{-2} oxidized releases two electrons to the working electrode. Therefore, nearly $3x10^{17}$ in an area of 1 cm^2 are oxidized according to the found charge density. The overall concentration of oxygen in the sample LCGTP0402 can be estimated based on the cell volume parameter (~1.3 nm^3) and the number of oxygen in an unit cell (72), which results in approximately $3x10^{22}$ cm^{-3}. Therefore, considering that all oxygen anions are oxidized in the layer and dividing the number of oxygen anions oxidized by the concentration of oxygen in the sample we can find a thickness of about $1x10^{-5}$ cm or 100 nm. The last assumption is not so realistic since what we should have is a diffuse concentration profile in the layer instead of an abrupt concentration profile. However, this estimation gives an idea of the order of magnitude of the layer thickness, which should be bigger than 100 nm.

In the cathodic sweep, the redox couple at around -0.5 V vs. Ag_3SI/Ag (Figure 5.24a, tag 2) may be related to Cr, Ti, or even Ge reduction, and subsequent oxidation during the subsequent anodic sweep. Since the chemical species in the LCGTP glass-ceramics are presumably in the most stable oxidation state, none of those species should be immediately excluded. As for the sudden increase in current density of around -2.5 V vs. Ag_3SI/Ag (Figure 5.24, tag 3), the reaction associated with it should be the reduction of Li^+ at the working electrode. Converting -2.5 V vs. Ag_3SI/Ag to Li^+/Li potential gives a potential of

0.1 V vs. Li^+/Li (-2.5 V + 2.6 V), which is fairly close to the expected value of 0 V considering Li metal in aqueous solution. On the other hand, when the potential is swept back, this couple reoxidizes at a much higher potential than expected (-1 V vs. Ag_3SI/Ag or 1.6 vs. Li^+/Li). This discrepancy can be explained by the tendency of Li metal to form alloys with gold [88].

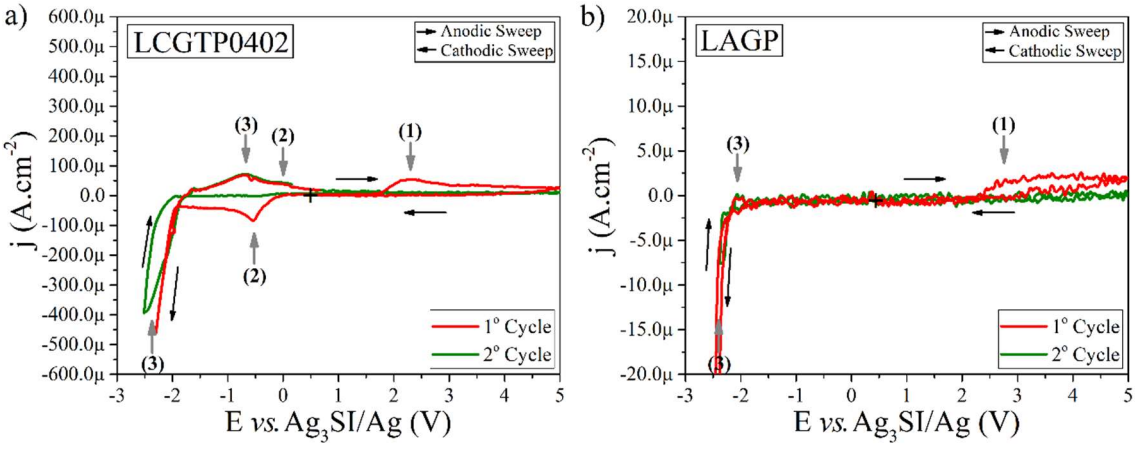

Figure 5.24 - Cyclic voltammograms of LCGTP0402 (a) and LAGP (b) glass-ceramic samples. Measurements were taken under vacuum. The electrochemical window and scan rate were set at -3 V to 5 V vs. Ag_3SI/Ag and 1 $mV \cdot s^{-1}$, respectively. Current peaks are attributed to the O-2 oxidation (1), the Ti, Cr, or Ge oxidation/reduction (2) and Li oxidation/reduction (3).

CV measurements were also taken of the well-known NASICON-structured glass-ceramic LAGP (Figure 5.24b) to unveil the chemical species behind the redox peaks marked as 2 in Figure 5.24a. In this case, current density peaks corresponding to Li^+ reduction and O^{-2} oxidation are around the same potential, despite their much smaller magnitude. These quantitative differences could be explained based on the electronic conductivity of this electrolytes. In contrast, peaks marked as 2 are absent, suggesting that Cr or Ti are responsible for this peak in LCGTP glass-ceramics. In both cases, an intriguing characteristic is that after the first cycle, both electrolytes seem to stabilize in the entire electrochemical window analyzed, since they present only reduction and oxidation signals pertaining to Li. This point will be discussed later in light of the *in situ* EIS results.

Regarding the reduction peak assigned as 2, one way to determine whether Cr or Ti is the chemical species behind it is to compare LCGTP glass-ceramics containing different concentrations of these elements. Figure 5.25 shows cyclic voltammograms under the same scan speed (1 $mV \cdot s^{-1}$) of the four LCGTP glass-ceramic studied here. Figure 5.25a shows three LCGTP glass-ceramics with the same Cr content and variable Ti content. At the peak in question (tagged as 2), the current density increases as Ti content increases (as y decreases). On the other hand, when the Ti content is fixed (y=0.2) and Cr content is varied (x= 0.4 and 0.6), the current density at the peak remains practically the same (Figure 5.25b). This finding offers preliminary evidence that the reduction peak at -0.5 V vs. Ag_3SI/Ag pertains to the reduction of Ti.

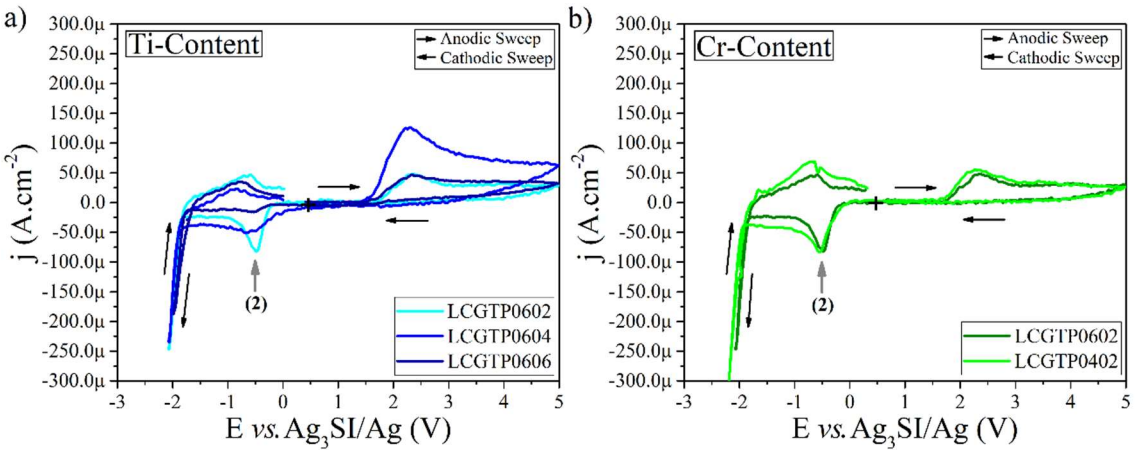

Figure 5.25 - Cyclic voltammograms of the four glass-ceramics under study, comparing the influence of Ti (a) and Cr (b) content. Measurements were taken under vacuum. The electrochemical window and scan rate were set at -3 V to 5 V vs. Ag_3SI/Ag and 1 $mV \cdot s^{-1}$, respectively.

A narrower electrochemical window was scanned around the reduction peak at -0.5 V vs. Ag_3SI/Ag (tagged as 2, Figure 5.25) in one of the LCGTP glass-ceramics (LCGTP0604) to separate the signal of this specific redox couple from the others. The result depicted in Figure 5.26 once again shows that, in the first cycle, no oxidation occurs under anodic sweep up to 1.5 V vs. Ag_3SI/Ag. When the potential is swept back, a reduction peak becomes visible a little beyond -0.5 V vs. Ag_3SI/Ag and the reoxidation of the reduced species also

occurs beyond -0.5 V in the cathodic direction (see purple strip, Figure 5.26). This process seems to be reversible in subsequent cycles. The mean potential between these peaks is still around -0.5 V vs. Ag_3SI/Ag, which converted to Li^+/Li potential, gives a potential of about 2.1 V vs. Li^+/Li (-0.5 V + 2.6 V). This mean potential of 2.1 V vs. Li^+/Li is reasonably close to that of lithium intercalation/extraction (2.5 V vs. Li^+/Li) in monoclinic lithium titanium phosphate ($Li_{1+x}Ti_2(PO_4)_3$) through the reduction/oxidation of the Ti^{+4}/Ti^{+3} couple [89]. Moreover, a decomposition potential of reduction at around 2.2 V vs. Li^+/Li for LATP was found in a computational simulation study [87]. Therefore, the reduction and oxidation peaks marked as 2 in Figure 5.25 are probably related to Ti species.

Considering the assumptions described above to estimate the thickness of the oxidized layer in anodic sweep, it is also possible to calculate here, the thickness of the reduced layer at the end of the cathodic sweep (Figure 5.26). By using the encountered charge density of about 10 $mC.cm^{-2}$, one electron transferred according to the Ti^{+4}/Ti^{+3} couple, a cell volume parameter of about 1.3 nm^3 and the number of titanium in an unit cell of approximately 5 according to the LCGTP0604 nominal composition, we have found a reduced layer of 300 nm.

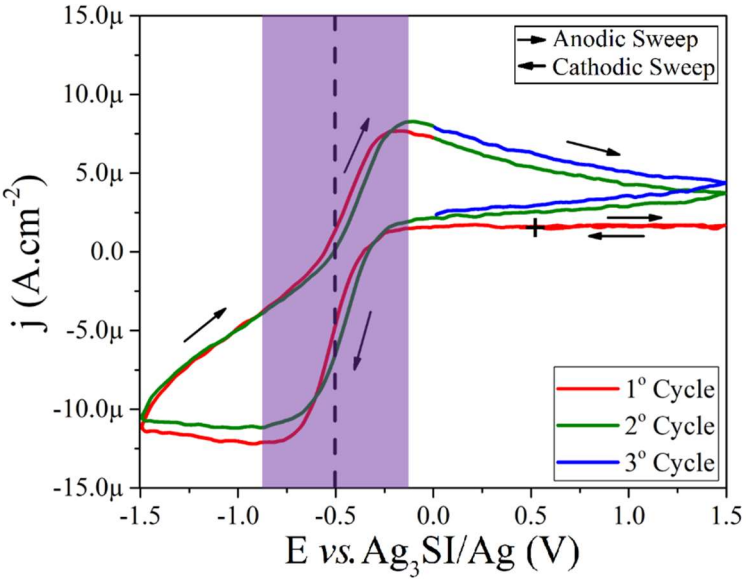

Figure 5.26 - Cyclic voltammograms of the LCGTP0604 glass-ceramic sample. Measurements were taken under vacuum. The electrochemical window and scan rate were set at -1.5 V to1.5 V vs. Ag_3SI/Ag and 1 $mV \cdot s^{-1}$, respectively.

5.3.3 Three-electrode setup electrochemical impedance spectroscopy

As shown earlier herein, after the first cycle the LCGTP glass-ceramic appeared to stabilize, presenting a much broader electrochemical stability window than in the first cycle. An innovative approach is used to follow the CV measurements by EIS *in situ* to evaluate the effect of this apparent stability on the electrical properties of LCGTP glass-ceramics. Figure 5.27 shows complex impedance plots recorded using the three-electrode cell setup before and after taking CV measurements, without moving the sample between measurements. Before the CV measurements, the electrical behavior of the LCGTP0402 glass-ceramic was similar to that found when the electrical properties of these electrolytes were evaluated using two-electrode Au/Sample/Au assembly in sections 5.1.4 and 5.2.4.

The inset plot in Figure 5.27 shows a high-frequency semicircle of a few KΩ that accounts for the LCGTP grain boundary impedance response, followed by a low-frequency straight line due to ionic polarization at the Au electrode. In contrast with the results from two-electrode Au/Sample/Au assembly showed in sections 5.1.4 and 5.2.4, the impedance response of the grains is not apparent here. Besides the different frequency range used here (1MHz-100mHz), which precludes visualization of the largest part of grain impedance response, the remaining part is probably masked by inductance effects of the electrochemical cell. Even so, the overall impedance itself suffices to evaluate the influence of oxidation and reduction reactions on the electrical properties of these electrolytes.

After the CV analyses, the impedance response of LCGTP samples changes dramatically with a mid-frequency semicircle of tens of KΩ (Figure 5.27) which overlaps the impedance response of the sample. This indicates that the apparent electrochemical stability after the first cycle is indeed caused by an electrically insulating layer which completely changes the overall electrical properties of LCGTP samples. In fact, this layer is visible to the naked eye. When the Au electrode is removed, the sample presents a very strong dark aspect in the region where the working electrode was located (inset in Figure 5.27). In

short, the sample appeared to be stable under potential cycling, but in fact, it was degraded and had lost its initial electrical properties.

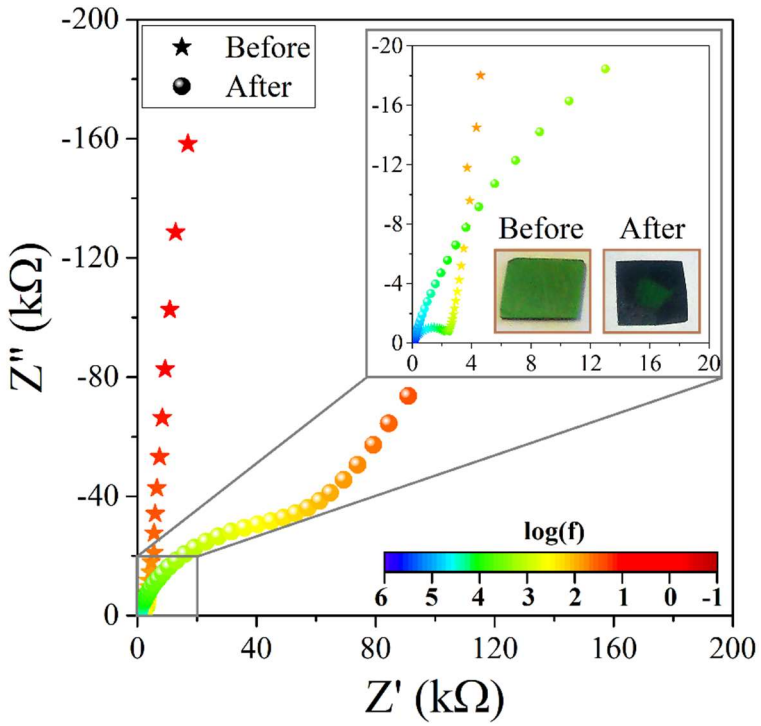

Figure 5.27 – Complex impedance data of sample LCGTP0402 recorded *in situ* using the three-electrode setup cell before (stars) and after (spheres) the cyclic voltammetry analyses shown in Figure 5.24a. Data were recorded under vacuum, in a frequency range of 1MHz to 100mHz, using a RMS amplitude of 100mV vs. Ag_3SI/Ag.

When CV measurements were taken within a narrower electrochemical window, the electrical properties of the sample are not noticeably affected. Figure 5.28 shows complex impedance plots recorded before and after taking CV measurements in an electrochemical window of -1.5 V to 1.5 V vs. Ag_3SI/Ag. As can be seen, the high-frequency impedance responses of the sample before and after the CV measurements are the same (insert plot, Figure 5.28). Also, the LCGTP0604 sample does not present a detectable color change after the CV analysis in a narrower electrochemical window.

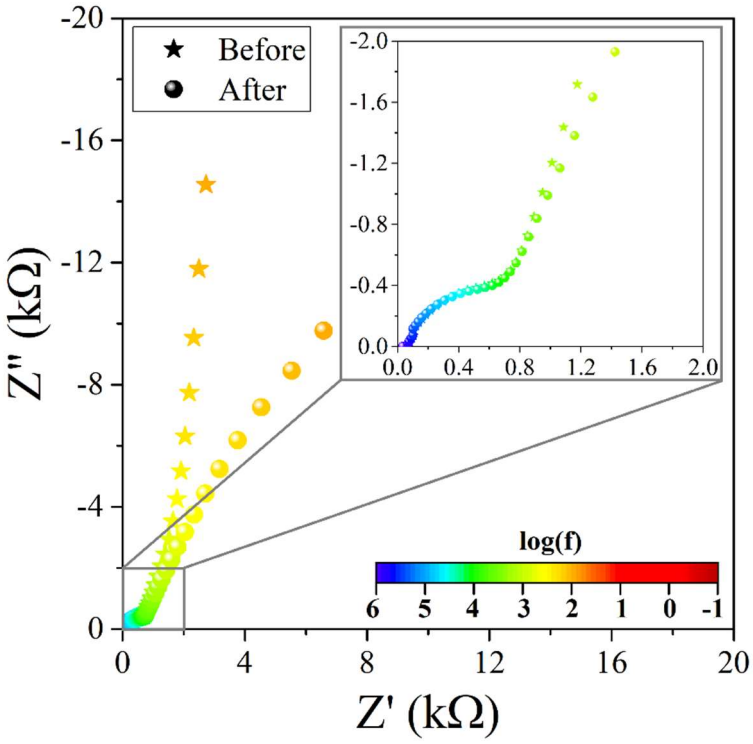

Figure 5.28 - Complex impedance data of sample LCGTP0604 recorded *in situ* using the three-electrode setup cell before (stars) and after (spheres) the cyclic voltammetry analyses shown in Figure 5.26. Measurements were taken under vacuum, in a frequency range of 1MHz to 100mHz, using a RMS amplitude of 100mV vs. Ag_3SI/Ag.

The behavior of both the LCGTP0402 and LCGTP0604 glass-ceramic samples depicted in Figure 5.27 and Figure 5.28 are similar to that of the other LCGTP glass-ceramics under study. Therefore, at anodic potentials, the electrochemical stability of LCGTP glass-ceramics was limited to potentials of 2 V vs. Ag_3SI/Ag or 4.6 V vs. Li/Li^+, while at a cathodic potential, the reduction peak at -0.5 V vs. Ag_3SI/Ag does not alter the electrical properties of these electrolyte materials.

The slight difference between the low-frequency impedance response (straight line, Figure 5.28) of the sample before and after CV measurements was examined by removing cautiously the gold electrode after the CV analyses and sputtering a new one. Figure 5.29 shows complex impedance plots recorded before, after taking CV measurements in an electrochemical window of -1.5 V to 1.5 V vs. Ag_3SI/Ag and with a new gold electrode. As a result, the new gold

electrode presents nearly the same blocking effect that of the gold electrode before CV measurements. This comparison revealed that the differences in low-frequency impedance data before and after CV measurements have to do with changes in the gold electrode, which for some reason no longer completely blocks out the Li-ions.

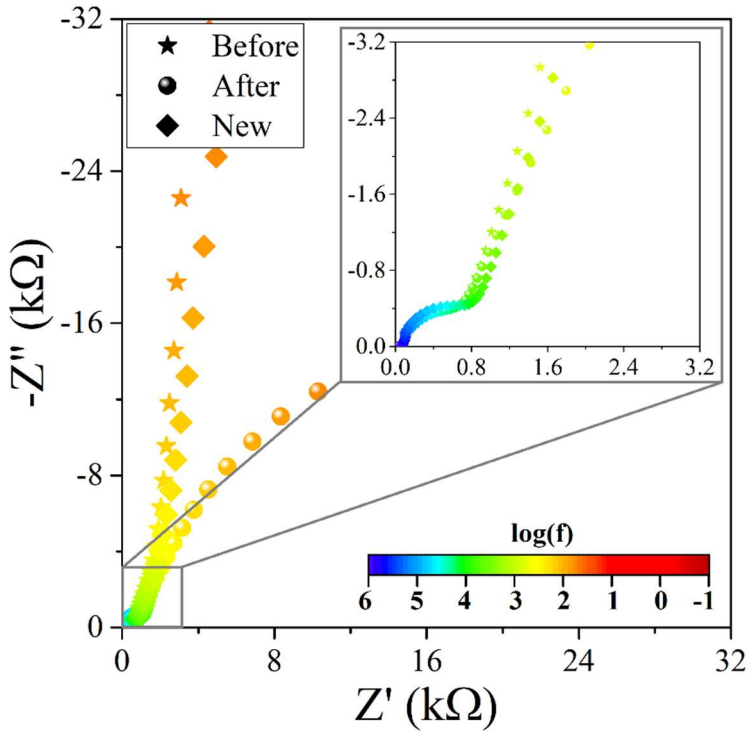

Figure 5.29 - Complex impedance data of sample LCGTP0604 recorded *in situ* using the three-electrode setup cell before (stars) and after (spheres) the cyclic voltammetry analysis shown in Figure 5.26. Additionally, after cyclic voltammetry analysis, the gold electrode was removed and replaced with a new gold electrode, after which the sample was subjected to a new EIS measurement (diamond). Measurements were taken under vacuum, in a frequency range of 1MHz to 100mHz, using an AC signal with a root mean square amplitude of 100mV vs. Ag_3SI/Ag.

5.3.4 X-ray photoelectron spectroscopy

The as-prepared samples of the four LCGTP glass-ceramics were analyzed by X-ray photoelectron spectroscopy (XPS). Figure 5.30 present high resolution XPS spectra of Cr 2p (a), Ge 3d (b), Ti 2p (c), P 2p (d) and O 1s (e) for all LCGTP

glass-ceramics under study. In general, a comparison of the four samples reveals no significant difference in the binding energies (BE) of the Cr 2p, Ge 3d, Ti 2p, P 2p and O 1s core-level electrons. BEs for these spectra lines in simple oxides are extracted from the U.S. National Institute of Standards and Technology (NIST) database and compiled in ranges of BEs in the XPS analyses presented here (Figure 5.30). Values of BE in simple oxides are usually significantly different (up to 4 eV) from those currently obtained in LCGTP glass-ceramics. To exemplify, the BE of Ti $2p_{3/2}$ in TiO_2 is 458.7 ± 0.3 eV and P 2p in P_2O_5 it is 135.4± 0.2 eV, while in the LCGTP glass-ceramic we have found BEs of about 459.8 for Ti $2p_{3/2}$ and 131.5 for P 2p. These discrepancies, which have also been found by other authors who investigate NASICON-structured compounds [85,90], can be explained by the strong inductive effect of the P-O bond that polarizes B-O bonds, increasing the ionic nature of the latter. The dashed lines indicate BE peaks of commercial LAGTP from Ohara (black line) [85] and $Li_{1+x}Cr_2(PO_4)_3$ (green line) NASICON-like phosphates [90] reported in the literature (Figure 5.30). In contrast to simple oxides, the reported BE of NASICON-type compounds matches with the results obtained here reasonably well. Based on the typical BE in NASICON-structured phosphates, the XPS results of as-prepared LCGTP samples show that the B cations are mostly in the ordinary oxidation state (Cr^{+3}, $Ti^{+4}$and Ge^{+4}). These results are in accordance with the CV results where no oxidation regarding those species is visualized in the first anodic cycle up to1.5 V vs. Ag_3SI/Ag (Figure 5.26).

Sample LCGTP0604 was also analyzed after LSV analyses to confirm the species that undergoes oxidation and/or reduction when subjected to anodic and cathodic potential sweeps. Figure 5.31 shows XPS spectra lines of Cr 2p, Ge 3d, Ti 2p, P 2p and O 1s core-level electrons of the LCGTP0604 glass-ceramic before (as a reference) and after LSV in an anodic sweep up to 5V vs. Ag_3SI/Ag and cathodic sweep up to -1.5V vs. Ag_3SI/Ag. Again, dashed lines are shown to indicate BE peaks of commercial LAGTP from Ohara (black line) [85] and $Li_{1+x}Cr_2(PO_4)_3$ (green line) NASICON-like phosphates [90]. The C 1s signal of adventitious carbon is also shown as a benchmark (grey line).

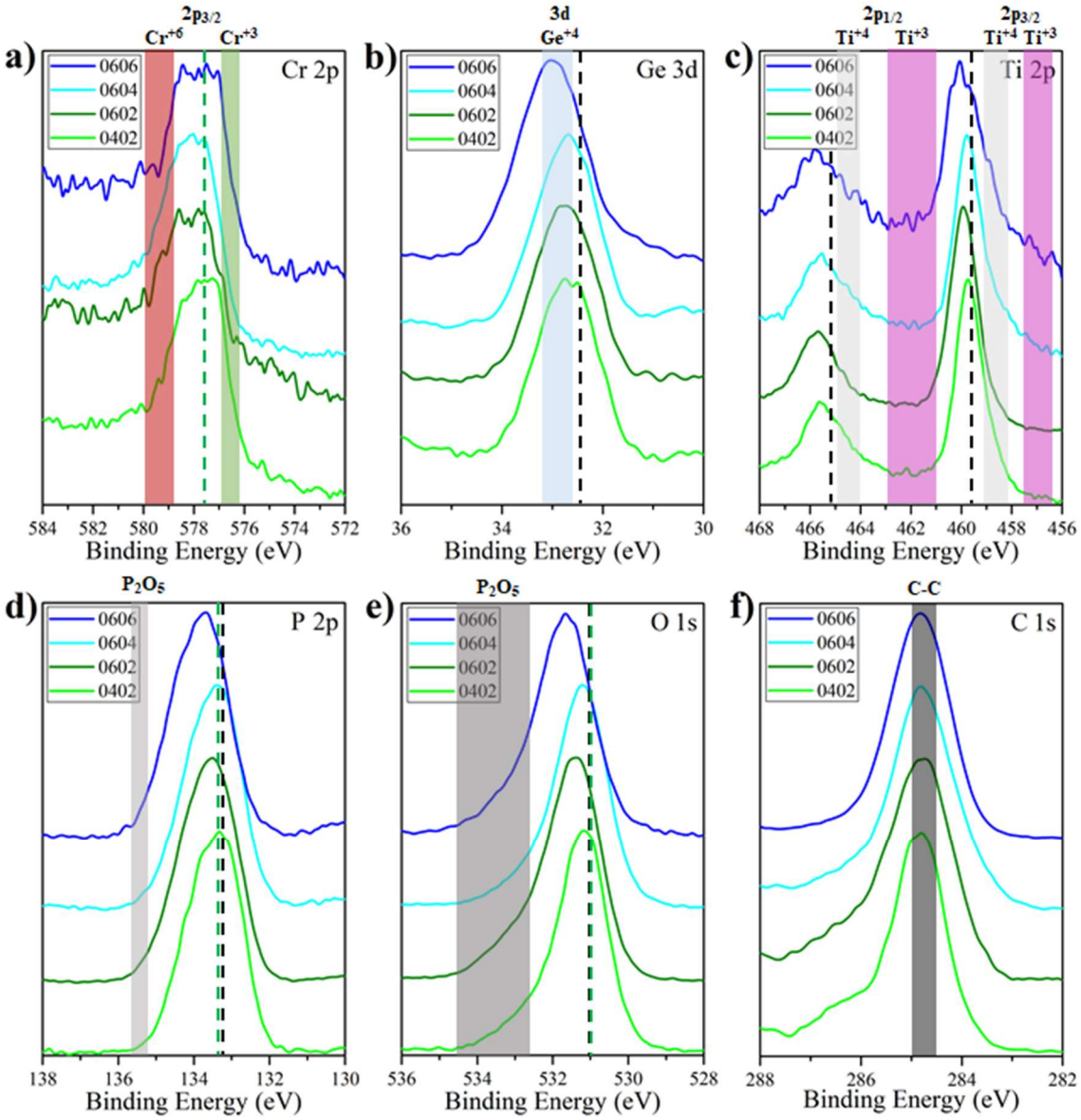

Figure 5.30 - High-resolution XPS spectra of Cr 2p (a), Ge 3d (b), Ti 2p (c), P 2p (d) and O 1s (e) for all LCGTP glass-ceramics under study. Spectrum line of C1s (f) for the C-C component resulting from adventitious carbon is also shown as a control. Note that intensities on the y-axis have been normalized to emphasize signal shapes rather than absolute intensities. Dashed lines represent BE peaks of LAGTP (black line) [24] and $Li_{1+x}Cr_2(PO_4)_3$ (green line) NASICON-type compounds [28] reported in the literature. Additionally, ranges of binding energy in oxides extracted from NIST database are shown for comparison.

As for the effect of anodic and cathodic sweeps on the BE, the spectra lines show marginal shifts in the positions of the Ge 3d (Figure 5.31b) and P 2p (Figure 5.31d) core-level electrons BE, but no significant differences in shape. On the other hand, the greatest changes in shape are found mainly in the Cr 2p, Ti 2p, and O 1s XPS spectra. The sample subjected to LSV cathodic sweep shows a broadening of Ti $2p_{1/2}$ and Ti $2p_{3/2}$ spectra lines toward lower BE (Figure 5.31c). This effect can be attributed to an increase in the Ti^{+3} concentration stemming from the reduction of Ti^{+4} under cathodic sweep. On the other hand, the LSV anodic sweep causes shape enlargement in the Cr 2p and O 1s XPS spectra toward higher BE. In the case of Cr, this must be associated with the oxidation of Cr^{+3} into species of a higher oxidation state, such as Cr^{+4} and/or Cr^{+6} (Figure 5.31a). The broadening in O 1s XPS spectra toward higher BE could be ascribed to a strong interaction in the B-O bond resulting from a higher oxidation state of the B cation. In this case, the Cr-O bond is the most likely one, since no other broadening toward high energy is visible in the sample subjected to the anodic sweep.

Another very rational explanation for this enlargement in the O 1s may be the formation of oxygen vacancies as presented in Eq. 5.3. Strictly speaking, BE of oxygen vacancies cannot be detected in XPS spectra because they have no nuclei or electrons. However, oxygen vacancies have a tendency to create a shoulder at higher binding energies. This effect was investigated by Gopel et al. [91], who created oxygen vacancies and then analyzed them by XPS. Moreover, the latter interpretation would also explain the intense dark color that appeared after LSV analyses in anodic sweeps, since the creation of oxygen vacancies introduces additional energy levels and increases the likelihood of light absorption. Finally, as mentioned previously, O_2 as an equilibrium phase in the potential decomposition (4.3 vs. Li^+/Li) has also been reported for LAGP and LATP NASICON-structured compounds in a computational simulation study [87].

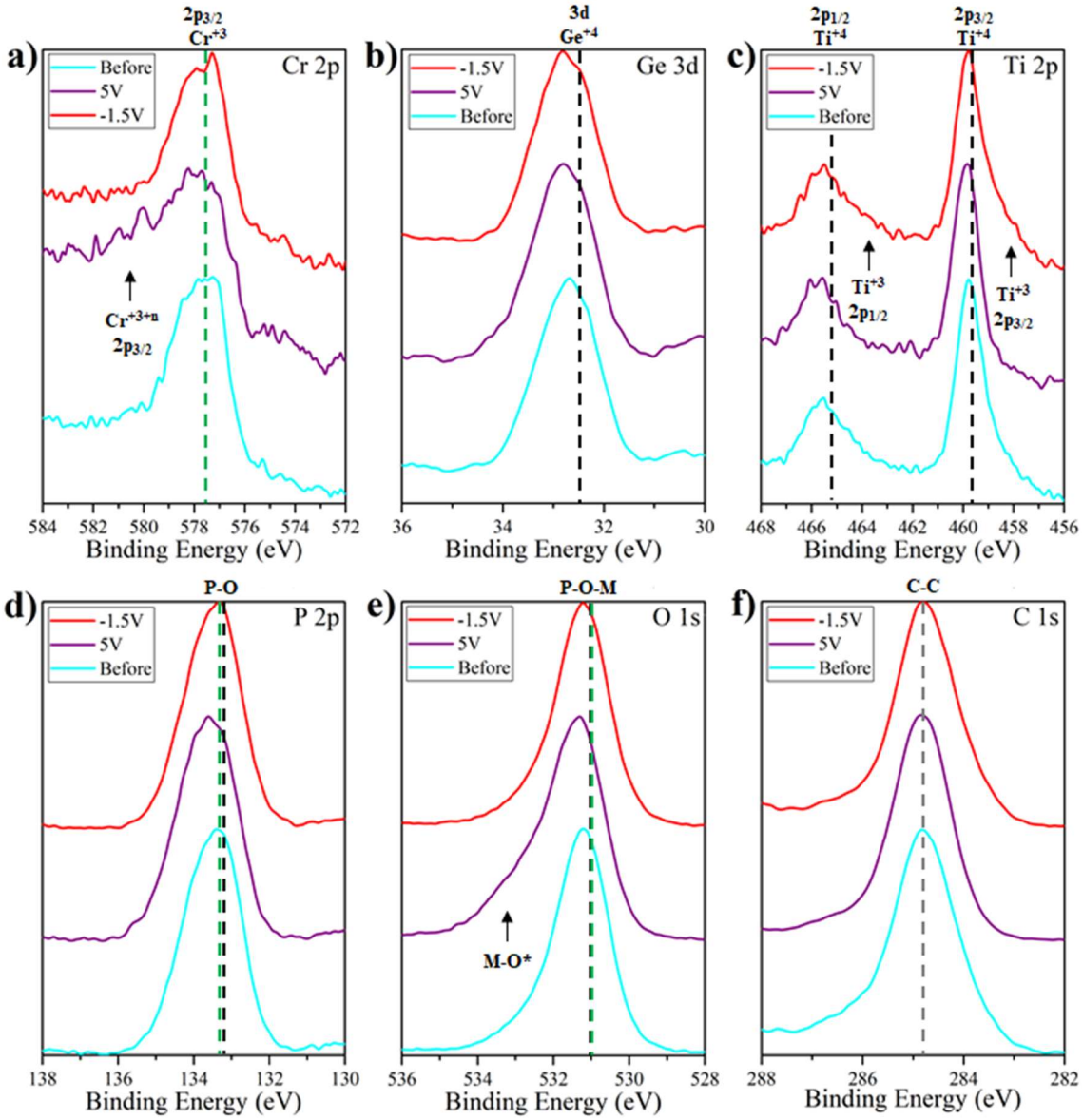

Figure 5.31 - High-resolution XPS spectra of Cr 2p (a), Ge 3d (b), Ti 2p (c), P 2p (d) and O 1s (e) for the LCGTP0604 glass-ceramic. Spectrum line of C1s (f) for the C-C component resulting from adventitious carbon is also shown as a control. XPS analyses are presented of the LCGTP0604 glass-ceramic before (bottom, cyan blue line) and after LSV in the anodic sweep of 5V vs. Ag_3SI/Ag (middle, purple line) and the cathodic sweep of -1.5V vs. Ag_3SI/Ag (top, red line). Note that intensities on the y-axis have been normalized to emphasize signal shapes rather than absolute intensities. Dashed lines represent BE peaks of LAGTP (black line) [85] and $Li_{1+x}Cr_2(PO_4)_3$ (green line) NASICON-type compounds [90] reported in the literature.

6 CONCLUSIONS

Herein, a new NASICON-structured glass-ceramics based on the $Li_{1+x}Cr_x(Ge_yTi_{1-y})_{2-x}(PO_4)_3$ (LCGTP) system was proposed. Firstly, we investigated a particular composition of this system in terms of the crystallization behavior, formation of NASICON-like phase and electrical properties of the obtained glass-ceramics. The LCGTP glass composition under study showed internal nucleation and the NASICON-like phase was successfully crystallized. The ionic conductivity of glass-ceramics is up to five orders of magnitude higher than that of the precursor glass and is dependent on the heat treatment temperature.

As a second step, the influence of substituting Ti by Cr and Ge on the glass stability of precursor glasses, the cell parameter of NASICON crystal structure and the electrical properties of LCGTP glass-ceramics was investigated. The glass stability of LCGTP glasses can be enhanced with Ge and Cr content. All the glass-ceramics presented the NASICON-like phase and their lattice parameters decreased with Ge and increased with Cr content, enabling adjustment of the unit cell volume of the NASICON-type structure. Furthermore, the total ionic conductivity of the glass-ceramics showed a strong dependence on Cr and Ge content, varying up to 3 orders of magnitude at 300 K (from 3×10^{-4} $\Omega^{-1}cm^{-1}$ for LCGTP0602 to 3×10^{-7} $\Omega^{-1}cm^{-1}$ for LCGTP0208).

Finally, the electrochemical stability window of NASICON-structured glass-ceramics of the $Li_{1+x}Cr_x(Ge_yTi_{1-y})_{2-x}(PO_4)_3$ system was investigated here using a combination of cyclic voltammetry (CV) measurements and *in situ* electrochemical impedance spectroscopy (EIS). The key finding was that the electrochemical stability of this material is limited to low potentials by the reduction of Ti^{+4} cations (around 2.1 V vs. Li^+/Li) and to high potentials (4.6 vs. Li^+/Li) by the oxidation of O^{-2} anions. A similar behavior was encountered for the well-know LAGP NASICON-like Li-ion conducting suggesting that the electrochemical behavior in oxidative potentials could be generalized for NASICON-structured phosphates.

7 SUGGESTIONS FOR FUTURE WORK

There are several practical challenges to incorporate a solid electrolyte into a complex electrochemical system such as a battery. Perhaps, the most critical ones are the manufacturability of an all-solid-state battery and retention of the electrode/electrolyte interface characteristics during cycling when the anode and cathode are changing their volume. Therefore, the development of all-solid-state Li-ion battery using the electrolytes developed here and a well-known cathode and anode materials would be of great interest. The manufacturability of this assemblage should consider different routes of synthesis and consolidation. The further characterization of the interfaces before and after cycling the device is also a crucial point for study.

Regarding the electrolyte specifically, it is suggested a microstructural optimization of the more promising compositions to enhance the total ionic conductivity. Once the grain boundary ionic conductivity is the limiting factor for higher total ionic conductivities, we suggest optimization of the heat treatment conditions to minimize the deleterious effects of grain boundaries. Based on this rationale, the use of a statistic tool, the so-called “response surface methodology analysis”, should lead to a heat treatment condition that optimizes the ionic conductivity using a reduced number of samples and heat treatment conditions.

Another open issue is to unveil the role of chromium-doping in the enhancement of ionic conductivity of this system. Once chromium has a comparable ionic radius of titanium, the increment of the ionic conductivity achieved by substituting titanium by chromium cannot be attributed to cell parameters considerations. Even though, a slight decrease in the activation energy for ion conduction is noticed when chromium replaces mostly titanium. However, X-ray diffraction techniques are not appropriated to detect these structural differences, since chromium and titanium have comparable X-ray scattering factors. On the other hand, neutron scattering length and cross-section are very different for those elements. Besides, lithium is also a very weakly scattering atom for X-rays which makes the determination of lithium sites occupancy an unfeasible task. Again, neutron diffraction could be a practical alternative to overcome this limitation. In this sense, we suggest the use of

neutron diffraction experiments coupled with impedance spectroscopy technique to shed some light on the origin of the enhancement of ionic conductivity caused by chromium doping.

Finally, the electronic conductivity of the electrolytes obtained should be cautiously determined. There are several works in literature with NASICON-like electrolytes of similar compositions which have addressed this issue. However, these studies often neglect fundamental phenomena or use assumptions that prevent a reliable determination of the partial electronic conductivity. As an example, one can cite a modification of the Wagner method which uses symmetric cells with two blocking electrodes instead of one blocking and one reversible electrode. In practice, the real Wagner experiment is very challenging to achieve once it requires one reversible electrode that has an electrochemically stable interface with the electrolyte under teste. Consequently, the choice of the reversible electrode to characterize the electronic conductivity of the electrolyte is a vital issue for the determination of the actual contribution of electronic transport in the total conductivity.

8 REFERENCES

[1] M. Park, X. Zhang, M. Chung, G.B. Less, A.M. Sastry, A review of conduction phenomena in Li-ion batteries, J. Power Sources. 195 (2010) 7904–7929. doi:10.1016/j.jpowsour.2010.06.060.

[2] J.B. Goodenough, P. Singh, Review—Solid Electrolytes in Rechargeable Electrochemical Cells, J. Electrochem. Soc. 162 (2015) A2387–A2392. doi:10.1149/2.0021514jes.

[3] K.B. Oldham, J.C. Myland, A.M. Bond, Electrochemical Science and Technology, John Wiley & Sons, Ltd, Chichester, UK, 2011. doi:10.1002/9781119965992.

[4] V. V. Kharton, Solid State Electrochemistry I, Wiley-VCH Verlag GmbH & Co. KGaA, Weinheim, Germany, 2009. doi:10.1002/9783527627868.

[5] M.R. Palacín, Recent advances in rechargeable battery materials: a chemist's perspective, Chem. Soc. Rev. 38 (2009) 2565. doi:10.1039/b820555h.

[6] R.G. Linford, S. Hackwood, Physical techniques for the study of solid electrolytes, Chem. Rev. 81 (1981) 327–364. doi:10.1021/cr00044a002.

[7] D.K. Gosser, Cyclic voltammetry: Simulation and analysis of reaction mechanisms, VCH, 1993.

[8] A.J. Bard, L.R. Faulkner, Electrochemical Methods: Fundamentals and Applications, Second, John Wiley and Sons, New York, 2001.

[9] J.C. Mauro, Y. Yue, A.J. Ellison, P.K. Gupta, D.C. Allan, Viscosity of glass-forming liquids, Proc. Natl. Acad. Sci. 106 (2009) 19780–19784. doi:10.1073/pnas.0911705106.

[10] J.C. Bachman, S. Muy, A. Grimaud, H.-H. Chang, N. Pour, S.F. Lux, O. Paschos, F. Maglia, S. Lupart, P. Lamp, L. Giordano, Y. Shao-Horn, Inorganic Solid-State Electrolytes for Lithium Batteries: Mechanisms and Properties Governing Ion Conduction, Chem. Rev. 116 (2016) 140–162. doi:10.1021/acs.chemrev.5b00563.

[11] E.A. Smart, Lesley E.; Moore, Solid State Chemistry: An Introduction, Third Edit, CRC Press, New York, 2005.

[12] P.G. Bruce, A.R. West, J.B. Goodenough, J.L. Souquet, D.F. Shriver, F.M. Gray, W.R. McKinnon, W. Weppner, B. Scrosati, R.D. Armstrong, M. Todd, O. Yamamoto, Solid State Electrochemistry, 1997.

[13] D.R. Kingery, W. David; Bowen, Harvey K.; Uhlmann, Introduction to Ceramics, Second, Wiley, New York, 1976.

[14] A.R. West, Solid State Chemistry and its Applications, 2nd Edition, Student Edition, Second, John Wiley & Sons, Ltd, Chichester, UK, 2014.

[15] R.A. Huggins, Simple method to determine electronic and ionic components of the conductivity in mixed conductors a review, Ionics (Kiel). 8 (2002) 300–313. doi:10.1007/BF02376083.

[16] T. Takahashi, O. Yamamoto, The Ag/Ag_3SI/I_2 solid-electrolyte cell, Electrochim. Acta. 11 (1966) 779–789. doi:10.1016/0013-4686(66)87055-X.

[17] E. Robinel, A. Kone, M.J. Duclot, J.L. Souquet, Silver sulfide based glasses, J. Non. Cryst. Solids. 57 (1983) 59–70. doi:10.1016/0022-3093(83)90408-8.

[18] C. Lee, P.K. Dutta, R. Ramamoorthy, S.A. Akbar, Mixed Ionic and Electronic Conduction in Li_3PO_4 Electrolyte for a CO_2 Gas Sensor, J. Electrochem. Soc. 153 (2006) H4. doi:10.1149/1.2129180.

[19] J.B. Wagner, C. Wagner, Electrical Conductivity Measurements on Cuprous Halides, J. Chem. Phys. 26 (1957) 1597–1601. doi:10.1063/1.1743590.

[20] C. Wagner, Investigations on Silver Sulfide, J. Chem. Phys. 21 (1953) 1819–1827. doi:10.1063/1.1698670.

[21] E. Barsoukov, J.R. Macdonald, Impedance Spectroscopy, John Wiley & Sons, Inc., Hoboken, NJ, USA, 2005. doi:10.1002/0471716243.

[22] M.E. Orazem, B. Tribollet, Electrochemical Impedance Spectroscopy, John Wiley & Sons, Inc., Hoboken, NJ, USA, 2008. doi:10.1002/9780470381588.

[23] X.-Z. Yuan, C. Song, H. Wang, J. Zhang, Electrochemical Impedance Spectroscopy in PEM Fuel Cells, Springer London, London, 2010. doi:10.1007/978-1-84882-846-9.

[24] V.F. Lvovich, Impedance Spectroscopy, John Wiley & Sons, Inc., Hoboken, NJ, USA, 2012. doi:10.1002/9781118164075.

[25] J.T.S. Irvine, D.C. Sinclair, A.R. West, Electroceramics: Characterization by Impedance Spectroscopy, Adv. Mater. 2 (1990) 132–138. doi:10.1002/adma.19900020304.

[26] G.A. Mabbott, An introduction to cyclic voltammetry, J. Chem. Educ. 60 (1983) 697. doi:10.1021/ed060p697.

[27] T. Saito,Yuki; Kikuchi, Voltammetry: Theory, types and applications., Nova Publishers, New York, 2014.

[28] N. Nitta, F. Wu, J.T. Lee, G. Yushin, Li-ion battery materials: present and future, Mater. Today. 18 (2015) 252–264. doi:10.1016/j.mattod.2014.10.040.

[29] Y. Zhao, Y. Ding, Y. Li, L. Peng, H.R. Byon, J.B. Goodenough, G. Yu, A chemistry and material perspective on lithium redox flow batteries towards high-density electrical energy storage, Chem. Soc. Rev. 44 (2015) 7968–7996. doi:10.1039/C5CS00289C.

[30] B. Scrosati, J. Garche, Lithium batteries: Status, prospects and future, J. Power Sources. 195 (2010) 2419–2430. doi:10.1016/j.jpowsour.2009.11.048.

[31] M.M. Thackeray, C. Wolverton, E.D. Isaacs, Electrical energy storage for transportation—approaching the limits of, and going beyond, lithium-ion batteries, Energy Environ. Sci. 5 (2012) 7854. doi:10.1039/c2ee21892e.

[32] J.-M. Tarascon, M. Armand, Issues and challenges facing rechargeable lithium batteries, Nature. 414 (2001) 359–367. doi:10.1038/35104644.

[33] G. Jeong, Y.-U. Kim, H. Kim, Y.-J. Kim, H.-J. Sohn, Prospective materials and applications for Li secondary batteries, Energy Environ. Sci. 4 (2011) 1986. doi:10.1039/c0ee00831a.

[34] J.W. Fergus, Ceramic and polymeric solid electrolytes for lithium-ion batteries, J. Power Sources. 195 (2010) 4554–4569. doi:10.1016/j.jpowsour.2010.01.076.

[35] P. Knauth, Inorganic solid Li ion conductors: An overview, Solid State Ionics. 180 (2009) 911–916. doi:10.1016/j.ssi.2009.03.022.

[36] C. Cao, Z.-B. Li, X.-L. Wang, X.-B. Zhao, W.-Q. Han, Recent Advances in Inorganic Solid Electrolytes for Lithium Batteries, Front. Energy Res. 2 (2014) 25. doi:10.3389/fenrg.2014.00025.

[37] K. Takada, Progress and prospective of solid-state lithium batteries, Acta Mater. 61 (2013) 759–770. doi:10.1016/j.actamat.2012.10.034.

[38] M. Tatsumisago, A. Hayashi, Superionic glasses and glass–ceramics in the Li_2S–P_2S_5 system for all-solid-state lithium secondary batteries, Solid State Ionics. 225 (2012) 342–345. doi:10.1016/j.ssi.2012.03.013.

[39] G.-Y. Adachi, N. Imanaka, H. Aono, Fast Li Conducting Ceramic Electrolytes, Adv. Mater. 8 (1996) 127–135. doi:10.1002/adma.19960080205.

[40] Y. Sun, Lithium ion conducting membranes for lithium-air batteries, Nano Energy. 2 (2013) 801–816. doi.org/10.1016/j.nanoen.2013.02.003

[41] V. Thangadurai, W. Weppner, Recent progress in solid oxide and lithium ion conducting electrolytes research, Ionics (Kiel). 12 (2006) 81–92.

doi:10.1007/s11581-006-0013-7.

[42] S. Teng, J. Tan, A. Tiwari, Recent developments in garnet based solid state electrolytes for thin film batteries, Curr. Opin. Solid State Mater. Sci. 18 (2014) 29–38. doi:10.1016/j.cossms.2013.10.002.

[43] N. Anantharamulu, K. Koteswara Rao, G. Rambabu, B. Vijaya Kumar, V. Radha, M. Vithal, A wide-ranging review on Nasicon type materials, J. Mater. Sci. 46 (2011) 2821–2837. doi:10.1007/s10853-011-5302-5.

[44] Z. Dauter, M. Jaskolski, How to read (and understand) Volume A of International Tables for Crystallography : an introduction for nonspecialists, J. Appl. Crystallogr. 43 (2010) 1150–1171. doi:10.1107/S0021889810026956.

[45] J. Kang, H. Chung, C. Doh, B. Kang, B. Han, Integrated study of first principles calculations and experimental measurements for Li-ionic conductivity in Al-doped solid-state $LiGe_2(PO_4)_3$ electrolyte, J. Power Sources. 293 (2015) 11–16. doi:10.1016/j.jpowsour.2015.05.060.

[46] H. Eckert, A.C. Martins Rodrigues, Ion-conducting glass-ceramics for energy-storage applications, MRS Bull. 42 (2017) 206–212. doi:10.1557/mrs.2017.30.

[47] C.R. Mariappan, M. Gellert, C. Yada, F. Rosciano, B. Roling, Grain boundary resistance of fast lithium ion conductors: Comparison between a lithium-ion conductive Li-Al-Ti-P-O-type glass ceramic and a $Li_{1.5}Al_{0.5}Ge_{1.5}P_3O_{12}$ ceramic, Electrochem. Commun. (2012). doi:10.1016/j.elecom.2011.10.022.

[48] C.R. Mariappan, C. Yada, F. Rosciano, B. Roling, Correlation between micro-structural properties and ionic conductivity of $Li_{1.5}Al_{0.5}Ge_{1.5}(PO_4)_3$ ceramics, J. Power Sources. (2011). doi:10.1016/j.jpowsour.2011.03.065.

[49] H. Aono, E. Sugimoto, Y. Sadaoka, N. Imanaka, G. ya Adachi, Ionic conductivity and sinterability of lithium titanium phosphate system, Solid

State Ionics. 40–41 (1990) 38–42.
doi:10.1016/0167-2738(90)90282-V.

[50] H. Aono, E. Sugimoto, Y. Sadaoka, N. Imanaka, G.-Y. Adachi, Ionic Conductivity of Solid Electrolytes Based on Lithium Titanium Phosphate, J. Electrochem. Soc. 1990 volume 137, issue 4, 1023-1027.
doi: 10.1149/1.2086597

[51] M. Cretin, P. Fabry, Comparative study of lithium ion conductors in the system $Li_{1+x}Al_xA_{2-x}IV\ (PO_4)_3$ with AIV=Ti or Ge and 0≤x≤0·7 for use as Li+ sensitive membranes, J. Eur. Ceram. Soc. 19 (1999) 2931–2940.
doi:10.1016/S0955-2219(99)00055-2.

[52] T. Šalkus, M. Barre, a. Kežionis, E. Kazakevičius, O. Bohnke, a. Selskienė, a. F. Orliukas, Ionic conductivity of $Li_{1.3}Al_{0.3-x}Sc_xTi_{1.7}(PO_4)_3$ (x=0, 0.1, 0.15, 0.2, 0.3) solid electrolytes prepared by Pechini process, Solid State Ionics. 225 (2012) 615–619.
doi:10.1016/j.ssi.2012.03.045.

[53] H. Morimoto, H. Awano, J. Terashima, Y. Shindo, S. Nakanishi, N. Ito, K. Ishikawa, S.I. Tobishima, Preparation of lithium ion conducting solid electrolyte of NASICON-type $Li_{1+x}Al_xTi_{2-x}(PO_4)_3$ (x = 0.3) obtained by using the mechanochemical method and its application as surface modification materials of $LiCoO_2$ cathode for lithium cell, J. Power Sources. (2013).
doi:10.1016/j.jpowsour.2013.05.039.

[54] E.D. Zanotto, A Bright Future for Glass-Ceramics, Am. Ceram. Soc. Bull. 89 (2010) 19–27.
http://ceramics.org/wp-content/uploads/2010/09/bulletin_oct-nov2010.pdf.

[55] R.H. Doremus, Glass Science, J. Electrochem. Soc. 122 (1975) 36C.
doi:10.1149/1.2134206.

[56] A.M. Cruz, E.B. Ferreira, A.C.M. Rodrigues, Controlled crystallization and ionic conductivity of a nanostructured $LiAlGePO_4$ glass-ceramic, J. Non. Cryst. Solids. 355 (2009) 2295–2301.
doi:10.1016/j.jnoncrysol.2009.07.012.

[57] J.L. Narváez-Semanate, A.C.M. Rodrigues, Microstructure and ionic conductivity of $Li_{1+x}Al_xTi_{2-x}(PO_4)_3$ NASICON glass-ceramics, Solid State

Ionics. 181 (2010) 1197–1204.
doi:10.1016/j.ssi.2010.05.010.

[58] X. Xu, Z. Wen, X. Wu, X. Yang, Z. Gu, Lithium Ion-Conducting Glass?Ceramics of $Li_{1.5}Al_{0.5}Ge_{1.5}(PO_4)_3$ - xLi_2O (x=0.0-0.20) with Good Electrical and Electrochemical Properties, J. Am. Ceram. Soc. 90 (2007) 2802–2806.
doi:10.1111/j.1551-2916.2007.01827.x.

[59] S. Ujiie, A. Hayashi, M. Tatsumisago, Structure, ionic conductivity and electrochemical stability of Li_2S–P_2S_5–LiI glass and glass–ceramic electrolytes, Solid State Ionics. 211 (2012) 42–45.
doi:10.1016/j.ssi.2012.01.017.

[60] J.-M. Lee, T. Kim, S.-W. Baek, Y. Aihara, Y. Park, Y.-I. Kim, S.-G. Doo, High lithium ion conductivity of $Li_7La_3Zr_2O_{12}$ synthesized by solid state reaction, Solid State Ionics. 258 (2014) 13–17.
doi:10.1016/j.ssi.2014.01.043.

[61] N. Kamaya, K. Homma, Y. Yamakawa, M. Hirayama, R. Kanno, M. Yonemura, T. Kamiyama, Y. Kato, S. Hama, K. Kawamoto, A. Mitsui, A lithium superionic conductor., Nat. Mater. 10 (2011) 682–686.
doi:10.1038/nmat3066.

[62] M. Illbeigi, A. Fazlali, M. Kazazi, A.H. Mohammadi, Effect of simultaneous addition of aluminum and chromium on the lithium ionic conductivity of $LiGe_2(PO_4)_3$ NASICON-type glass–ceramics, Solid State Ionics. 289 (2016) 180–187.
doi:10.1016/j.ssi.2016.03.012.

[63] M. TATSUMISAGO, Glassy materials based on Li_2S for all-solid-state lithium secondary batteries, Solid State Ionics. 175 (2004) 13–18.
doi:10.1016/j.ssi.2004.09.012.

[64] Y. Sun, K. Suzuki, K. Hara, S. Hori, T. Yano, M. Hara, M. Hirayama, R. Kanno, Oxygen substitution effects in $Li_{10}GeP_2S_{12}$ solid electrolyte, J. Power Sources. 324 (2016) 798–803.
doi:10.1016/j.jpowsour.2016.05.100.

[65] I. Tarhouchi, V. Viallet, P. Vinatier, M. Ménétrier, Electrochemical

characterization of $Li_{10}SnP_2S_{12}$: An electrolyte or a negative electrode for solid state Li-ion batteries?, Solid State Ionics. 296 (2016) 18–25. doi:10.1016/j.ssi.2016.08.016.

[66] J.H. Kennedy, F. Chen, Preparation of silver sulfide iodide, J. Inorg. Nucl. Chem. 32 (1970) 695–697. doi:10.1016/0022-1902(70)80282-2.

[67] P.K. Gupta, D.R. Cassar, E.D. Zanotto, On the variation of the maximum crystal nucleation rate temperature with glass transition temperature, J. Non. Cryst. Solids. 442 (2016) 34–39. doi:10.1016/j.jnoncrysol.2016.03.024.

[68] E.D. Zanotto, M.C. Weinberg, Trends in homogeneous crystal nucleation in oxide glasses, Phys. Chem. Glas. 30 (1989) 186–192.

[69] M.L.F. Nascimento, L.A. Souza, E.B. Ferreira, E.D. Zanotto, Can glass stability parameters infer glass forming ability?, J. Non. Cryst. Solids. 351 (2005) 3296–3308. doi:10.1016/j.jnoncrysol.2005.08.013.

[70] A.A. Cabral, C. Fredericci, E.D. Zanotto, A test of the Hrubÿ parameter to estimate glass-forming ability, J. Non. Cryst. Solids. 219 (1997) 182–186. doi:10.1016/S0022-3093(97)00327-X.

[71] A.A. Cabral, A.A.D. Cardoso, E.D. Zanotto, Glass-forming ability versus stability of silicate glasses. I. Experimental test, J. Non. Cryst. Solids. 320 (2003) 1–8. doi:10.1016/S0022-3093(03)00079-6.

[72] S.M. Abo-Naf, M.S. El-Amiry, A.A. Abdel-Khalek, FT-IR and UV–Vis optical absorption spectra of γ-irradiated calcium phosphate glasses doped with Cr_2O_3, V_2O_5 and Fe_2O_3, Opt. Mater. (Amst). 30 (2008) 900–909. doi:10.1016/j.optmat.2007.03.013.

[73] H. Shinozaki, S. Nakashima, S. Takahashi, A. Hanada, Y. Yamamoto, Water resistance of cerium phosphate glasses as studied by in situ high temperature IR microspectroscopy, J. Non. Cryst. Solids. 378 (2013) 55–60. doi:10.1016/j.jnoncrysol.2013.06.016.

[74] C.J. Antony, A. Aatiq, C.Y. Panicker, M.J. Bushiri, H.T. Varghese, T.K. Manojkumar, FT-IR and FT-Raman study of Nasicon type phosphates, $ASnFe(PO_4)_3$ [A=Na_2, Ca, Cd], Spectrochim. Acta Part A Mol. Biomol. Spectrosc. 78 (2011) 415–419. doi:10.1016/j.saa.2010.11.003.

[75] A. Aatiq, M.R. Tigha, Structural and spectroscopic study of $NaSbR(PO_4)_3$ (R = Cr, Fe, In) phases, Powder Diffr. 28 (2013) S394–S408. doi:10.1017/S0885715613000882.

[76] J. Fu, Superionic conductivity of glass-ceramics in the system Li_2O_ Al_2O_3_TiO_2_P_2O_5, Solid State Ionics. 96 (1997) 195–200. doi:10.1016/S0167-2738(97)00018-0.

[77] X. Xu, Z. Wen, Z. Gu, X. Xu, Z. Lin, Lithium ion conductive glass ceramics in the system $Li_{1.4}Al_{0.4}(Ge_{1-x}Ti_x)_{1.6}(PO_4)_3$ (x=0-1.0), Solid State Ionics. 171 (2004) 207–213. doi:10.1016/j.ssi.2004.05.009.

[78] X. Xu, Z. Wen, Z. Gu, X. Xu, Z. Lin, Preparation and characterization of lithium ion-conducting glass-ceramics in the $Li_{1+x}Cr_xGe_{2-x}(PO_4)_3$ system, Electrochem. Commun. 6 (2004) 1233–1237. doi:10.1016/j.elecom.2004.09.024.

[79] H. Chung, B. Kang, Increase in grain boundary ionic conductivity of $Li_{1.5}Al_{0.5}Ge_{1.5}(PO_4)_3$ by adding excess lithium, Solid State Ionics. 263 (2014) 125–130. doi:10.1016/j.ssi.2014.05.016.

[80] X. Xu, Z. Wen, J. Wu, X. Yang, Preparation and electrical properties of NASICON-type structured $Li_{1.4}Al_{0.4}Ti_{1.6}(PO_4)_3$ glass-ceramics by the citric acid-assisted sol-gel method, Solid State Ionics. 178 (2007) 29–34. doi:10.1016/j.ssi.2006.11.009.

[81] J.S. Thokchom, B. Kumar, The effects of crystallization parameters on the ionic conductivity of a lithium aluminum germanium phosphate glass-ceramic, J. Power Sources. 195 (2010) 2870–2876. doi:10.1016/j.jpowsour.2009.11.037.

[82] H.S. Jadhav, M.S. Cho, R.S. Kalubarme, J.S. Lee, K.N. Jung, K.H. Shin,

C.J. Park, Influence of B_2O_3 addition on the ionic conductivity of $Li_{1.5}Al_{0.5}Ge_{1.5}(PO_4)_3$ glass ceramics, J. Power Sources. 241 (2013) 502–508.
doi:10.1016/j.jpowsour.2013.04.137.

[83] B. Yan, Y. Zhu, F. Pan, J. Liu, L. Lu, $Li_{1.5}Al_{0.5}Ge_{1.5}(PO_4)_3$ Li-ion conductor prepared by melt-quench and low temperature pressing, Solid State Ionics. 278 (2015) 65–68.
doi:10.1016/j.ssi.2015.05.020.

[84] R.D. Shannon, Revised effective ionic radii and systematic studies of interatomic distances in halides and chalcogenides, Acta Crystallogr. Sect. A. 32 (1976) 751–767.
doi:10.1107/S0567739476001551.

[85] P. Hartmann, T. Leichtweiss, M.R. Busche, M. Schneider, M. Reich, J. Sann, P. Adelhelm, J. Janek, Degradation of NASICON-Type Materials in Contact with Lithium Metal: Formation of Mixed Conducting Interphases (MCI) on Solid Electrolytes, J. Phys. Chem. C. 117 (2013) 21064–21074.
doi:10.1021/jp4051275.

[86] A. Kone, M. Armand, J.L. Souquet, Triangular voltammetry study of the electrochemical reactions at a glass-noble metal interface—application for the redox stability range measurements, Electrochim. Acta. 27 (1982) 653–656.
doi:10.1016/0013-4686(82)85055-X.

[87] Y. Zhu, X. He, Y. Mo, Origin of Outstanding Stability in the Lithium Solid Electrolyte Materials: Insights from Thermodynamic Analyses Based on First-Principles Calculations, ACS Appl. Mater. Interfaces. 7 (2015) 23685–23693.
doi:10.1021/acsami.5b07517.

[88] P. Bach, M. Stratmann, I. Valencia-Jaime, A.H. Romero, F.U. Renner, Lithiation and Delithiation Mechanisms of Gold Thin Film Model Anodes for Lithium Ion Batteries: Electrochemical Characterization, Electrochim. Acta. 164 (2015) 81–89.
doi:10.1016/j.electacta.2015.02.184.

[89] A. Aatiq, M. Ménétrier, L. Croguennec, E. Suard, C. Delmas, On the structure of $Li_3Ti_2(PO_4)_3$, J. Mater. Chem. 12 (2002) 2971–2978. doi:10.1039/B203652P.

[90] M. Herklotz, F. Scheiba, R. Glaum, E. Mosymow, S. Oswald, J. Eckert, H. Ehrenberg, Electrochemical oxidation of trivalent chromium in a phosphate matrix: $Li_3Cr_2(PO_4)_3$ as cathode material for lithium ion batteries, Electrochim. Acta. 139 (2014) 356–364. doi:10.1016/j.electacta.2014.06.170.

[91] W. Göpel, J.. Anderson, D. Frankel, M. Jaehnig, K. Phillips, J.. Schäfer, G. Rocker, Surface defects of TiO_2(110): A combined XPS, XAES AND ELS study, Surf. Sci. 139 (1984) 333–346. doi:10.1016/0039-6028(84)90054-2.